Synthesis of Ru(II) and Co(II) NNN-pyridine based complexes and their activity in the oxidation of *n*-octane

by

Revana Chanerika

Dissertation submitted in fulfilment of the academic requirements for the degree of

Master of Science in the

School of Chemistry and Physics,

University of KwaZulu-Natal,

Durban,

South Africa

As the candidate's supervisors, we have approved this dissertation for submission.

Signed_____ Name_____Date_____

Signed_____ Name_____Date_____

February, 2017

Abstract

Over the past few decades, the activation of paraffinic C-H bonds has positively impacted synthetic reactions in the natural products chemistry and drug delivery fields. This process of activation has also warranted the use of more economical and easily accessible alkanes from natural gas and petroleum derivatives, which had earlier been ignored for the direct conversion to more value-added products due to their chemical inertness. Pincer complexes have been widely explored in catalytic C-H activation due to their properties such as high thermal stability and their protective nature to a metal centre. Various NNN tridentate ligand systems have shown great affinity towards transition metal complexes, which can exhibit high reactivities as a result of structural modifications introduced by the ligands.

A series of four NNN-pyridine based ligands of the general form: NNN-Rpy (R = propyl, *tert*-butyl, cyclohexyl and phenyl, py = pyridine) were successfully synthesised and characterised through NMR spectroscopy, IR spectroscopy and mass spectrometry. Coordination of the ligands to a Ru benzene dimer and $CoCl_2.6H_2O$ metal precursor afforded novel Ru(II) complexes (**RI-RIV**) and Co(II) NNN-pyridine based complexes (**CV-CVIII**) with varying substituents on the nitrogen backbone, with the aim of investigating the steric and electronic influences of these on the chemistry and reactivity of the catalytic system. These complexes were characterised through techniques including, NMR, IR, MS, elemental analyses and in some cases single crystal XRD. It was found that all complexes existed as mononuclear units (confirmed through the melting point and single-crystal structures for **RI-RIII** and **CV**). All Ru complexes (**RI-RIII**) exhibited a piano stool geometry, while the Co systems portrayed a distorted trigonal bypyramidal geometry (complex **CV**).

These complexes were then tested as catalysts in the oxidation of *n*-octane using *t*-BuOOH and H_2O_2, and the oxygenated products, i.e. octanol, octanone, octanal and octanoic acid were quantified through gas chromatography. A calculation of the conversion and selectivity of each catalyst system under optimum reaction conditions using *t*-BuOOH (temperature = 80 °C, time = 24 hours in an acetonitrile solvent system), revealed **RIV** and **CVI** to be the most efficient systems with TONs of 12.6 and 10.2, respectively. Also, the selectivity was predominantly towards 2-octanol for the Co systems (**CV-CVII**), while 2-octanone was the dominant product formed over all Ru catalysts and **CVIII**. Both metal systems were also highly active using hydrogen peroxide as the oxidant in the activation of *n*-octane with a

conversion of 23% for catalysts **CVII** and **RII**, respectively. Both series of catalysts were highly selective to alcohols within 24 hours.

Preface

The experimental work described in this thesis was performed in the School of Chemistry, University of KwaZulu-Natal, Durban, from January 2015 to December 2016, under the supervision of Prof. H. B. Friedrich and Dr. M. Shozi.

These studies represent original work by the author and have not otherwise been submitted in any form for any degree or diploma to any tertiary institution. The work of others that has been used in this study is duly acknowledged in the text.

Signed _____ Date _____

Revana Chanerika

Declaration 1

Plagiarism

I, ... hereby declare that:

1. The research reported in this thesis, except where otherwise indicated, is my original research.

2. This thesis has not been submitted for any degree or examination at any other university.

3. This thesis does not contain other person's data, pictures, graphs or other information, unless specifically acknowledged as being sourced from other persons.

4. This thesis does not contain other person's writing, unless specifically have been acknowledged as being sourced from other researchers. Where other written sources quoted, then:

    a. Their words have been re-written but the general information attributed to them has been referenced.

    b. Where their exact words have been used, then their writing has been placed in italics and inside quotation marks, and referenced.

5. This thesis does not contain text, graphics or tables copied and pasted from the Internet, unless specifically acknowledged, and the source being detailed in the thesis and in the References sections.

Signed _____ Date _____

Revana Chanerika

Declaration 2

Conference Contributions

Part of the work discussed in this dissertation has been presented as an oral presentation at the following symposiums and conferences:

c*change Symposium 2015, Cape Town, oral presentation, *Synthesis of SNS and NNN Ru, Ni and Fe complexes for the oxidation of paraffins,* Revana Chanerika and H.B. Friedrich.

c*change Symposium 2016, Drakensburg, oral presentation, *Synthesis of Ru(II) and Co (II) NNN complexes and their activity in the oxidation of n-octane*, Revana Chanerika, H.B. Friedrich and M. Shozi.

CATSA Conference 2016, Drakensburg, oral presentation, *Synthesis of Ru and Co NNN-pyridine based complexes and their activity in the oxidation of n-octane*, Revana Chanerika, H.B. Friedrich and M. Shozi.

Table of contents

List of figures

List of schemes

List of tables

Abbreviations

APT	-	Attached Proton Test
ATR	-	Attenuated Total Reflectance
Cy	-	Cyclohexyl
CPD	-	Composite-Pulse Decoupling
DBM	-	Dopamine β-monooxygenase
DCM	-	Dichloromethane
DEPT	-	Distortionless Enhancement by Polarisation Transfer
DMSO	-	Dimethylsulfoxide
ESI	-	Electron Spray Ionisation
Et_2O	-	Diethyl ether
EtOH	-	Ethanol
FID	-	Flame Ionisation Detector
GC	-	Gas chromatography
HSAB	-	Hard Soft Acid Base
HSQC	-	Heteronuclear Single-Quantum Coherence
IR	-	Infrared
MAO	-	Methylaluminoxane
MeCN	-	Acetonitrile
$MgSO_4$	-	Magnesium sulfate
MMO	-	Methane monooxygenase
MMOH	-	Methane monooxygenase hydrolase
MMOR	-	Methane monooxygenase reductase
MP	-	Melting point

MS	-	Mass spectrometry
NAD+	-	β-nicotinamide-adenine dinucleotide
NADH	-	β-nicotinamide-adenine dinucleotide (reduced)
NADPH	-	Nicotinamide-adenine dicucleotide phosphate (reduced)
NMR	-	Nuclear magnetic resonance
Ph/Phe	-	Phenyl
PhIO	-	Iodosylbenzene
pMMO	-	Membrane-bound particle
PPh_3	-	Triphenylphosphine
Prop	-	Propyl
Py	-	Pyridine
QSAR	-	Quantitative structure-activity relationship
RBF	-	Round bottom flask
RT	-	Room temperature
sMMO	-	Soluble methane monooxygenase
TBAB	-	Tetrabutylammonium bromide
TBHP/*t*-BuOOH	-	*tert*-butylhydroperoxide
^{t}Bu/tbut	-	*tert*-butyl
TEMPO	-	2,2,6,6-tetramethylpiperidine-*N*-oxyl
THF	-	Tetrahydrofuran
TLC	-	Thin Layer Chromatography
TON	-	Turn over number
XRD	-	X-Ray Diffraction

Acknowledgments

I would like to express my sincere thanks and appreciation to my supervisors, Prof. H.B. Friedrich and Dr. M. Shozi, for their supervision and guidance through my years of study.

I am also grateful to c*change for financial aid.

My appreciation also goes to the technical staff of the School of Chemistry and Physics: Mr Raj Somaru, Mr Dilip Jagjivan, Mr Gregory Moodley, Mrs Anita Naidoo and Mrs Malini Padayachee for their assistance with instrumentation and chemicals.

In addition, I would like to thank Mrs Jayshree Naicker and Mr Mpho Sehoto for efficient handling and processing of my orders.

My deepest gratitude to my mentor and dear friend, Mrs Lynette Soobramoney, for her assistance and advice with techniques. I would also like to thank all members of CRG for their valuable input during meetings.

My humble appreciation to Mr Michael Pillay and Mr Sizwe Zamisa for single crystal X-ray diffraction data collection and refinement.

A warm thanks to my friends, Ms Letisha Deeplal, Ms Vuyi Mahlaba, Ms Jenelle Moodley, Mr Sachan Naidoo, Mr Drushan Padayachee, Mr Kershen Naicker, Ms Denisha Gounden, Ms Kimona Kisten and Ms Serina Naicker for their untiring support and friendship.

To my dear family, thank you for your unwavering support, advice, and encouragement during my years of study.

Lastly, I would like to thank God, Lord Krishna, for giving me the strength to persevere.

Chapter One

Introduction

1.1 Biomimetics in metal-oxo species

Various biochemical processes utilising oxygen components have propelled the evolution of a variety of organisms that incorporate oxygen in their life-sustaining processes.[1] Functionalisation of the C-H bond usually takes place through dioxygen-utilising enzymes where an oxygen atom is inserted into the C-H bond.[2] To date, an abundance of knowledge and insight has been gained in the study of using enzymes to activate paraffin C-H bonds. Apart from a number of biological components being able to readily carry out this process, this dissertation briefly focuses on the C-H bond activation using copper monooxygenases, dehydrogenases and methane monooxygenase.

1.1.1 C-H oxidation through copper monooxygenases

Yoshizawa and co-workers have studied the active species and function of the amino acids that are seen in the developed dopamine β-monooxygenase (DBM), which consist of two reactive copper sites i.e. CuA and CuB.[3] These reactive sites help promote the stereoselective hydroxylation of dopamine. From the crystal structure determination, in the CuA, Cu is coordinated to three histidine residues, while two histadines and a methionine coordinate in the CuB site. Hydrogen abstraction results when the substrate is orientated through H bonds and three key residues fulfil this role i.e. two glutamates and one tyrosine.

Three active species, Cu-superoxo, Cu-hydroperoxo, and Cu-oxo, bearing different charges and spin states were investigated (Fig. 1.1). The Cu-superoxo specie, which is less reactive than the Cu-oxo specie, was able to promote the H abstraction with an energy barrier of 16.9 kcal mol^{-1}. The Cu-hydroperoxo species, having an energy barrier of 40 kcal mol^{-1}, was ruled out due to the high energy barrier.

In a similar investigation by the same authors, focus was given to the reactivity of the copper centre on the entire enzymatic structure. The energy barrier for the Cu-superoxo species in the H abstraction process was found to be 23.1 kcal mol^{-1} and 5.4 kcal mol^{-1} for the Cu-oxo

species. In the Cu-superoxide pathway, an energy barrier of 18.4 kcal mol^{-1} was established for the hydroxo radical intermediate and -14.2 kcal mol^{-1} for the Cu-oxo pathway. From these findings, it was established that the active species has a Cu=O oxo group incorporated. Thus the protein environment thermodynamically and kinetically favours the hydroxylation reaction.[4]

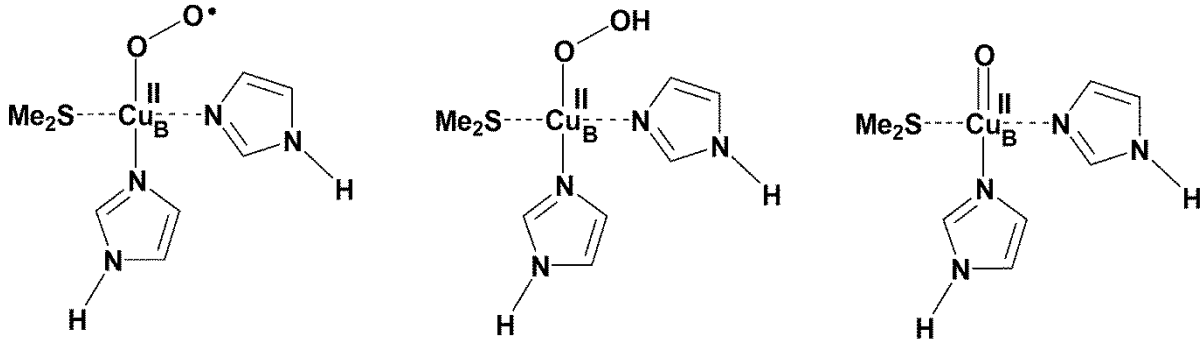

Figure 1.1: The superoxo, hydroperoxo and oxo forms, respectively, of the Cu_B site in DBM.

1.1.2 C-H oxidation through dehydrogenases

Szaleniec *et al*. had focused their study on the oxidation of hydrocarbons *via* the enzyme, ethylbenzene dehydrogenase.[5] This enzyme contains a molybdenum oxo group in its reactive centre and was responsible for catalysing the oxidation of ethylbenzene to form (S)-1-phenylethanol. Considering the cationic or radical nature of the intermediates, three equations were investigated (Scheme 1.1): eq **1** gives a carbocation and a Mo(IV)-OH intermediate through the homolytic C-H cleavage of the substrate. The final reaction product is formed from the attack on the ligand hydrocarbon from the carbocation.

The second equation (eq **2**) is a typical oxygen rebound mechanism, whilst the third (eq **3**) is a combination of equations **2** and **3**. The two processes (**1** and **3**) leading to the formation of the carbocation and the Mo(IV)–OH intermediate are mediated by the homolytic cleavage of the C-H bond and a subsequent electron transfer process. The carbocationic character of the intermediate was described through the development of a quantitative structure-activity relationship (QSAR) model and therefore substantiates the preference for eq **1**. However, in the case of the OH-rebound mechanism playing a role in controlling the rate, the third equation needs to be considered.[5]

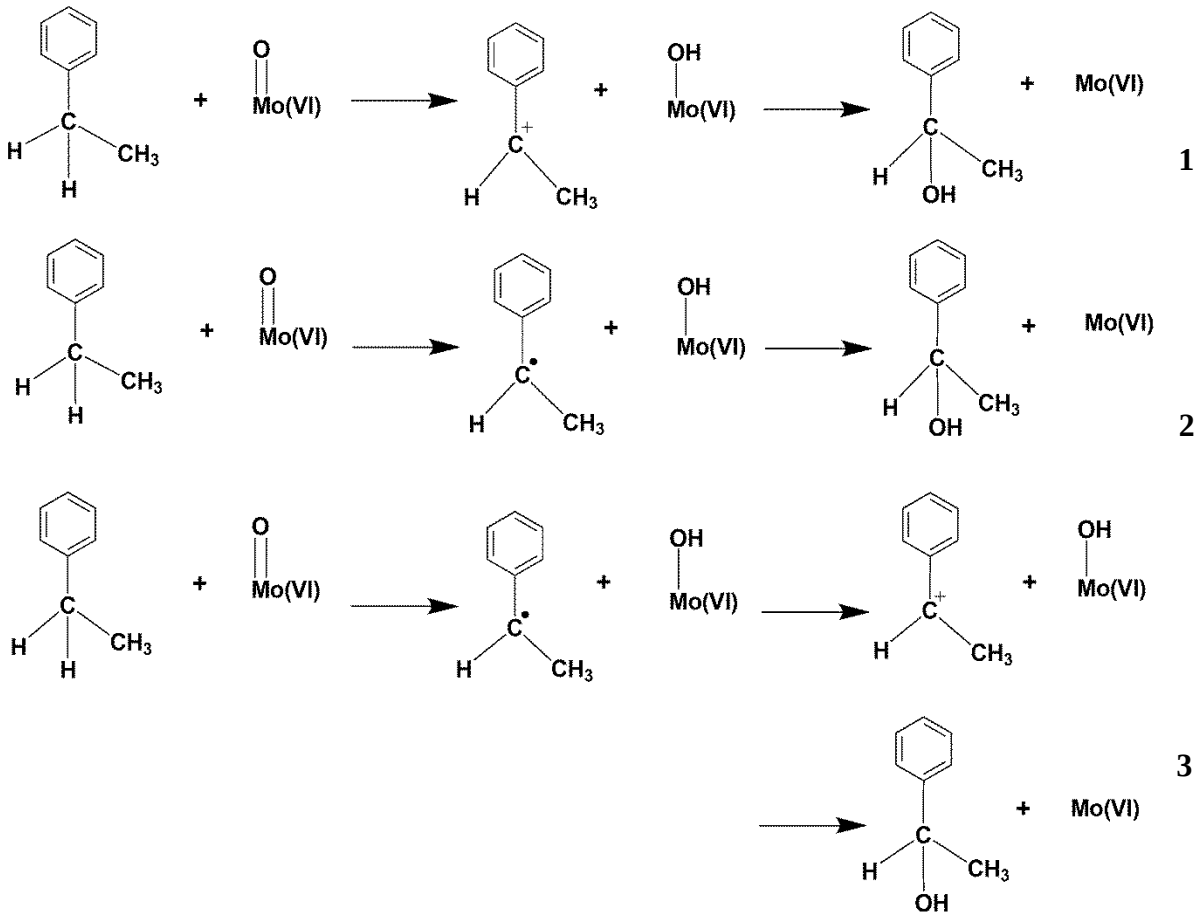

Scheme 1.1: Proposed reaction mechanisms for ethylene dehydrogenase.[5]

1.1.3 C-H oxidation through methane monooxygenase

There has been a rising challenge to develop alternative fuels and have them made available continuously for future purposes. Liquid fuels can use methane gas as their basis or precursor, however, many strategies implemented thus far to catalytically convert methane to methanol have been found neither economical nor sustainable.[6] Methane is used as a sole carbon source by methanotrophic bacteria and these organisms metabolise methane through an initial selective conversion to methanol by methane monooxygenase enzymes (MMO) according to eq **4**[7]:

$$CH_4 + O_2 + NADH + H^+ \xrightarrow{MMO} CH_3OH + H_2O + NAD^+ \qquad \mathbf{4}$$

Methane monooxygenase (MMO) is an enzyme which acts as a catalyst in the conversion of methane to methanol using O_2 as an oxidant under mild reaction conditions i.e. ambient temperatures and pressures.[8] This enzyme is found in methanotrophic bacteria and occurs in two different forms:[9]

i. Soluble (cytoplasmic) methane monooxygenase (sMMO)
ii. Membrane-bound particle (pMMO)

The sMMO comprises of three components i.e. a hydrolase (MMOH), a reductase (MMOR) and an iron source (B) coupled with methane monooxygenase (MMOB).[9] The hydrolase component contains iron in its active site, whilst in contrast, the pMMO components contain copper.[10]

The hydrolase (MMOH) component of the soluble MMO is responsible for catalysing the oxidation of methane by binding the oxygen atom. The resultant oxidised state of MMOH, which is MMOHox, is deemed as the resting state containing a diferric Fe^{3+}-Fe^{2+} core. A metastable intermediate (depicted as intermediate P) complexed to a peroxo ligand results from a two electron reduction process carried out by NAPDH, with subsequent oxidation by O_2. This intermediate leads to an active species (intermediate Q) in methane oxidation, which is a typical FeIV-(μ-O)-FeIV diamond core type. Observable in the arrangement Q, is the bridging of two oxo ligands and one bidentate glutamate to the Fe atom. Also, there is a possible terminal binding of other glutamate and histidine species to the Fe atom, together with the presence of a water molecule in the coordination sphere (Scheme 1.2).

Various mechanisms relating to the hydroxylation of methane catalysed by MMO have been proposed, with an example by Yoshizawa and group[11] (Scheme 1.3). In this mechanism, the starting intermediate consists of methane binding to FeO^{+} through weak Fe-H bonds. The C-H bond activation of this specie involves a hydroxo methyl ion intermediate being formed from a four-centre transition state. In the final methyl migration step, the cleavage and formation of a Fe-C bond and a C-O bond respectively, leads to a Fe^{+1} cation and methanol.

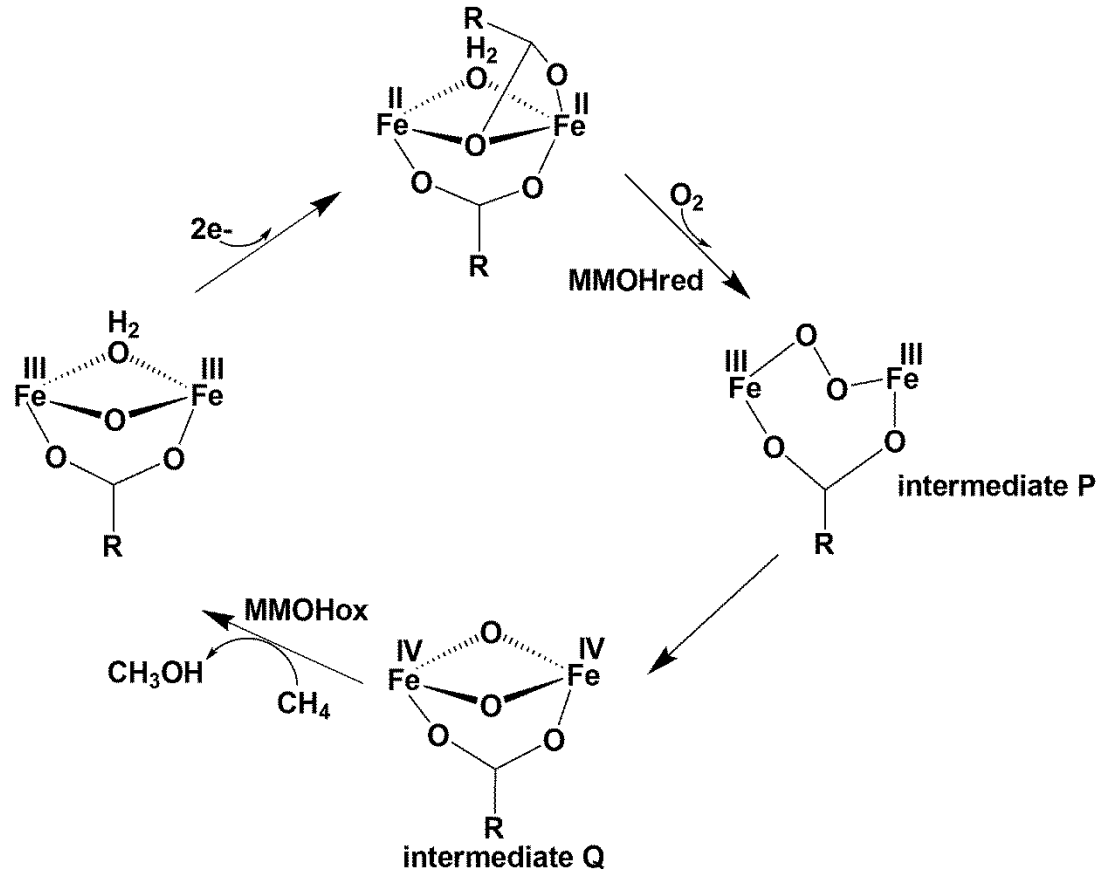

Scheme 1.2: Mechanism for the hydroxylation of methane by MMO.

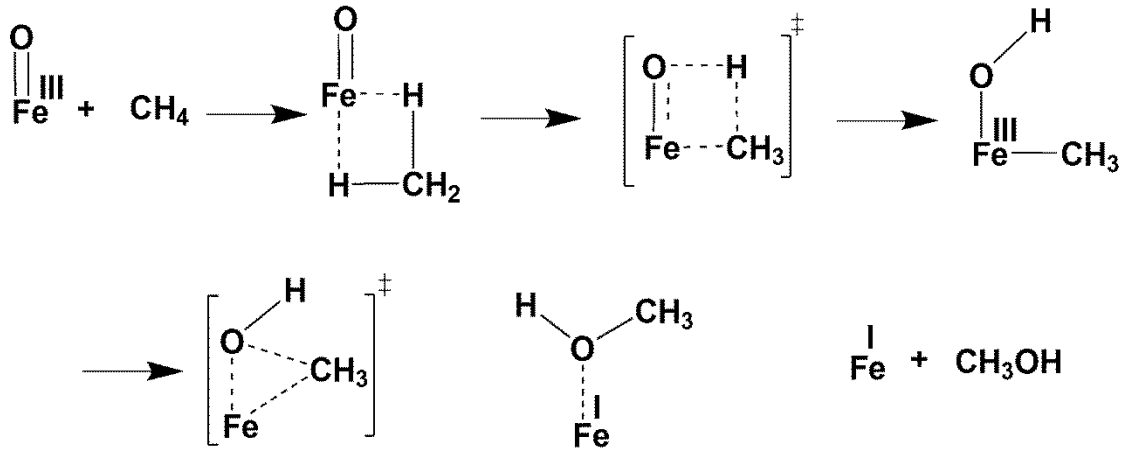

Scheme 1.3: A nonradical mechanism for the oxidation of methane by FeO^+.

1.2 C-H alkane activation

Carbon-hydrogen bond activation, often contrasted with alkane functionalisation, is a reaction involving the cleavage of a C-H bond by a functional group X, usually involving heteroatoms *viz*. carbon, oxygen and nitrogen.[12-14] The concept, according to Goldman and co-workers, is constrained to reactions involving organometallic complexes that are driven through the coordination of a hydrocarbon to the inner-sphere of the metal. This occurs *via* alkane or arene complex intermediates or as a transition state leading to "M-C" intermediates.[15, 16] Over the past decade, the use C-H bond activation in synthetically useful reactions has had profound effect in natural products synthesis and drug delivery.[17]

Prior to the 1980s, research conducted on C-H bonds reacting at transition-metal centres has confirmed that reactions proceed smoothly through the assistance of the C-H bond π orbitals of aromatics (eq **5**).[18, 19]

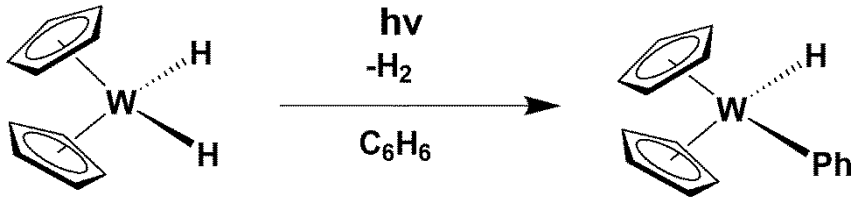

5

Petroleum and natural gas comprise of alkanes or saturated hydrocarbons as the major constituents, however, the use of practical methods to warrant their direct conversion to valuable products, has remained challenging.[18] This difficulty has been recognised in the redistribution of C-C bonds and C-H bonds in hydrocarbons to give more sophisticated architectures.[20]

A further difficulty presents itself in the relative inertness of alkanes, which arises from the constituent atoms that are held by strong C-C and C-H bonds. Thus, a chemical reaction is hindered as the molecules do not have low energy empty orbitals or high energy filled orbitals to participate in this reaction. This effect is negated in unsaturated hydrocarbons, such as alkenes and alkynes, and the C-H bonds are efficiently and selectively activated, thus presenting a positive economic impact. The associated advantages of hydrocarbons, involving their low cost and ubiquity, has been evident in the more atom economical C-H bond functionalisation.[21]

In general, four mechanisms of C-H bond functionalisation have been postulated depending on the metal (M) and ligand (Ln) set in the active species (LnM). This dissertation mentions briefly the outline and functionality of each mechanism listed below:

i. Oxidative addition
ii. Sigma bond metathesis
iii. Electrophilic substitution
iv. 1,2-addition

Oxidative addition, seen as the most common mechanism, involves the cleavage of a C-H bond and the formation of a M-C and M-H bond. This mechanism is typical of late transition metals (Re, Fe, Ru, Os, Ir and Pt). The σ-bond metathesis mechanism is preferred for early transition metals (groups 3 and 4), since an oxidative process is not possible for these metals. The key aspect in this mechanism is the formation of the M-C and C'-H bonds with cleavage of the M-C' and C-H bonds at the transition state. The electrophilic substitution mechanism had been classified according to the substitution process of the hydrogen by the Lewis acidic metal species. Finally, the C-H bond can add across a M-X bond through a 1,2 addition (Scheme 1.4).

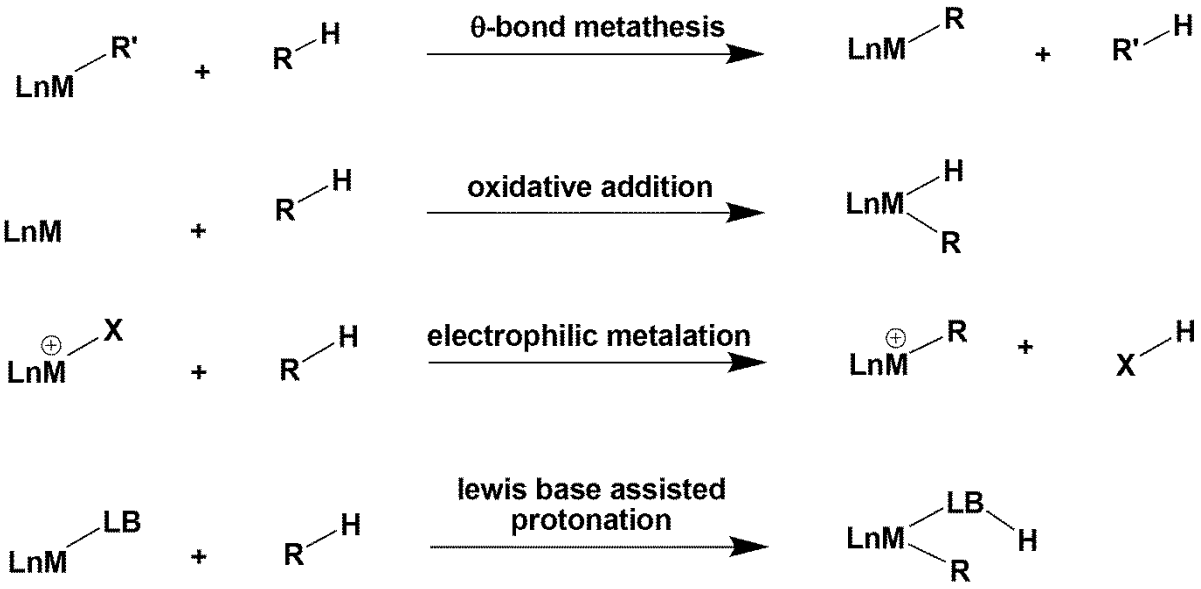

Scheme 1.4: A representation of common C-H bond activation mechanisms (LB = Lewis-base).[21]

1.2.1 Stoichiometric C-H bond activation

Some synthetic methodologies have shown that well-defined organometallic complexes supported on oxides containing ligands (hydrides, alkyls, alkylidynes and alkylidenes), will facilitate a C-H bond activation process spontaneously under controlled reaction conditions.[20] In this dissertation, a brief review is given on the C-H activation of alkanes on supported substrates with an in depth focus directed to the activation of alkanes driven by intramolecular processes.

1.2.1.1 C-H activation of alkanes on supported metals

Alkanes which undergo C-H bond activation on silica supported metal hydrides will readily give rise to metal-alkyl fragments. This can be illustrated by silica supported hydrides and zirconium which freely reacts with various alkanes e.g. cyclohexane and propane, at low temperature to yield H_2 and the corresponding metal alkyl complexes (Scheme 1.5).[22, 23]

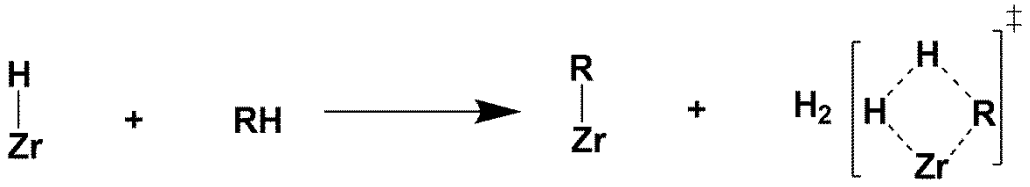

Scheme 1.5: C-H bond activation of cyclohexane or propane on zirconium hydrides supported on silica.[22]

The C-H bond activation of propane is fast and yields a stable *n*-propyl surface species together with a minor isopropyl surface species as the isomer.[24] This reaction occurs through proton transfer from the alkane to the Zr-H species (σ-bond metathesis). The resultant transition state is seen as having a quasi-triangular shape with the carbon and two H atoms mimicking a linear relationship (Scheme 1.5).[25]

Spectroscopic investigations conducted have shown that the Zr hydrides supported on silica substrates have produced mixtures of mono- and bis-hydrides (Scheme 1.6).[26] Also, a study conducted on the relative reactivity of the zirconium-hydride supported complexes toward methane confirmed that the bis-hydride is more reactive.[27]

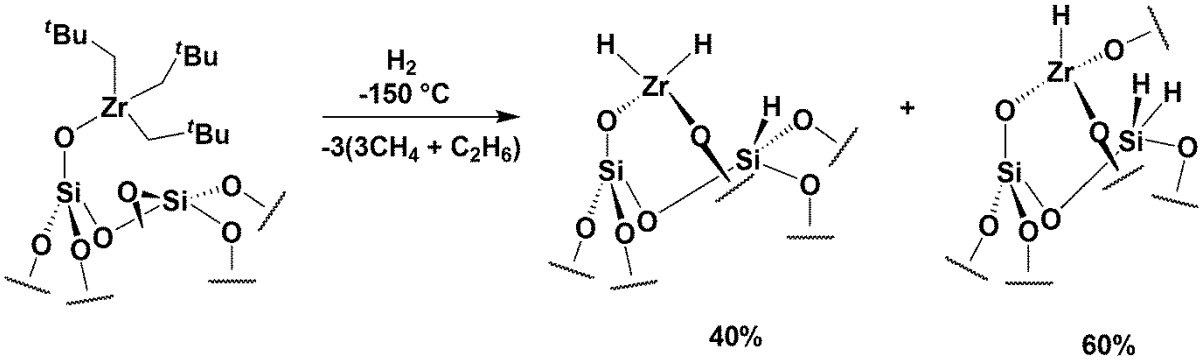

Scheme 1.6: Synthesis and structure of zirconium hydrides supported on silica.[26]

Through an elementary step of α-H abstraction, it has been established that well-defined metal alkylidene complexes on silica supports form through a thermal decomposition of bis-alkyl surface species.[26] Here, the elementary step involves an alkyl-ligand situated at the α-position having its C-H bond intramolecularly activated by an adjacent ligand (an alkyl in this case). This corresponds to a σ-bond metathesis process, but an intramolecular version of it.[28] The grafting process of Ta and Re molecular alkylidene complexes onto silica supports[29, 30], involves a reaction that produces a bis-alkyl species *via* a 1,2-addition of the metal (Ta or Re) onto the surface silanols. To yield the alkylidene species, the resultant bis-alkyl complex must undergo decomposition (Scheme 1.7).

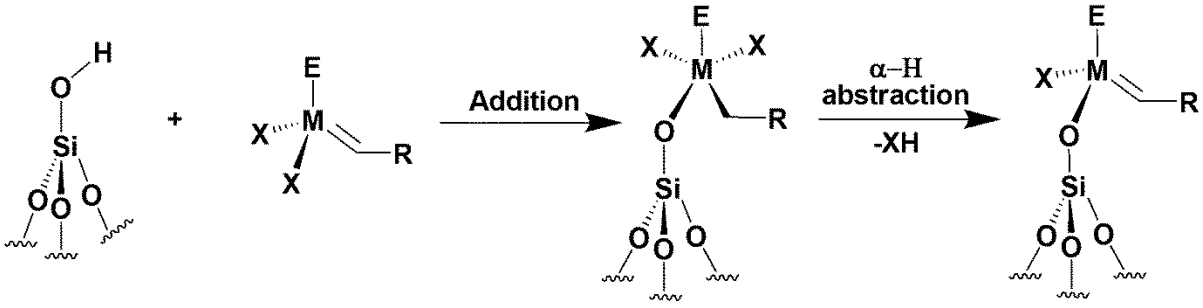

M = Ta, E = X = $CH_2{}^tBu$
M = Mo/W, E = NR, X = CH_2R_3, NR_2, OR
M = Re, E = ER, X = $CH_2{}^tBu$

Scheme 1.7: Addition of an OH group to the alkylidene moiety followed by abstraction of α-H.[29, 30]

1.2.2 Pincer complexes for paraffinic activation

The fields of catalytic chemistry and materials have attracted considerable attention relating to pincer ligands and their coordination to metals. This was due to the special properties displayed by the metal as a result of the coordinated ligand.[31] The first type of pincer ligand was synthesised in 1976 by Moulton and Shaw.[32] This ligand together with its complex represented a derivative of a novel diphosphine. A careful study of the properties of these complexes in the 1980's revealed exceptional thermal stability due to their high melting points. This is one property that promotes the use of these ligands and complexes in homogeneous catalysis today.[32]

A typical pincer ligand involves an *ortho-ortho* disubstituted aryl ring with heteroatom substituents that include CH_2NR_2, CH_2PR_2 or CH_2SR_2 groups. These substituents generally have the ability to coordinate to the metal centre, thus supporting the M-C σ-bond.[33] This coordination is a terdentate one comprising of two metallacyles sharing the same M-C bond. A general formula may be used to describe a pincer ligand, $[2,6\text{-}(ECH_2)_2C_6H_3]^-$ (ECE), where E corresponds to a two-electron donor atom, i.e. $N(R^2)_2$, $P(R^2)_2$, $As(R^2)_2$, OR^2 or SR^2, whilst C is associated to the carbon atom of the 2,6-disubstituted phenyl ring. The aryl ring may also bear an R^1 substituent which is generally in the 4 position (Fig 1.2).[33]

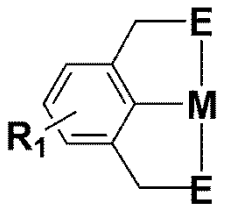

Figure 1.2: General structure of a pincer complex with donor atoms (E) and metal centre (M) bound to a phenyl ring.[33]

Many desirable properties arise from the coordination of a multidentate ligand to a specific metal, with one such property being the reduction of leaching (dissociation of the ligand from the metal). The lability of the complex may be fine-tuned by the donor atoms and substituents present on the complex thereby influencing the metal electron density as well as the coordination of substrates to the metal.[34] This controls the electronic and steric properties of the metal as a whole. In recent years, modification of the substituents on PCP pincer complexes has induced chirality in various processes.[34]

1.2.3 Transition metal C-H activation assisted by chelation

Over the past several years, synthetic transformations driven by transition metal catalysts have emerged as one of the most reliable and powerful tools in bond forming reactions and have allowed for economic and efficient preparation of complex molecular structures. Coupling reactions, such as the Suzuki-Miyaura, Heck, Stille, and Kumada, have been widely employed when vinyl-, aryl-, and alkyl (pseudo) halides (preactivated electrophiles) react with organometallic nucleophiles.[35] In recent years, researchers have gained impressive achievements in utilising late transition metals (Ru, Rh, Pd, Fe, Ir) in catalysing the sp^2 bond transformation of various heteroaromatics. This dissertation focuses on comparing earth abundant and cheap transition metals to the uses of late transition metals in catalysing the C-H bond activation of *n*-octane.

The first step in forming metal-carbon bonds, prior to an actual bond cleavage, is for the coordination of the hydrocarbon bond to a vacant site on the metal. In most cases, the C-H activation of aromatics is favoured over that of aliphatics, taking into account the thermodynamics of the resultant M-C bond.[20] In the C-H bond activation of aliphatics, the primary carbons are generally favoured over the secondary and tertiary carbons. However, for the various C-H bonds on a substituted aromatic molecule, little selectivity is usually seen and is accounted for by the steric effects observed in the molecule.[20] *Ortho* C-H bond activation is exemplified in the fluorinated aromatics where the activation of the C-H bonds of *ortho* F atoms is generally thermodynamically favoured.[20] This example is an exception to the lower selectivities generally observed for aromatics.

The effect of *ortho* substituted fluorine atoms on selectivity has been rationalised from the inductive effect introduced from the *ortho* F atom which causes an increase in the M-C bond's ionic component. Milstein and his group have extended their research to other sigma-attracting haloatoms, i.e. Cl, Br and OMe. The selective activation of *ortho* substituted C-H bonds has been widely studied using Ir(I) complexes (Scheme 1.8).[36] As seen in Scheme 1.9, the major kinetic product formed is as a result of the *ortho* C-H activation in conjunction with a mixture of other ortho, para and meta activated sites. Heating at a temperature of 50 °C makes possible the recovery of the sole thermodynamic product, that being the *ortho* C-H activated species. In some cases, para activation also occurs in fluorobenzene.

Short Ir-X bond distances are observed in the product of the C-H activated *ortho* substituted chlorobenzene and anisole. The bond distances for Ir-Cl and Ir-OMe are 2.816 Å and 2.76 Å, respectively. The resultant selectivity observed is due to the coordination of the heteroatom to the Ir metal. A thermodynamically stable complex is obtained as a result of the coordination of the Ir metal to the C-H bond of the *ortho* substituted species. The rate determining step ultimately produces the fourteen electron intermediate, $(PNP)Ir^{+}$, following the dissociation of cyclooctene and this intermediate mediates the C-H bond activation.

In general, the selective activation is established *via* the η^1-coordination of the heteroatom, in this case the O atom in anisole, followed by subsequent isomerisation to an *ortho* η^2-C-H complex. Upon C-H cleavage, additional thermodynamic stabilisation is introduced from the X coordination to a vacant site.

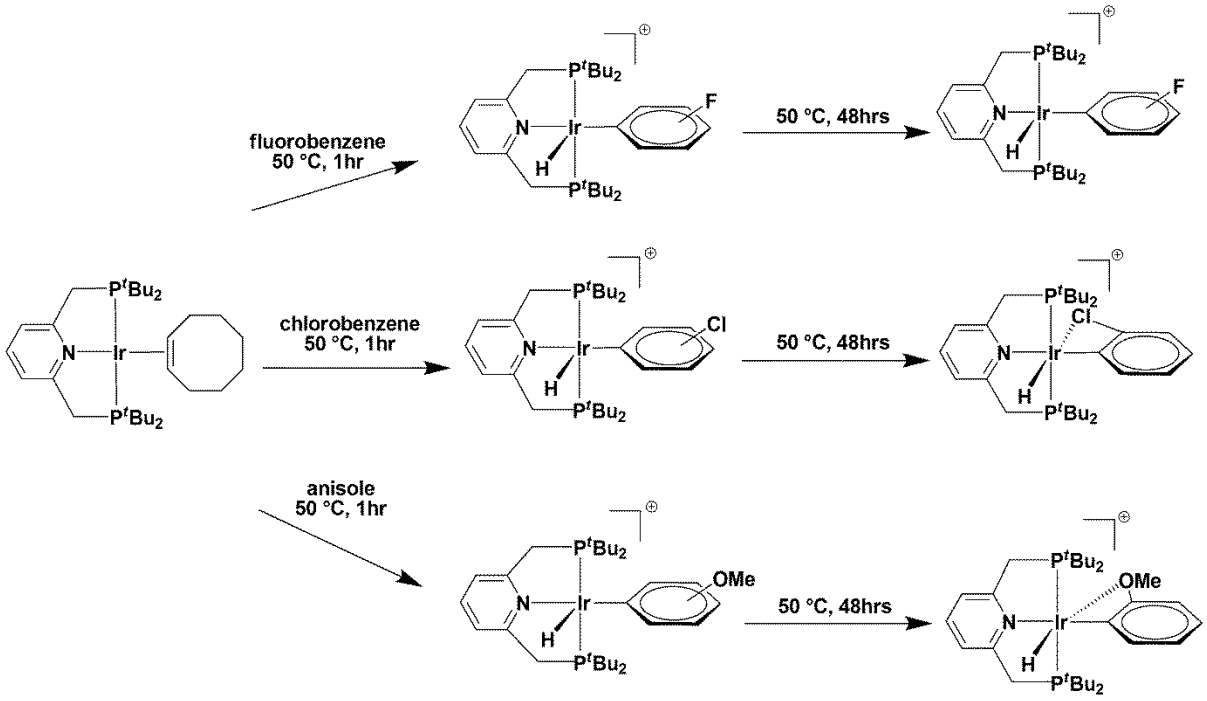

Scheme 1.8: Haloarenes undergoing *ortho* C-H activation by an Ir(I) complex.[36]

1.2.4 Ru catalysed C-H activation

Recent developments in ruthenium pincer complexes that are coordinatively saturated or unsaturated with heteroaromatic and aliphatic backbones, have become key points of interest. These complexes exhibit new reactivities in terms of activating strong chemical bonds and serve as efficient catalysts for several synthetic methods, including green transformations.[37]

There are numerous reports on Ru pincer complexes, and a summary of the key developments regarding bond activation and catalysis is presented.

A report by Gunnoe and co-workers has highlighted the generation of a cyclometalated PCP Ru pincer complex through sp^3 C-H activation (Scheme 1.9).[38] This was achieved through liberation of ammonia from a five coordinate complex, [(PCP)Ru(CO)(NH_2)] (**1**), and methane from [(PCP)Ru(CO)(CH_3)] (**2**). The rate of conversion of the methyl complex **2** to **3** appeared to occur 5 times faster than the conversion with the amido complex (**1**). Attempts at intermolecular C-H activation of methane using complex **1** were unsuccessful and provided **3** *via* intramolecular C-H activation.

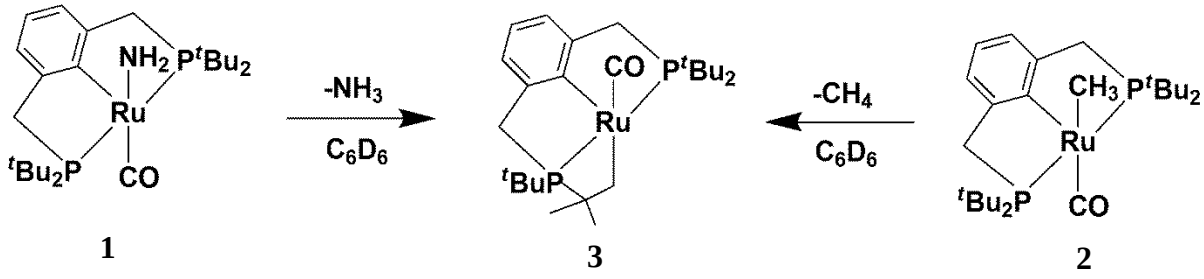

1 **3** **2**

Scheme 1.9: Intramolecular activation of sp^3 C-H Bonds.[38]

Murai and co-workers have studied aromatic ketones, where olefin insertion into a C-H bond that is ortho substituted to a carbonyl group, has been a fundamental breakthrough and has led to an important discovery in the field of C-H bond functionalisation (Scheme 1.10).[39, 40] The reaction proceeds *via* refluxing a catalyst precursor, i.e. toluene, with $RuH_2(CO)(PPh_3)_3$ with the active species being either Ru(0), $RuH_2(CO)(PPh_3)_3$, or $RuH_2(CO)(PPh_3)_2$ complexes. The rate determining step in this reaction has been established to be a C-C coupling process.

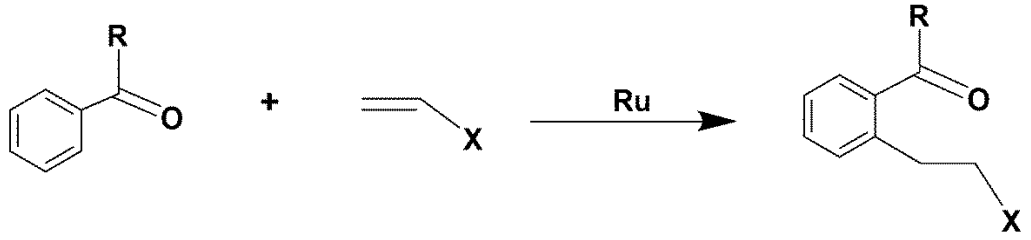

Scheme 1.10: Olefin insertion into an *ortho* C-H bond of an aromatic ketone catalysed by $RuH_2(CO)(PPh_3)_2$.[39, 40]

1.2.5 Co catalysed C-H activation

Numerous coordination chemistry reports show that Co(II) can exhibit tetrahedral, square planar, trigonal bipyramidal and octahedral stereochemical configurations.[41] To date, there has been limited research carried out in the C-H bond activation of alkane substrates catalysed by cobalt pincer complexes. The use of first row transition metals exhibiting two-electron reactivity over the one electron alternatives, which are often common but disruptive, has led to the development of catalysts which are earth-abundant and inexpensive.[42, 43]

Recently, Soobramoney *et al*. reported on pyridine and amine based tridentate SNS ligands with formulae, 2,6-bis($RSCH_2$)pyridine and bis($RSCH_2CH_2$)amine [R = alkyl, aryl], complexed to $CoCl_2.6H_2O$. These complexes were tested in the C-H activation of *n*-octane using *tert*-butylhydroperxide (TBHP) as the oxidant at a substrate to oxidant ratio of 1:20. Findings of this study revealed Co[2,6-bis(CH_3SCH_2)pyridine]Cl_2 to be the most active catalyst among other catalysts of the pyridine-based series with a conversion of 12%, whilst Co[bis($CH_3CH_2SCH_2CH_2$)amine]Cl_2 was most active among the amine-based systems with a total conversion of 23%. This was attributed to the sterics of the complexes in which the more rigid pyridine-based SNS systems gave a higher selectivity toward alcohols with an overall dominant selectivity to ketones for each catalyst.[44]

1.3 NNN terdentate complexes

Heterocyclic ligands containing nitrogen donors have drawn attention in various fields, including homogeneous catalysis, coordination chemistry and organic synthesis. These organometallic complexes exhibit high reactivities as a result of the nitrogen donor in the ligand system. Research conducted in recent years revealed applications of planar tridentate NNN ligands in materials, physical chemistry, homogenous catalysis and organic synthesis.[45] In contrast, reports on unsymmetrical planar tridentate NNN ligands bound to various transition metals have only been sporadic.[46]

Recent reports have revealed unsymmetrical 2,6-(mixed *N*-heterocyclic) ligands in the absence of bound phosphine groups illustrating an “on-off” chelating effect occurring on the metal centre during catalysis. As a result, these transition metal complexes display enhanced selectivity and catalytic activity.[47]

1.3.1 Pyridine based NNN pincer systems

Over the years, insight has been gained into coordination compounds of palladium(II) combined with various NNN tridentate ligands. These include bis(2-pyridylmethyl)amine (bpma), diethylentriamine (dien) or 2,2':6',2"-terpyridine (terpy), and have been useful in ligand substitution reactions of square-planar complexes.[48] The reactivity of these complexes is known to be influenced by small structural modifications in the multidentate ligands.[49] Nowadays, much attention has been directed to the lability of square-planar Pd(II) complexes by tuning their steric and electronic properties.

Mijatovic and group have focused on the synthesis, structure and reactivity of Pd(II) coordination complexes with novel chelating ligands. Two nitrogen based tridentate donor ligands were synthesised, TL^{tBu} = 2,6-bis[(1,3-di-*tert*-butylimidazolin-2-imino)methyl]pyridine and tpdm = terpyridinedimethane, complexed to palladium(II), yielding $[(TL^{tBu})PdCl]^+$ and $[(tpdm)PdCl]^+$. Substitution reactions of complexes **4** and **5** (Fig. 1.3) were carried out with nucleophiles including thiourea, pyridine, dimethylsulfoxide (DMSO), I^-, Br^- and NO_2^- in a 0.1 M sodium perchlorate solution with 10 mM sodium chloride. The reaction temperatures used were 288 K, 298 K, and 308 K. Complex **4**, $[(tpdm)PdCl]^+$, was seen to react faster than complex **5** containing the TL^{tBu} ligand, due to the bulky nature of the tridentate ligand slowing down the rate of the reaction. The reactivity of both ligands was highest in thiourea and lowest in DMSO.[50]

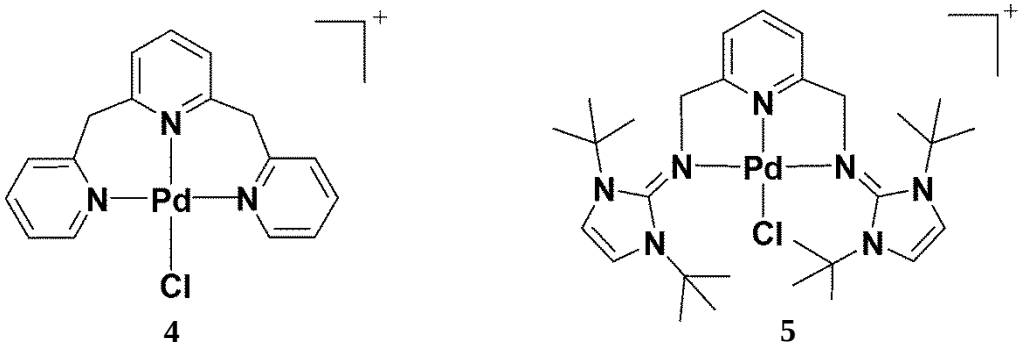

Figure 1.3: Synthesis of complexes $[(tpdm)PdCl]^+$ (**4**) and $[(TL^{tBu})PdCl]^+$ (**5**).[50]

The discovery of remarkable catalytic activities displayed by Pd(II) and Ni(II) complexes containing α-diimine ligands in the polymerisation of ethylene, has inspired interest in the coordination chemistry of these complexes among many researchers.[51] Thus, for example, Zhang *et al.* focussed on monochloropalladium complexes prepared by treating 2-(*N*-

alkylcarboxamide)-6-iminopyridyl $PdCl_2(CH_3CN)_2$ in dichloromethane (Scheme 1.11). To yield the dichloronickel complex, 2-(*N*-alkylcarboxamide)-6-iminopyridyl was treated with $NiCl_2.6H_2O$ in ethanol (Scheme 1.11). The molecular structures of Pd(II) and Ni(II) show that these complexes exhibit distorted square planar and square-pyramidal geometries, respectively. In the presence of methylaluminoxane (MAO), the catalytic activity of the palladium complexes were optimum in the polymerisation of norbornene, whilst the nickel complexes showed enhanced activity in ethylene dimerisation.[52]

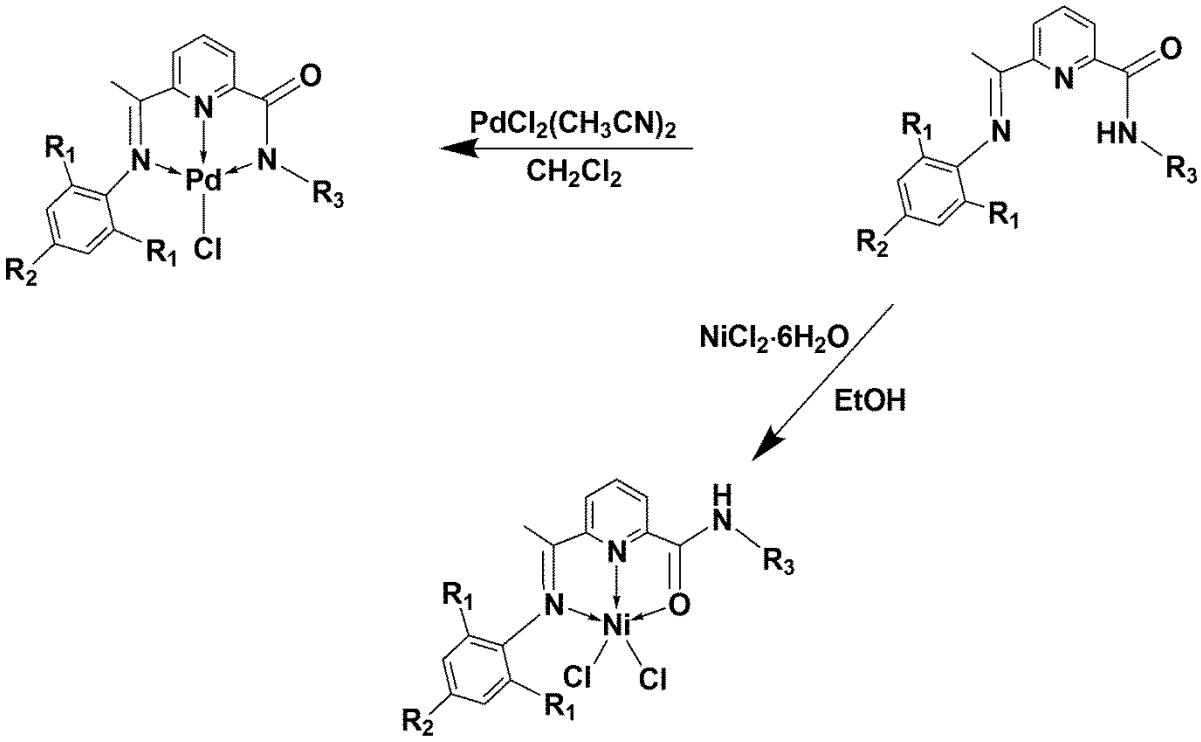

Scheme 1.11: The synthesis of palladium and nickel complexes containing α-diimine ligands in the polymerisation of ethylene.[52]

1.3.2 Specific applications of NNN pincer complexes

As mentioned previously, nitrogen-bearing donor ligands have captured the attention of many researchers due to the excellent catalytic activity exhibited by these ligands. A number of studies have been reported on their synthesis and structure, together with their applications, which include the hydrosilylation of olefins, oligomerisation and polymerisation of ethylene, symmetric and asymmetric transfer hydrogenation of ketones, as well as applications in Heck reactions. This chapter now focuses on the oligomerisation and polymerisation of ethylene,

the transfer hydrogenation of ketones and the hydrosilylation of olefins, outlining the role of various transition metal NNN complexes in these applications.

1.3.2.1 Ethylene oligomerisation and polymerisation

The discovery of iron and cobalt 2,6-bis(imino)pyridine complexes has spawned the use of late transition metal catalysts in ethylene oligomerisation and polymerisation. These 2,6-bis(imino)pyridine iron and cobalt complexes showed remarkable activity in the oligomerisation and polymerisation of ethylene in the works of Brookhart[53] and Gibson.[54] Due to the advantages exhibited by iron and cobalt complexes, such as high catalytic activity and low toxicity, research has been directed to ligand modifications and the development of alternative catalysts.

Sun and Xiao have worked on developing novel iron and cobalt catalysts containing NNN tridentate ligands for ethylene oligomerisation and polymerisation. Both symmetrical and unsymmetrical iron catalysts bearing 2,6-bis(imino)pyridines were synthesised and employed, e.g. complex **6** (Fig. 1.4). Both the iron and cobalt complexes containing 2-(ethylcarboxylato)-6-iminopyrdines, complexes **7** (Fig. 1.4), were efficient in catalysing the oligomerisation and polymerisation of ethylene with particular selectivity for α-olefins in the presence of the cocatalyst, methylaluminoxane (MAO). Other iron and cobalt complexes, e.g. complexes **8** (Fig. 1.4), ligated by 2,9-bis(imino)-1,10-phenanthroline, were also synthesised by this group, and the enhanced catalysing ability of cobalt complexes for both ethylene oligomerisation and polymerisation was shown. In contrast, iron complexes only showed negligible activities for the polymerisation of ethylene. This was attributed to the added nitrogen group on the second imino group of the iron catalyst occupying the site necessary for the coordination of ethylene.[55]

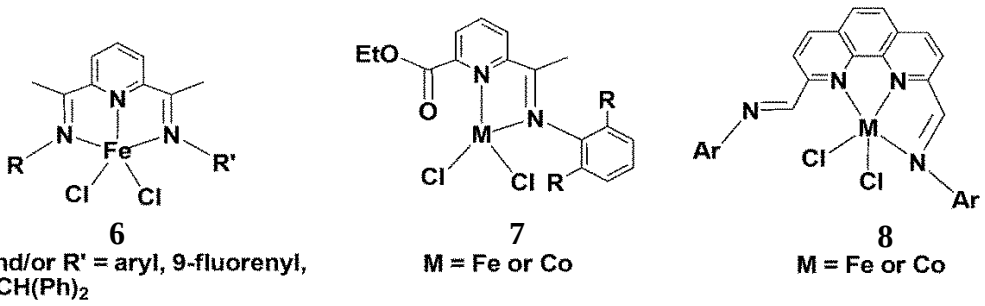

Figure 1.4: Procatalysts based on iminopyridine ligands (**6** and **7**) and iminophenanthrolines (**8**).[55]

1.3.2.2 Transfer hydrogenation

The reduction of ketones to alcohols using 2-propanol as the hydrogen source (rather than hydrogen) has proven to be a promising route in transfer hydrogenation.[56] There have been many reports on efficient Ru(II) catalysts that effectively reduce ketones to alcohols in the transfer hydrogenation process using 2-propanol as a hydrogen source. Thus, e.g. Ru(II) compounds, synthesised by Noyori and group, containing aminoalcohols or monotosylated 1,2-diamines in their system, have shown superior catalytic activity and selectivity due to the N-H group.[57] Another study conducted by Baratta *et al.*, who had developed Ru(II) 2-(aminomethyl)pyridine (ampy) phosphane catalysts, showed increased activity in the transfer hydrogenation of ketones as a result of the N-H group based on the ampy ligand.[58] The impact of the N-H moiety on the catalytic activity and selectivity was termed as the N-H effect. The absence of an N-H functionality on Ru(II) complexes has also been reported for the transfer hydrogenation of ketones. These rare examples include a study conducted by Zhao *et al.* who successfully synthesised Ru(II) NNN complexes combined with an unsymmetrical pyrazolyl-imino ligand. These complexes displayed good to excellent catalytic activity in refluxing 2-propanol in the transfer hydrogenation of ketones.[56]

1.3.2.3 Hydrosilylation of olefins

Olefin hydrosilylation catalysed by transition metals has played a key role in the synthesis of commercial silicones with applications in moulding products and agrochemical adhesives, among others.[59] These commercial silicones are produced by an anti-Markovnikov addition of the tertiary silane to a terminal alkane following the discovery of catalysts exhibiting terminal selectivity.

Over the past three decades, platinum compounds have been used to produce anti-Markovnikov products as they are highly active and stable. However, due to the high cost and volatility of platinum metals, there has been a quest for the use of more affordable metal catalysts to carry out the process. Taking these factors into consideration, Tondreau and group focussed their study on iron dialkyl complexes, $Fe(CH_2SiMe_3)_2$, using three different tridentate nitrogen-donor ligands: terpyridine, aryl-substituted bis(imino)pyridines and pyridine bis(oxazoline). These complexes have been evaluated in the hydrosilylation of olefins with tertiary silanes and the results showed that aryl-substituted bis(imino)pyridine iron complexes are efficient in catalysing the hydrosilylation of 1-octene with

$(Me_3SiO)_2MeSiH$ and $(EtO)_3SiH$ over a period of 1 hour at 60 ºC. In contrast, the pyridine bis(oxazoline) iron complex showed no activity in the hydrosilylation of 1-octene. The terpyridine iron dialkyl complex was established to be an effective catalyst in the hydrosilylation of 1-octene showing a 95% conversion at 60 ºC with tertiary silanes.[59]

1.4 Research approach and scope

Over the past few years, much insight has been gained in the field of C-H activation occurring at metal centres. In the beginning, there was much speculation on whether alkane activation occurring at metal centres was at all possible. From investigations conducted by various research groups, a conclusion was reached that this is possible and might be easier than expected. From this realisation, some research has focused on how the process occurs. Various mechanisms have been investigated, particularly for oxidative alkane activation, although there is ongoing research on controlling the selectivity and activity of the catalytic C-H activation. This allows for the exploration of alkane chemistry in developing practical processes and using them more efficiently and cleanly.

Since C-H activation has now entered the mainstream, this study is aimed at investigating the catalytic activity of ruthenium and cobalt systems in the C-H activation of *n*-octane. This study will also strive to achieve optimum selectivity and substrate conversion and investigate whether this will be possible under mild reaction conditions (reaction temperatures, solvent and oxidant) in an attempt to focus on an overall green process.

Another objective of this project is to analyse the effect of the hard nitrogen donating atoms on rigid NNN systems toward the activity of each catalyst. Also, some emphasis will be placed on investigating the stability, steric and electronic effects of the complexes when varying the ligand substituents ranging from propyl, *tert*-butyl, cyclohexyl and phenyl groups on the central N-donor atom as depicted in Fig. 1.5 below.

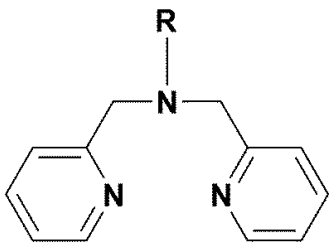

Figure 1.5: General structure of the NNN ligand (R: propyl, *tert*-butyl, cyclohexyl and phenyl).

Since these ligand systems are considered biomimetic in nature, they are deemed fit to function under mild reaction conditions as opposed to those catalyst systems requiring harsh reaction conditions. From the reports gathered on transition metal catalysts, ruthenium and cobalt metals are perceived as suitable choices as they are efficient in the paraffinic C-H activation due to their functional group tolerance.

1.5 References

1. J. Raymond and D. Segre, *Science*, 2006, **311**, 1764-1767.
2. S. Shaik, S. Cohen, Y. Wang, H. Chen, D. Kumar and W. Thiel, *Chemical Reviews*, 2010, **110**, 949-1017.
3. T. Kamachi, N. Kihara, Y. Shiota and K. Yoshizawa, *Inorganic Chemistry*, 2005, **44**, 4226-4236.
4. K. Yoshizawa, N. Kihara, T. Kamachi and Y. Shiota, *Inorganic Chemistry*, 2006, **45**, 3034-3041.
5. M. Szaleniec, M. Witko and J. Heider, *Journal of Molecular Catalysis A: Chemical*, 2008, **286**, 128-136.
6. H. Arakawa, M. Aresta, J. N. Armor, M. A. Barteau, E. J. Beckman, A. T. Bell, J. E. Bercaw, C. Creutz, E. Dinjus, D. A. Dixon, K. Domen, D. L. DuBois, J. Eckert, E. Fujita, D. H. Gibson, W. A. Goddard, D. W. Goodman, J. Keller, G. J. Kubas, H. H. Kung, J. E. Lyons, L. E. Manzer, T. J. Marks, K. Morokuma, K. M. Nicholas, R. Periana, L. Que, J. Rostrup-Nielson, W. M. Sachtler, L. D. Schmidt, A. Sen, G. A. Somorjai, P. C. Stair, B. R. Stults and W. Tumas, *Chemical Reviews*, 2001, **101**, 953-996.
7. C. E. Tinberg and S. J. Lippard, *Accounts of Chemical Research*, 2011, **44**, 280-288.
8. C. Bedard and R. Knowles, *Microbiological Reviews*, 1989, **53**, 68-84.
9. J. D. Lipscomb, *Annual Review of Microbiology*, 1994, **48**, 371-399.
10. H. H. T. Nguyen, K. H. Nakagawa, B. Hedman, S. J. Elliott, M. E. Lidstrom, K. O. Hodgson and S. I. Chan, *Journal of the American Chemical Society*, 1996, **118**, 12766-12776.
11. Y. Shiota and K. Yoshizawa, *Journal of the American Chemical Society*, 2000, **122**, 12317-12326.
12. R. H. Crabtree, *Journal of the Chemical Society, Dalton Transactions*, 2001, 2437-2450.
13. R. H. Crabtree, *Journal of Organometallic Chemistry*, 2004, **689**, 4083-4091.
14. B. G. Hashiguchi, S. M. Bischof, M. M. Konnick and R. A. Periana, *Accounts of Chemical Research*, 2012, **45**, 885-898.
15. I. G. Karen and S. G. Alan, *Activation and Functionalisation of C-H Bonds*, American Chemical Society, 2004.

16. B. A. Arndtsen, R. G. Bergman, T. A. Mobley and T. H. Peterson, *Accounts of Chemical Research*, 1995, **28**, 154-162.
17. I. V. Seregin and V. Gevorgyan, *Chemical Society Reviews*, 2007, **36**, 1173-1193.
18. J. A. Labinger and J. E. Bercaw, *Nature*, 2002, **417**, 507-514.
19. M. L. Green and P. J. Knowles, *Journal of the Chemical Society D: Chemical Communications*, 1970, 1677-1677.
20. D. Balcells, E. Clot and O. Eisenstein, *Chemical Reviews*, 2010, **110**, 749-823.
21. D. A. Colby, R. G. Bergman and J. A. Ellman, *Chemical Reviews*, 2010, **110**, 624.
22. G. H. Loew and D. L. Harris, *Chemical Reviews*, 2000, **100**, 407-420.
23. J. H. Dawson and M. Sono, *Chemical Reviews*, 1987, **87**, 1255-1276.
24. S. Shaik, D. Kumar, S. P. de Visser, A. Altun and W. Thiel, *Chemical Reviews*, 2005, **105**, 2279-2328.
25. C. U. Carlsen, J. K. S. Møller and L. H. Skibsted, *Coordination Chemistry Reviews*, 2005, **249**, 485-498.
26. C. Corpéret, *Chemical Reviews*, 2010, **110**, 656-680.
27. W. Koch and M. C. Holthausen, in *A Chemist's Guide to Density Functional Theory*, Wiley-VCH Verlag GmbH, 2001, 93-116.
28. L. E. Schock and T. J. Marks, *Journal of the American Chemical Society*, 1988, **110**, 7701-7715.
29. A. Toner, J. Matthes, S. Grundemann, H. H. Limbach, B. Chaudret, E. Clot and S. Sabo-Etienne, *Proceedings of the National Academy of Sciences of the United States of America*, 2007, **104**, 6945-6950.
30. M. A. Esteruelas, A. Lledós, M. Oliván, E. Oñate, M. A. Tajada and G. Ujaque, *Organometallics*, 2003, **22**, 3753-3765.
31. T. Suzuki, Y. Kajita and H. Masuda, *Dalton transactions*, 2014, **43**, 9732-9739.
32. C. J. Moulton, B. L. Shaw, *Journal of the Chemical Society, Dalton Transactions*, 1976, 1020–1024.
33. M. Albrecht and G. van Koten, *Angewandte Chemie*, 2001, **40**, 3750-3781.
34. J. T. Singleton, *Tetrahedron*, 2003, **59**, 1837-1857.
35. L. Ackermann and R. Vicente, in *Modern Arylation Methods*, Wiley-VCH Verlag GmbH & Co. KGaA, 2009, 311-333.
36. E. Ben-Ari, R. Cohen, M. Gandelman, L. J. W. Shimon, J. M. L. Martin and D. Milstein, *Organometallics*, 2006, **25**, 3190-3210.
37. C. Gunanathan and D. Milstein, *Chemical Reviews*, 2014, **114**, 12024-12087.

38. D. Conner, K. N. Jayaprakash, T. R. Cundari and T. B. Gunnoe, *Organometallics*, 2004, **23**, 2724-2733.
39. F. Kakiuchi and S. Murai, *Accounts of Chemical Research*, 2002, **35**, 826-834.
40. F. Kakiuchi and N. Chatani, *Advanced Synthesis & Catalysis*, 2003, **345**, 1077-1101.
41. Herausgeg. von R. S. Young, *Journal of the American Chemical Society*, 1963, **75**, 256.
42. L. D. Field, A. V. George and B. A. Messerle, *Journal of the Chemical Society, Chemical Communications*, 1991, 1339-1341.
43. E. J. Klinker, S. Shaik, H. Hirao and L. Que, *Angewandte Chemie*, 2009, **48**, 1291-1295.
44. L. Soobramoney, M. D. Bala and H. B. Friedrich, *Dalton Transactions*, 2014, **43**, 15968-15978.
45. W. Baratta, G. Chelucci, E. Herdtweck, S. Magnolia, K. Siega and P. Rigo, *Angewandte Chemie International Edition*, 2007, **46**, 7651-7654.
46. J. F. Sonnenberg, N. Coombs, P. A. Dube and R. H. Morris, *Journal of the American Chemical Society*, 2012, **134**, 5893-5899.
47. W. Du, L. Wang, P. Wu and Z. Yu, *Chemistry – A European Journal*, 2012, **18**, 11550-11554.
48. Ž. D. Bugarčić, B. Petrović and E. Zangrando, *Inorganica Chimica Acta*, 2004, **357**, 2650-2656.
49. D. Jaganyi, A. Hofmann and R. van Eldik, *Angewandte Chemie International Edition*, 2001, **40**, 1680-1683.
50. A. Mijatović, J. Bogojeski, B. Petrović and Ž. D. Bugarčić, *Inorganica Chimica Acta*, 2012, **383**, 300-304.
51. L. K. Johnson, C. M. Killian and M. Brookhart, *Journal of the American Chemical Society*, 1995, **117**, 6414-6415.
52. W. Zhang, Y. Wang, J. Yu, C. Redshaw, X. Hao and W. H. Sun, *Dalton Transactions*, 2011, **40**, 12856-12865.
53. B. L. Small, M. Brookhart and A. M. A. Bennett, *Journal of the American Chemical Society*, 1998, **120**, 4049-4050.
54. V. C. Gibson, B. S. Kimberley, A. J. P. White, D. J. Williams and P. Howard, *Chemical Communications*, 1998, 313-314.

55. S. Jie, W.-h. Sun and T. Xiao, *Chinese Journal of Polymer Science*, 2010, **28**, 299-304.

56. W. Ye, M. Zhao, W. Du, Q. Jiang, K. Wu, P. Wu and Z. Yu, *Chemistry – A European Journal*, 2011, 17, 4737-4741.

57. T. Ohkuma, N. Utsumi, K. Tsutsumi, K. Murata, C. Sandoval and R. Noyori, *Journal of the American Chemical Society*, 2006, **128**, 8724-8725.

58. W. Baratta, M. Ballico, G. Esposito and P. Rigo, *Chemistry – A European Journal*, 2008, **14**, 5588-5595.

59. A. M. Tondreau, C. C. H. Atienza, J. M. Darmon, C. Milsmann, H. M. Hoyt, K. J. Weller, S. A. Nye, K. M. Lewis, J. Boyer, J. G. P. Delis, E. Lobkovsky and P. J. Chirik, *Organometallics*, 2012, **31**, 4886-4893.

Chapter Two

Preparative methods for NNN-pyridine based ligands and complexes

2.1 Introduction

This chapter describes the synthetic approach taken to prepare terdentate NNN ligands and their metal complexes. It also reports on the characterisation techniques (^{1}H NMR, ^{13}C NMR, IR, MS, MP and elemental analysis) used for the structural elucidation, as well as confirmation on the purity of the synthesised complexes.

NNN tridentate ligands, more commonly known as pincer ligands, comprise of a set with hard donor ability. Pincer ligand systems form three tridentate coordinative bonds in a complex linking each donor atom to the metal centre and thus enclosing the metal like a pincer. Diverse structural variations are also seen in the coordination modes of these ligands which range from bidentate to tridentate and also tetradentate methods of binding.

According to the Hard Soft Acid Base (HSAB) theory, a hard acid usually coordinates more readily to a hard base, whereas a soft acid prefers a soft base. Adopting this theory to NNN donor systems comprising of three hard nitrogen donor atoms, ligand coordination takes place more freely using second row divalent transition metals which are essentially hard acids. The construction of versatile ligand moieties has been desired in order to develop transition metal catalysts that are highly active. The different behaviour of catalysts in various applications stems from the finely tuned ligand, whereby substituents on each donor of the NNN systems, as well as the type of linker binding the N atoms, all contribute to the complex reactivity and stability.[1, 2]

Various substituted NNN ligands have been studied and reported in literature. These substituents include combinations of alkyl groups[3-5], branched alkyl chains[6-8], cyclic groups[9-10] and aromatics[11-12]. Of these substituents, this project focuses on the contrasting effects of aromatic (phenyl) versus aliphatic (propyl, *tert*-butyl and cyclohexyl) substituents on the central nitrogen backbone of the NNN system and their influence on the planarity and geometry of the consequential complexes. Also, investigations are carried out on the effects

of these interchangeable nitrogen substituents in conjunction to the catalyst activity, which may either be steric or electronically influenced.

2.1.1 NNN pincer ligands

Each NNN pincer ligand is composed of a R group, *viz.* propyl (prop), *tert*-butyl (tbut) cyclohexyl (cy) and phenyl (phe) on the nitrogen backbone. In this project, the nitrogen backbone will be bound to two constrained six membered pyridine rings *via* two methylene linkers in the NNN system (Fig 2.1). Hereafter, these ligands will be referred to using an abbreviated naming system, i.e. NNN-propy, NNN-tbutpy, NNN-cypy and NNN-phepy reflecting the amine substituent (propyl, *tert*-butyl, cyclohexyl or phenyl) on the nitrogen backbone linked to two pyridine (py) rings.

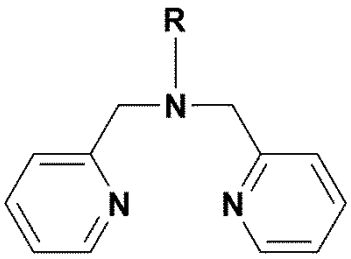

Figure 2.1: General structure of the NNN ligand (R: propyl, *tert*-butyl, cyclohexyl and phenyl).

2.2 Experimental

2.2.1 Materials

Unless otherwise noted, all ligands and complexes were synthesised under inert atmosphere of argon or nitrogen using standard Schlenk techniques. All glassware was oven dried and thus rendered moisture free. All solvents were dried prior to use using standard procedures. Absolute ethanol (EtOH) was dried over magnesium filings and iodine, dichloromethane (DCM) was dried over phosphorus pentoxide, diethyl ether (Et_2O) and tetrahydrofuran (THF) were dried over sodium wire, whilst acetonitrile and methanol were dried over 4 Å molecular sieves. All column chromatography solvents were distilled prior to use. Pure nitrogen and argon gasses were purchased from Afrox and Air Products. The starting materials used in the ligand preparation, which include 2-pyridine methanol (98%), propylamine (98%), *tert*-butylamine (98%), cyclohexylamine (99%), aniline (99%) and tetrabutylammonium bromide (TBAB), were purchased from Sigma-Aldrich and used without further purification. Ruthenium(III) chloride hydrate was sourced from DLD Scientific. Cobalt chloride hexahydrate was obtained from Associated Chemical Enterprises and used as received.

2.2.2 Instrumentation

All ligand and diamagnetic ruthenium structures were elucidated using NMR spectroscopy, which was performed at ambient temperature using a Bruker Avance III 400 MHz spectrophotometer. Each ^{1}H NMR peak shift (δ, ppm) is referenced to the solvent peak dimethylsulfoxide-d6 (m, 2.50 ppm) with the multiplicity and number of protons indicated in parentheses. The chemical shifts (δ, ppm) of the peaks in the proton decoupled ^{13}C NMR data are referenced to the DMSO-d6 solvent peak (39.51 ppm) with the specific carbon indicated in parentheses. The ^{13}C DEPT 135 data showing individual positive (pos) and negative (neg) chemical shifts that correspond to methine (CH), methylene (CH_2) and methyl (CH_3) peaks, as well as selected ^{13}C APT NMR data for confirmation of quarternary carbons, are also reported for the ligands and complexes. Likewise, the corresponding carbons in these spectra are indicated in parenthesis.

As another structural confirmation technique, infrared (IR) spectroscopy was used in identifying functional group band shifts corresponding to the electromagnetic radiation

absorbed at specific frequencies which the bonds vibrate at. All IR spectra were recorded on a Perkin Elmer with an Attenuated Total Reflectance (ATR) attachment.

Elemental analysis was used as a technique in proving the purity of all complexes. This was performed on a ThermoScientific Flash 2000 elemental analyser. The second technique used in assessing the purity of the ligands and complexes, was determining their melting point ranges using a Stuart Scientific melting point apparatus. The mass-to-charge ratio (m/z) of all ligands and complexes were determined using high and low resolution mass spectrometry. This technique was another structural confirmation technique which presented the molecular ion peak in a hundred percent abundance in most cases, hence proving the formation of the complexes. This spectrometric data was obtained on a Bruker Micro TOF-Q11 using electron spray ionisation (ESI) as a soft ionisation technique, with a pre-prepped sample of a concentration of 10 ppm.

2.2.3 Experimental methods

2.2.3.1 Synthesis of NNN ligands

Precursor 2-chloromethylpyridine hydrochloride

The preparation of 2-chloromethylpyridine hydrochloride was adapted from a reported protocol by Moelands *et* al[13]. To a 250 mL round bottom flask, 2.1 mL (0.029 mol) of 2-pyridine methanol was added in 50 mL of DCM. This solution was placed in an ice bath with a cooled solution (~ 4 °C) of thionyl chloride (1.9 mL, 0.020 mol) added dropwise from a dropper connected to a N_2 inlet. The white turbid mixture was stirred for 1 hour at 0 °C during which the solution turned clear. The ice bath was then removed and the solution was allowed to stir for an hour at room temperature. The solution was then quenched with 3.5 mL of *n*-propanol and stirred for a further 15 minutes. The solvent was removed *in vacuo* in which the product precipitated as an off-white solid which was dried under vacuum overnight (4.07 g, 93%). ^{1}H NMR (400 MHz, DMSO): δ 5.0 (s, 2H, CH_2-Cl), 7.8 (m, 1H, CH-py), 8.0 (d, 1H, *J*= 7.7 Hz, CH-py), 8.4 (m, 1H, CH-py), 8.8 (d, 1H, *J*= 4.7 Hz, CH-py). ^{13}C NMR (400 MHz, DMSO): δ 42.3 (CH_2-Cl), 125.7 (CH-py), 126.0 (CH-py), 143.6 (CH-py), 144.5 (CH-py), 152.7 (C-py).

NNN-propy

The preparation of NNN-propy was adapted from a reported procedure by Carney *et al*. with a few modifications.[14] To a 100 mL round bottom flask containing a solution of potassium carbonate (6 g) in 50 mL of acetonitrile, 2 g (12.45 mmol) of 2-chloromethyl pyridine hydrochloride was added. To this solution, 0.34 mL (4.15 mmol) of propylamine was added dropwise and an immediate colour change from white to orange was observed. A mass of 0.05 g tetrabutylammonium bromide (TBAB) was added to the mixture which was then refluxed for 3 days. The brown slurry was filtered through a Buchner funnel and the solvent removed under reduced pressure yielding a thick red-brown oil. The oil was treated with 30 mL of 1 M sodium hydroxide solution and extracted thrice with 30 mL of DCM. The solvent was evaporated under vacuum and a thick dark brown oil was obtained. No further purification was required as shown by a single spot on the TLC (silica) plate (1.41 g, 47% based on 2-chloromethyl pyridine HCl). ^{1}H NMR (400 MHz, DMSO): δ 0.8 (t, 3H, *J*= 7.8 Hz, CH_3-prop), 1.4 (m, 2H, CH_2-prop), 2.4 (t, 2H, *J*= 7.5 Hz, prop-CH_2-N), 3.7 (s, 4H, N-CH_2-py), 7.2 (m, 2H, CH-py), 7.5 (d, 2H, *J*= 7.9 Hz, CH-py), 7.7 (ddd, 2H, *J*= 8.8, 7.7, 0.7 Hz, CH-py), 8.5 (d, 2H, *J*= 4.5 Hz, CH-py). ^{13}C NMR (400 MHz, DMSO): δ 11.6 (CH_3-prop), 19.8 (CH_2-prop), 55.6 (prop-CH_2-N), 59.8 (N-CH_2-py), 121.9 (CH-py), 122.4 (CH-py), 136.4 (CH-py), 148.6 (CH-py), 159.6 (C-py). ^{13}C DEPT 135 (400 MHz, DMSO): δ 11.6 (CH_3-CH_2) pos, 19.8 (CH_3-CH_2-CH_2) neg, 55.6 (CH_3-CH_2-N) neg, 59.8 (N-CH_2-py) neg, 121.9 (CH-py) pos, 122.4 (CH-py) pos, 136.4 (CH-py) pos, 148.6 (CH-py) pos. IR ν_{max} (cm^{-1}): 2959 (m), 2934 (m), 2873 (m), 1589 (s), 1569 (s), 1432 (s), 1047 (s), 753 (s).

NNN-tbutpy

The synthesis of the NNN-tbutpy ligand was adapted from a reported protocol by Wright *et al*. with a few modifications.[6] To a N_2 saturated 100 mL round bottom flask containing 40 mL water, 8.2 g (0.05 mol) of 2-chloromethylpyridine HCl was added, together with a dropwise addition of 2.68 mL (0.025 mol) *tert*-butylamine. The mixture was heated to 50 ºC in an oil bath and a solution of 4 g of sodium hydroxide in 10 mL water was quickly added. The mixture was left to stir at 50 ºC, after which the mixture was extracted four times with chloroform. The combined organic layers were washed several times with water before being dried with $MgSO_4$. The solvent was removed under reduced pressure and the crude product obtained was passed through a silica packed column with chloroform ($CHCl_3$), yielding a

crystalline yellow solid (1.0 g, 16% based on *tert*-butylamine). ^{1}H NMR (400 MHz, DMSO): δ 1.1 (s, 9H, CH_3-tbut), 3.8 (s, 4H, N-CH_2-py), 7.1 (ddd, 2H, *J*= 7.6, 6.0, 0.8 Hz, CH-py), 7.4 (d, 2H, *J*= 7.8 Hz, CH-py), 7.6 (ddd, 2H, *J*= 8.3, 7.8, 1.5 Hz, CH-py), 8.3 (d, 2H, *J*= 4.5 Hz, CH-py). ^{13}C NMR (400 MHz, DMSO): δ 26.9 (CH_3-tbut), 55.3 (C-tbut), 55.8 (N-CH_2-py), 121.4 (CH-py), 122.6 (CH-py), 135.8 (CH-py), 148.1 (CH-py), 161.9 (C-py). ^{13}C DEPT 135 (400 MHz, DMSO): δ 26.9 (CH_3-tbut) pos, 55.8 (N-CH_2-py) neg, 121.4 (CH-py) pos, 122.6 (CH-py) pos, 135.8 (CH-py) pos, 148.1 (CH-py) pos. IR ν_{max} (cm^{-1}): 2963 (w), 2877 (w), 1589 (w), 1433 (w), 1197 (s), 1137 (w), 768 (s), 403 (s).

NNN-cypy

The NNN-cypy ligand was prepared by mimicking an established method by Song *et al*[15]. To a 100 mL round bottom flask, 15 mL of double distilled water was added, followed by an addition of 2-chloromethylpyridine HCl (4.96 g, 0.03 mol). Cyclohexylamine (1.73 mL, 0.015 mol) was added dropwise to the mixture which was stirred for 5 minutes before adding 2.4 g (0.06 mol) of NaOH pellets. The mixture was further stirred for 5 days at room temperature and the product was then extracted with 3 x 30 mL portions of $CHCl_3$. The organic layers were combined and dried over $MgSO_4$, yielding a crude product that was passed through a silica packed column and eluted with $CHCl_3$. The off-white crystalline solid obtained was isolated in moderate yield (1.8 g, 43% based on cyclohexylamine). ^{1}H NMR (400 MHz, DMSO): δ 1.1 (m, 2H, CH_2-cy), 1.3 (q, 2H, *J*= 11.1 Hz, CH_2-cy), 1.5 (m, 2H, CH_2-cy), 1.7 (m, 2H, CH_2-cy), 1.8 (d, 2H, *J*= 12.6 Hz, CH_2-cy), 2.4 (m, 1H, CH_2-cy), 3.8 (s, 4H, N-CH_2-py), 7.2 (ddd, 2H, *J*= 7.6, 3.9, 1.1 Hz, CH-py), 7.5 (d, 2H, *J*= 7.6 Hz, CH-py), 7.7 (ddd, 2H, *J*= 8.6, 7.8, 1.7 Hz, CH-py), 8.4 (d, 2H, *J*= 4.9 Hz, CH-py). ^{13}C NMR (400 MHz, DMSO): δ 24.4 (CH_2-cy), 25.6 (CH_2-cy), 25.7 (CH_2-cy), 28.4 (CH_2-cy), 32.9 (CH_2-cy), 56.0 (N-CH_2-py), 59.3 (CH-cy), 121.8 (CH-py), 122.0 (CH-py), 136.3 (CH-py), 148.5 (CH-py), 160.8 (C-py). ^{13}C DEPT 135 (400 MHz, DMSO): δ 24.4 (CH_2-cy) neg, 25.6 (CH_2-cy) neg, 25.7 (CH_2-cy) neg, 28.4 (CH_2-cy) neg, 32.9 (CH_2-cy) neg, 56.0 (N-CH_2-py) neg, 59.3 (CH-cy) pos, 121.8 (CH-py) pos, 122.0 (CH-py) pos, 136.3 (CH-py) pos, 148.5 (CH-py) pos. IR ν_{max} (cm^{-1}): 2923 (w), 2851 (w), 1587 (w), 1440 (w), 1359 (s), 1127 (w), 754 (s), 620 (s).

NNN-phepy

The NNN-phepy ligand was prepared analogously to NNN-propy in a scaled up one-pot synthesis using the following masses and volumes, added in the following sequence: potassium carbonate (12 g) in 85 mL acetonitrile, 2-chloromethylpyridine hydrochloride (4.0 g, 24.39 mmol), aniline (0.74 mL, 8.10 mmol) and TBAB (0.10 g). A thick dark brown oil was obtained after passing the crude product through a silica packed column and eluting with 1:1 (v/v) hexane/ethyl acetate (1.05 g, 16% based on 2-chloromethyl pyridine HCl). ^{1}H NMR (400 MHz, $CDCl_3$): δ 4.3 (s, 4H, N-CH_2-py), 6.5 (m, 1H, CH-ph), 7.1 (m, 4H, CH-ph), 7.2 (m, 2H, CH-py), 7.4 (d, 2H, *J*= 8.0 Hz, CH-py), 7.7 (ddd, 2H, *J*= 8.4, 7.6, 1.7 Hz, CH-py), 8.5 (d, 2H, *J*= 4.8 Hz, CH-py). ^{13}C NMR (400 MHz, DMSO): δ 48.5 (N-CH_2-py), 112.3 (CH-ph), 115.9 (CH-py), 121.1 (CH-ph), 121.9 (CH-py), 128.8 (CH-ph), 136.6 (CH-py), 148.4 (CH-py), 148.8 (C-ph), 159.7 (C-py). ^{13}C DEPT 135 (400 MHz, DMSO): δ 48.4 (N-CH_2-py) neg, 112.2 (CH-ph) pos, 116.0 (CH-ph) pos, 121.2 (2xCH-py) pos, 128.8 (CH-ph) pos, 136.8 (CH-py) pos, 148.7 (CH-py) pos. IR ν_{max} (cm^{-1}): 2926 (w), 1602 (w), 1499(w), 1243 (w), 1046 (w), 746 (s), 691 (s).

2.2.3.2 Preparation of NNN complexes

2.2.3.2.1 Preparation of Ru and Co NNN complexes

For all variations of the NNN ligands described herein, there is little to no literature on Ru and Co complexes prepared from these ligands. The aim was to synthesise mononuclear based catalysts from a reaction of the respective metal precursor (either $CoCl_2.6H_2O$ or $[(\eta^6\text{-}C_6H_6)Ru(\mu\text{-}Cl)Cl]_2$) with varying ligands, in a 1:1 ratio. A general structure of the Ru series of complexes (**RI**-**RIV**) is represented in Fig. 2.2 with a general coding assigned to each complex, i.e. Ru NNN-propy (**RI**), Ru NNN-tbutpy (**RII**), Ru NNN-cypy (**RIII**) and Ru NNN-phepy (**RIV**), where **R** defines the Ru metal and **I**-**IV** represents the first set of compounds. Fig. 2.3 shows a general structure of the Co series of compounds coded as follows: Co NNN-propy (**CV**), Co NNN-tbutpy (**CVI**), Co NNN-cypy (**CVII**) and Co NNN-phepy (**CVIII**), where **C** defines the Co metal and **V**-**VIII** represents the second set of synthesised compounds. A description of the individual compounds and yields are shown in Table 2.1 (for the Ru complexes) and Table 2.2 (for the Co complexes). A general procedure is reported herein, highlighting the synthesis of the Ru precursor and each series of compounds.

Ru precursor

The $[(\eta^6\text{-}C_6H_6)Ru(\mu\text{-}Cl)Cl]_2$ dimer was synthesised in a similar manner to the report by Bennet *et al*[16]. To a 100 mL nitrogen saturated round bottom flask, 0.5 g $RuCl_3.xH_2O$ was added in 25 mL ethanol. The mixture was allowed to stir, after which 2.5 mL of 1,4-cyclohexadiene was added. The brown precipitate, which formed after a 4 h reflux, was collected under vacuum filtration and washed with a small portion of methanol. The resultant solid was dried *in vacuo* for several hours.

Ru complexes (RI-RIV)

The synthetic procedures used in the preparation of all Ru complexes were adapted from a procedure reported by Mishra *et al*[17]. To a 100 mL round bottom flask containing a mixture of the ligand in 40 mL of methanol, $[(\eta^6\text{-}C_6H_6)Ru(\mu\text{-}Cl)Cl]_2$ was added in half the ratio of the added ligand. The mixture was allowed to stir at room temperature for 24 hours during which the colour of the solution changed to a brownish-green colour (for complexes **RI** and **RIV**) and a yellow-orange colour for complexes **RII** and **RIII**. The solution was concentrated to ~7 mL after which $NH_4PF_6^-$ was added (in a ratio equivalent to that of the ligand) and stirred for 1 hour. The resulting precipitate was filtered and washed with a small portion of cold methanol and diethyl ether. The coloured product (crude) in each case was purified by dissolving the solid in acetonitrile, filtering off the undissolved material and precipitating the product with diethyl ether. The solids were dried *in vacuo* for several hours and recrystallised by diffusion of diethyl ether into a concentrated acetonitrile solution, yielding crystals suitable for X-ray diffraction.

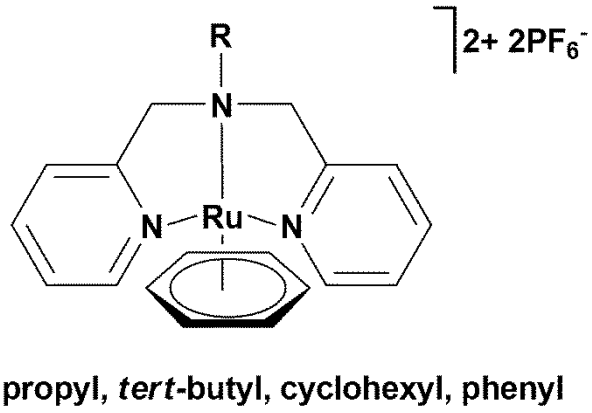

Figure 2.2: General structure of the Ru complexes with varying R substituents.

Table 2.1: Physical properties and yields obtained for each Ru complex.

Name	Description	Yield
RI	Dark green crystalline solid	0.32 g, 75%
RII	Mustard powder	0.27 g, 94%
RIII	Yellow powder	0.21 g, 79%
RIV	Dark brown solid	0.26 g, 95%

Co complexes (CV-CVIII)

To an argon saturated 100 mL round bottom flask (RBF) containing the ligand in 10 mL of methanol, a solution of $CoCl_2.6H_2O$ (0.39 g) in 10 mL of methanol was added dropwise in a 1:1 ratio. The mixture was stirred for 24 hours at room temperature, after which a deep purple coloured precipitate was observed for complexes **CV** and **CVII,** whilst concentrating the mixture of complex **CVI** and allowing it to stand overnight, resulted in the growth of blue crystals. In the case of complex **CVIII**, the product was precipitated out of solution with diethyl ether. The solid obtained in each case was collected under vacuum filtration and washed several times with diethyl ether. Each of the solids obtained through filtration (complexes **CV**, **CVII** and **CVIII**) and decantation (complex **CVI**), was dried *in vacuo* for several hours. These complexes were recrystallised through layering a concentrated DCM solution (complexes **CV** and **CVI**) with diethyl ether, a DMSO solution (complex **CVII**) with hexane and a methanol solution for complex **CVIII**, with diethyl ether. Single crystals for complex **CV**, that were suitable for single crystal XRD, were formed.

Table 2.2: Physical properties and yields obtained for each Co complex.

Name	Description	Yield
CV	Deep purple crystalline solid	0.38 g, 62%
CVI	Deep blue crystals	0.15 g, 49%
CVII	Deep purple powder	0.37 g, 63%
CVIII	Dark green powder	0.16 g, 55%

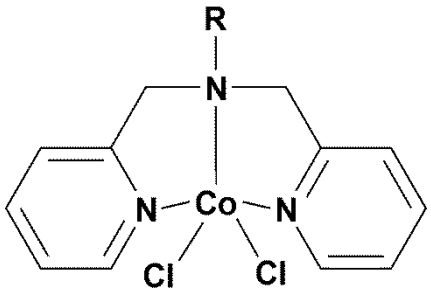

R= propyl, *tert*-butyl, cyclohexyl, phenyl

Figure 2.3: General structure of the Co complexes with varying R substituents.

2.3 Results and discussion

2.3.1 Ligands

All ligands were prepared by reacting the chlorinated pyridine precursor with the respective amine substituent. All protocols used to prepare the NNN ligands were taken from literature without any further modifications[6, 14, 15].

Pyridine based NNN ligands

The NNN ligands containing propyl, *tert*-butyl, cyclohexyl and phenyl groups were prepared by reacting the respective deprotonated amine with the ligand precursor, in a 1:2 ratio, with exception of NNN-propy which was synthesised using a 1:3 ratio. In two cases, for the ligands containing the propyl and phenyl moieties on the central N-donor atom, excess ligand together with the phase transfer catalyst tetrabutylammonium bromide (TBAB), was used to ensure formation of a disubstituted ligand. In most instances, when monosubstituted ligands form, i.e. when there is an amide proton present, reactivity of this proton is generally low (Scheme. 2.1). Further reaction with strong bases like sodium hydride are required to remove the amide proton in order to form a disubstituted ligand. However, the presence of TBAB drives the reaction to form the disubstituted ligands, making them more susceptible to form stable pincer complexes.

acyl chlorides > anhydrides > aldehydes > ketones > esters > amides > carboxylic acids

Scheme 2.1: Reactivity trends of various functional groups[18].

NMR analysis

The main analysis tool used in structural elucidation, as well as in assessing the compound's purity, was NMR spectroscopy. The representative peaks of the synthesised compounds were identified through a series of NMR spectroscopic methods, including ^{1}H NMR, ^{13}C NMR, ^{13}C DEPT 135 NMR and ^{13}C APT NMR.

All significant peaks were integrated relative to the protons on the amine backbone or, in some cases, integrated relative to the methylene protons. The presence of the *tert*-butyl protons furthermost upfield, appearing as a singlet at around 1.1 ppm and integrating to nine protons, as well as the four protons arising from the methylene linker between the amine and pyridine ring (appearing at around 3.9 ppm), confirmed a successful synthesis of one typical ligand (NNN-tbutpy). A typical ^{1}H NMR spectrum, of the NNN-tbutpy ligand, is presented below (Fig. 2.4). The remaining spectra of the ligands can be found in Appendix A2 (Figs. A2.3-A2.20).

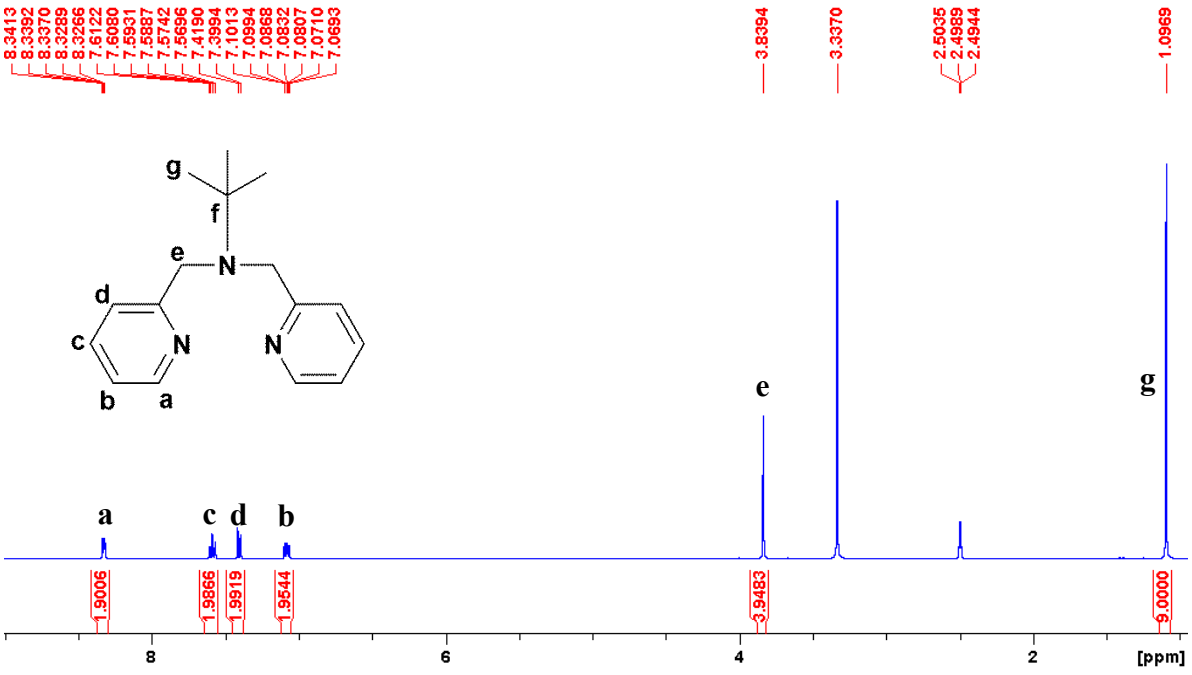

Figure 2.4: ^{1}H NMR spectrum of NNN-tbutpy.

The ^{13}C DEPT 135 NMR was a technique that provided clear and concise information on the ligand structures, and confirmed the information gained from the conventional ^{13}C NMR. This technique was effective in that the peaks observed are of the carbons to which hydrogens are bonded and, therefore, quarternary carbons, which are seen in ^{13}C CPD and

APT experiments, are absent in these. The ^{13}C DEPT 135 NMR of the NNN-tbutpy ligand is presented in Fig. 2.5 in which all CH and CH_3 peaks of the pyridine and amine fragments appear above (positive) the baseline, with the CH_2 depicted as negative.

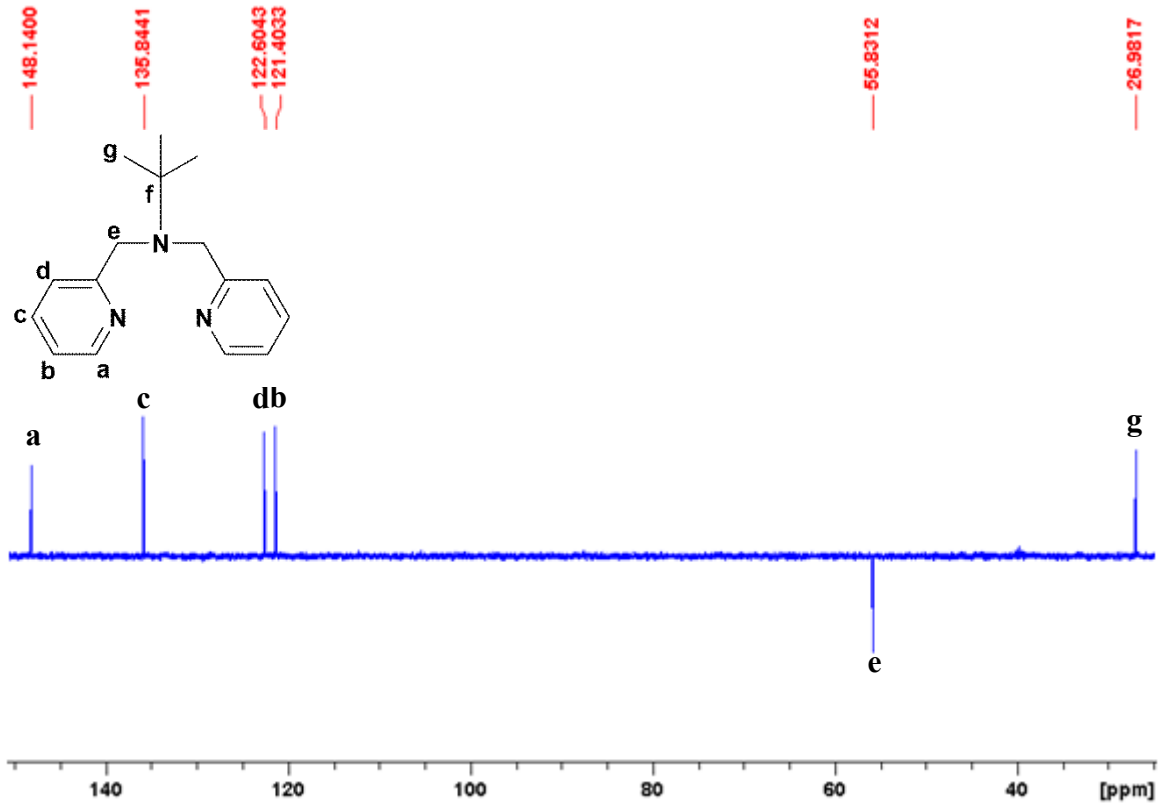

Figure 2.5: ^{13}C DEPT 135 NMR spectrum of NNN-tbutpy with CH, CH_3 (positive) and CH_2 (negative).

IR analysis

Significant wave numbers, which are due to the various functional groups of the pyridine based NNN ligands, are shown in Table 2.3. Signal strength of each characteristic functional group is represented as follows: a (most intense), b (medium intensity), c (weak) and d (broad and very strong). The characteristic bands presented are those assigned to the C-H alkyl asymmetric and symmetric stretching vibrations, typically in the region 2825-2958 cm^{-1},[19] with the C-C aromatic stretches appearing in the region 1570-1440 cm^{-1}.[20] The C-N stretching vibration occurs in the region of 1300-900 cm^{-1}, with the C-H rocking vibrations occurring in the region 750-720 cm^{-1}.[21]

Table 2.3: IR data for the pyridine based NNN ligands showing functional group wave numbers in cm[1].

Ligand	**IR ν_{max}/cm^{-1}**				
	C-H (alkyl)[c]	**C-C (aromatic)[a]**	**C-H bend (alkyl)[b]**	**C-N[b]**	**C-H (rocking)[d]**
NNN-propy	2959, 2934, 2873	1589, 1569	1432	1047	753
NNN-tbutpy	2963, 2877, 2835	1589, 1567	1433	1197	768, 608
NNN-cypy	2945, 2926, 2854	1588, 1567	1449, 1356	1130	765, 620
NNN-phepy	3050, 2926	1602, 1571	1499	1046	746

[a] strong, [b] medium, [c] weak, [d] broad and very strong

Any observable strong and broad absorption bands appearing just over 3000 cm^{-1} are due to the stretching ν(O-H) vibration of the lattice water.[20] Bands at 1589-1567 cm^{-1} are typical of C=N stretches[22]. In addition to these bands, a weak band at 612 cm^{-1} is a result of the C-H out of plane stretching of the pyridine ring. All IR spectra of the NNN pyridine based ligands can be found in Appendix A2 (Figs. A2.38-A2.41).

MS analysis

Table 2.4 shows the mass-to-charge (m/z) ratios obtained for each NNN ligand with the calculated values presented in parentheses. This technique was a good indication for a successful ligand synthesis. The low and high resolution MS spectra showed the molecular ions as the dominant peaks (Appendix A2, Figs. A2.46-A2.49), with the exception of NNN-phepy showing fragmentation of half the ligand to give a molecular ion peak with an m/z ratio of 185.12 (Appendix A2, Fig. A2.49).

Table 2.4: The m/z ratios obtained for each NNN ligand.

Ligand	m/z (Calculated)
NNN-propy	242 (241.16)
NNN-tbutpy	256.18 (255.36)
NNN-cypy	282.20 (281.40)
NNN-phepy	274.13 (275.35)

2.3.2 Complexes

2.3.2.1 Ru and Co NNN-pyridine based complexes

Various techniques can be employed to ascertain whether successful complexation has occurred between the ligand and a metal. These techniques include, NMR, IR, MS, elemental analysis and single crystal XRD. The first signs of complexation can occur from an observable colour change when a concentrated solution of metal precursor is added to that of the ligand. This colour change is distinguishable from the colours of the metal precursor and that of the ligand.

In all cases of the synthesised Ru and Co NNN complexes, precipitation of the complex resulted within 24 h of addition, following stirring or standing at room temperature (in the case of the Co complex with a *tert*-butyl substituent on the nitrogen backbone). The Ru and Co complexes had distinct colour shades, different from the various coloured ligands. This indicated successful complexation of the individual NNN ligands to the $[(\eta^6\text{-}C_6H_6)Ru(\mu\text{-}Cl)Cl]_2$ or $CoCl_2.6H_2O$ metal precursors.

All complexes were obtained in good yields. All Ru and Co complexes were stable in both solution and air, except for Co NNN-tbutpy, where prolonged exposure of the crystals to air showed initial stages of decomposition by turning sticky.

Ru(+2) forms a diamagnetic low spin complex and as a result NMR studies can be carried out on such complexes. In the case of the paramagnetic, high spin Co(+2) complexes, NMR studies cannot provide information as to whether such complexes have formed, as no signals are seen in the spectra. Nevertheless, there are other techniques like IR, MS, melting point, elemental analysis and single crystal XRD, that are able to provide useful insight and proof of complex formation (discussed later).

NMR analysis of Ru NNN-pyridine based complexes

In confirming successful complex formation, noticeable resonance shifts are observed for the coordinated ligand relative to the free ligand. Successful complexation occurs *via* cleavage of the bridged chlorine atoms in the Ru metal precursor, with subsequent coordination of the individual NNN ligands.

Fig. 2.6 shows a representative ^{1}H NMR spectrum of the Ru NNN-propy complex (**RI**). The significant proton shifts are tabulated in Tables 2.5-2.8 and show marked shifts in the aromatic proton signals which appear further downfield relative to those observed in the ^{1}H NMR spectra of the ligands. This result is attributed to metal coordination.[23] Apart from these resonance shifts, a distinct singlet around 6.3 ppm, due to the protons of the benzene ring, further confirms successful complex synthesis.

Noticeably, all Ru complex spectra show a rearrangement of two individual aromatic proton signals, each integrating to two protons, with multiplicities of a doublet and triplet, respectively. The switching of these proton signals provides substantial evidence that the desired compound was obtained. This effect is rationalised through shielding of the aromatic pyridine rings by the electron rich benzene ring resulting from complexation.[24] Furthermore, this result is interpreted through polarisation of the pi cloud of the substituted pyridine rings.

The protons of the methylene linker in each of the NNN ligands give rise to a singlet integrating to four protons. This singlet, centered around 3.7 ppm in the NNN-propy ligand, splits into two doublets with the first appearing around 4.8 ppm and the other at 4.4 ppm. This outcome is due to the presence of two diastereotopic protons, one being axial, whilst the other is equatorial[5, 17, 19, 2]. Moreover, the methylene linker separating the aliphatic and pyridine fragments of the ligand is affected by the arrangement or planarity of the substituent on the central N-donor atom. Therefore, the split CH_2 signal is also due to the pyridine rings and nitrogen substituent (aliphatic groups) appearing in two different planes to each other.[26]

In complex **RIII**, the signal comprising of the furthermost shifted cyclohexyl C-H proton and the second doublet of the methylene linker, were indicative of a through space proton interaction existing among the cyclohexyl C-H proton and the proton on one methylene group. This was confirmed by the 2D HSQC NMR spectrum of the complex (Appendix A2, Fig. A2.31). The shift in the cyclohexyl C-H peak, integrating to a single proton, provided clarity of coordination of the central N-donor atom to the metal centre.

Furthermore, the ^{13}C APT NMR spectrum of Ru NNN-propy (Fig. 2.7) confirms successful coordination of the ligand to the metal, as seen from the sharp benzene signal centered around 88.3 ppm, together with other observable downfield carbon shifts in the aliphatic and aromatic region. All ^{13}C DEPT 135 NMR peaks of the Ru complexes were found at lower fields relative to those signals observed in the ^{13}C DEPT 135 NMR of the free ligand. The remaining Ru NMR spectra can be found in Appendix A2 (Figs. A2.21-A2.37).

Table 2.5: Proton NMR peak shifts for complex **RI** relative to the respective ligand.

Specific proton	**Peak shift (δ, ppm), multiplicity and no. of protons**	
	NNN-propy	**RI**
H-py	8.5 (d, 2H, *J*= 4.5 Hz)	9.2 (d, 2H, *J*= 5.6 Hz)
H-py	7.7 (ddd, 2H, *J*= 8.8, 7.7, 0.7 Hz)	7.9 (ddd, 2H, *J*= 8.8, 7.7, 1.0 Hz)
H-py	7.5 (d, 2H, *J*= 7.9 Hz)	7.4 (d, 2H, *J*= 7.5 Hz)
H-py	7.2 (m, 2H)	7.5 (m, 2H)
H-CH_2	3.7 (s, 4H)	4.4, 4.8 (d, 2H, *J*= 16.9 Hz; d, 2H, J= 17.4 Hz)
H-prop	2.4 (t, 2H, *J*= 7.5 Hz)	4.0 (m, 2H)
H-prop	1.4 (m, 2H)	1.8 (m, 2H)
H-prop	0.8 (t, 3H, *J*= 7.8 Hz)	1.0 (t, 3H, *J*= 7.1 Hz)

Table 2.6: Proton NMR peak shifts for complex **RII** relative to the respective ligand.

Specific proton	Peak shift (δ, ppm), multiplicity and no. of protons	
	NNN-tbutpy	**RII**
H-py	8.3 (d, 2H, *J*= 4.5 Hz)	9.3 (d, 2H, *J*= 6.2 Hz)
H-py	7.6 (ddd, 2H, *J*= 8.3, 7.8, 1.5 Hz)	8.0 (ddd, 2H, *J*= 8.8, 7.7, 1.0 Hz)
H-py	7.4 (d, 2H, *J*= 7.8 Hz)	7.5 (d, 2H, *J*= 7.8 Hz)
H-py	7.1 (ddd, 2H, *J*= 7.6, 6.0, 0.8 Hz)	7.6 (ddd, 2H, *J*= 7.7, 6.5, 0.9 Hz)
H-CH_2	3.8 (s, 4H)	3.9, 4.9 (d, 2H, *J*= 17.3 Hz; d, 2H, *J*= 17.2 Hz)
H-tbutyl	1.1 (s, 9H)	1.6 (s, 9H)

Table 2.7: Proton NMR peak shifts of the complex **RIII** relative to the respective ligand.

Specific proton	Peak shift (δ, ppm), multiplicity and no. of protons	
	NNN-cypy	**RIII**
H-py	8.4 (d, 2H, *J*= 4.9 Hz)	9.3 (d, 2H, *J*= 5.6 Hz)
H-py	7.7 (ddd, 2H, *J*= 8.6, 7.8, 1.7 Hz)	8.1 (ddd, 2H, *J*= 8.6, 8.0, 1.5 Hz)
H-py	7.5 (d, 2H, *J*= 7.6 Hz)	7.6 (d, 2H, *J*= 7.8 Hz)
H-py	7.2 (ddd, 2H, *J*= 7.6, 3.8, 1.1 Hz)	7.6 (ddd, 2H, *J*= 7.8, 6.8, 1.0 Hz)
H-CH_2	3.8 (s, 4H)	4.0, 4.8 (d, 2H, *J*= 17.3 Hz; d, 2H, *J*= 15.6 Hz)
H-cy	2.4 (m, 2H)	4.1 (m, 2H)
H-cy	1.8 (d, 2H, *J*= 12.6 Hz)	2.2 (m, 2H)
H-cy	1.7 (m, 2H)	1.8 (m, 2H)
H-cy	1.5 (m, 2H)	1.7 (m, 2H)
H-cy	1.3 (q, 2H, *J*= 11.1 Hz)	1.6 (q, 2H, *J*= 9.1 Hz)
H-cy	1.1 (m, 2H)	1.2 (m, 2H)

Table 2.8: Proton NMR peak shifts of the complex **RIV** relative to the respective ligand.

Specific proton	Peak shift (δ, ppm), multiplicity and no. of protons	
	NNN-phepy	**RIV**
H-py	8.5 (d, 2H, *J*= 4.8 Hz)	9.2 (d, 2H, *J*= 5.9 Hz)
H-py	7.7 (ddd, 2H, *J*= 8.4, 7.6, 1.7 Hz)	8.1 (ddd, 2H, *J*= 8.7, 7.6, 1.5 Hz)
H-py	7.4 (d, 2H, *J*= 8.0 Hz)	7.5 (d, 2H, *J*= 7.8 Hz)
H-py	7.2 (m, 2H)	7.6 (m, 2H)
H-CH_2	4.3 (s, 4H)	4.4, 5.2 (d, 1H, *J*= 14.9 Hz; m, 1H)
H-ph	7.1 (m, 4H)	7.6 (m, 4H)
H-ph	6.5 (m, 1H)	7.4 (m, 1H)

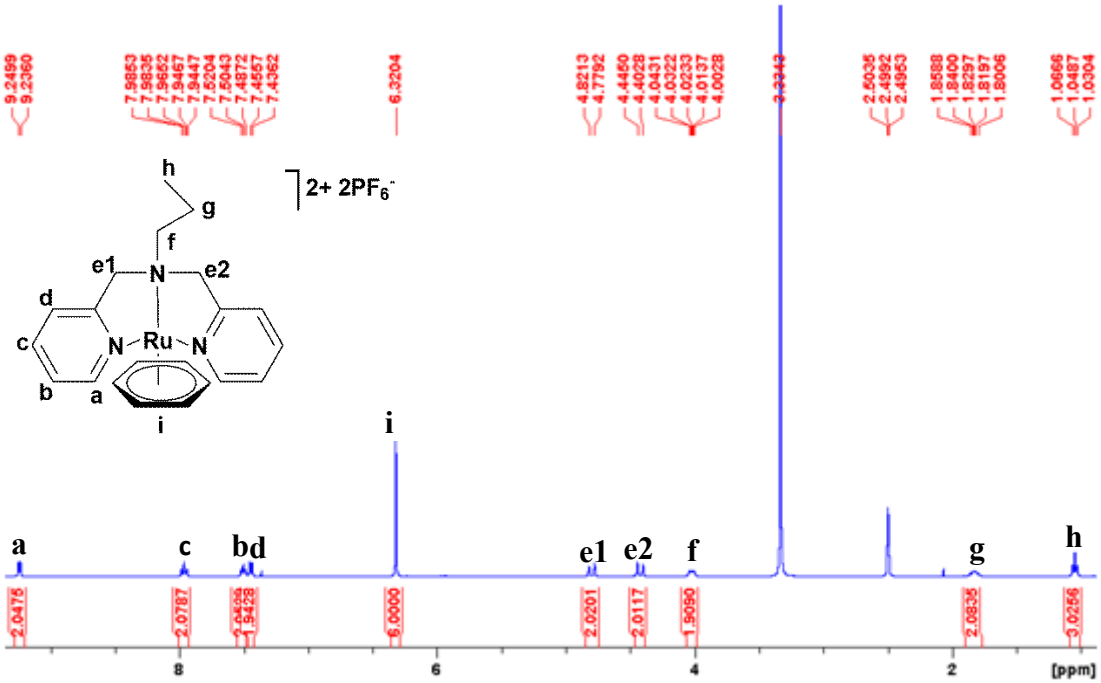

Figure 2.6: ^{1}H NMR spectrum of Ru NNN-propy.

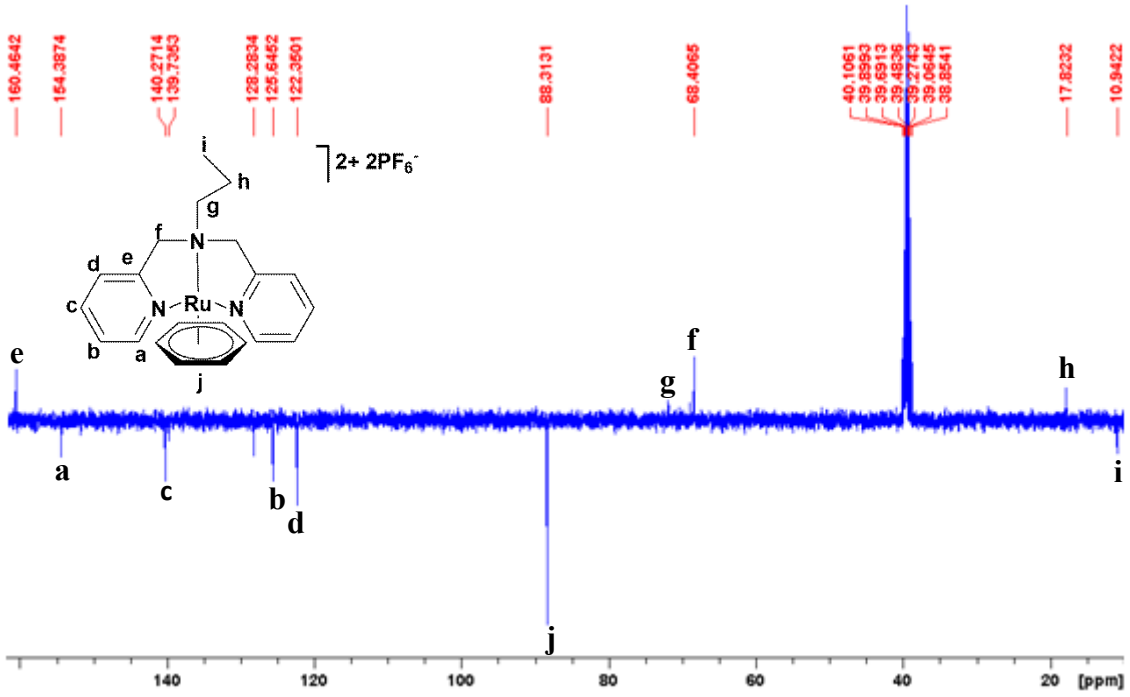

Figure 2.7: ^{13}C APT NMR spectrum of Ru NNN-propy.

IR analysis of Ru and Co NNN-pyridine based complexes

The IR spectra of the NNN ligands and the metal complexes were compared to further confirm the synthesis of the intended complexes. Any band shifts seen for the complexes from those of the ligands were a clear indication that the complexes indeed formed. Medium intensity C-H bands, due to sp^2 and sp^3 hybridised groups in the alkyl region, are shifted to higher wavenumbers for both the Ru and Co complexes. Apart from these shifts, bands in the C-C aromatic region of the Co complexes, and particularly the C=N vibrations of the pyridine ring, were shifted to higher wavenumbers. This result was due to the relationship between the resonant frequencies in which the bonds vibrate and that of the bond strength. In this respect, the C=N bond is strengthened by the donation of electrons from the metals, Ru^{2+} and Co^{2+} (which are hard acids that readily donate electrons), resulting in an increase in energy of the C=N bond. Reports show that the C=N shift in the aromatic region is generally large, as opposed to the corresponding peak appearing in the uncoordinated ligand.[22] This observation is noticeable in these complexes, which show coordination of the pyridine rings to the Ru or Co metals.

All other bands seen in the IR spectra of the Ru complexes were low in intensity and any possible shifts were difficult to identify and would have been based on speculation (Table

2.9). These weak bands were further masked by the intense PF_6^- band occurring at 828 cm^{-1}. [17] However, synthesis of these complexes, apart from IR results, was further confirmed though MS data and single crystal XRD results which are shown later in this report.

Table 2.9: Band shifts in the IR of the complexes relative to those observed in the ligands.

	IR ν_{max}/cm^{-1}			
	C-H (alkyl)[a]	**C-C (aromatic)[b]**	**C-H bend (alkyl)[a]**	**C-H (rocking)[c]**
NNN-propy	2959	1589	1432	753
RI	unassignable	1609	1440	779
CV	2967	1605	1443	776
NNN-tbutpy	2963	1589	1433	768
RII	unassignable	1613	1448	779
CVI	2973	1605	1438	766
NNN-cypy	2945	1588	1449	765
RIII	unassignable	1611	1461	771
CVII	2921	1606	1444	772
NNN-phepy	2926	1602	1499	746
RIV	unassignable	1597	1427	763
CVIII	3050	1600	1493	763

[a] very weak, [b] weak, [c] broad and very strong

Similar band shifts (C-C aromatic, C-H alkyl and C-H rocking vibrations) were observed among both the Ru and Co metal complexes. However, the sp^2 and sp^3 hybridised C-H bands in the Co complexes shifted to lower wave numbers, indicating that these bonds are now weaker than those in the Ru complexes. This is due to a drop in energy at which the C-H bonds vibrate. Band shifts occurring in the IR spectra of most Co complexes appeared more intense compared to similar shifts in the spectra of the Ru complexes. This result can be related to Hooke's Law which states:

$$\nu = \frac{1}{2\pi c}\sqrt{\frac{k}{\mu}}$$

and simply links the strength of a bond to the mass of the atoms involved. From this relationship, a greater shift in wavenumber (> 10 cm^{-1}) of the bands appearing in some of the Co IR spectra were seen as opposed to those in the Ru complexes. This effect is ascribed by Co having a lower atomic mass than Ru (58.93 $gmol^{-1}$ compared to 101.07 $gmol^{-1}$) and therefore the frequencies at which the bonds vibrate is larger than those of Ru resulting in a larger shift in wavenumber.

MS analysis

The mass-to-charge ratios obtained for each Ru and Co NNN complex are shown in Table 2.10 with the calculated values represented in parenthesis. In all Co complexes, with exception of **CVIII**, m/z ratios are expressed with omission of one chlorine atom originally bound to the metal, as a result of ionisation fragmentation. In the case of **CVIII**, both Cl atoms fragment giving a mass-to-charge ratio of 356.02 which includes a sodium adduct and is in close proximity to the calculated value in parenthesis. All m/z ratios of the doubly charged Ru complexes shown exclude the two PF_6^- counter ions as expected. The MS spectrum of **RI** shows that half the ligand fragments to give a peak (100% abundant) with m/z ratio of 122 (Appendix A2, Fig. A2.50). With regards to **RIV**, a bidentate ligand was synthesised and this type of coordination was confirmed through the m/z ratio of 399.01, due to the Ru-Cl NN benzene complex with the calculated mass in parenthesis. The synthesised bidentate complex exits as a mononuclear specie, since the melting point was high and sharp with a single melting stage that negates phase transition.[27]

Table 2.10: The m/z ratios obtained for the Ru and Co NNN complexes.

Complex	m/z $[M+H]^+$ (Calculated)
RI	210 (210.56)
CV	335.06 (335.06)
RII	217.56 (217.06)
CVI	349.07 (349.74)
RIII	230.57 (230.06)
CVII	375.09 (375.78)
RIV	399.01 (399.02)
CVIII	356.02 (357.08)

Elemental analysis

The elemental analysis for each complex is represented in Table 2.11 and shows that the reported values are in acceptable range to the theoretical values represented in parenthesis. The technique shows that the complexes were pure. This supports a successful synthesis of all complexes, showing that the excess ligands used in each reaction had remained in solution, providing a pure complex.

Table 2.11: The elemental analysis obtained for all complexes with calculated values in parenthesis.

Complex	%C	%H	%N
RI	36.1 (35.5)	3.1 (3.6)	5.6 (5.9)
CV	48.5 (48.5)	4.9 (5.2)	11.3 (11.3)
RII	36.0 (36.5)	3.6 (3.8)	5.2 (5.8)
CVI	45.2 (45.6)	5.2 (5.9)	9.6 (10.0)
RIII	38.8 (38.4)	4.0 (3.9)	5.5 (5.6)
CVII	52.2 (52.6)	5.7 (5.6)	10.1 (10.2)
RIV	42.9 (42.6)	3.3 (3.4)	6.0 (5.5)
CVIII	53.2 (53.4)	4.6 (4.2)	10.5 (10.4)

Melting point

The melting point of a complex gives an indication of its level of purity. This is observed from the range at which the complex melts and usually gives an indication of the amount of impurities that may be present in the complex. Impurities may be associated with a broad melting range (> 4°) and low melting point. Information on successful complex syntheses can be established through this technique prior to conducting other characterisation techniques. With this, links can be drawn from the ligand melting point compared to that of the complex in question, which ought to have a significantly higher and sharp melting point. Furthermore, information on the type of species present in the complex can be obtained. Often, a mixture of mononuclear and dinuclear species can exist in a product, each having their own melting point ranges.

Table 2.12: The melting point ranges obtained for all complexes and certain ligands.

Complex/Ligand	Melting point/ °C[a]
RI	220.7-224.8 °C
CV	279.1-281.8 °C
NNN-tbutpy	84.4-87.7 °C
RII	287.1-288.7 °C
CVI	182.1-185.6 °C
NNN-cypy	57.3-60.1 °C
RIII	237-241.3 °C
CVII	319.3-320.7 °C
RIV	237.6-241.4 °C
CVIII	209.6-211.7 °C

[a] NNN-propy and NNN-phepy are oils

Table 2.12 shows the melting point ranges of the Ru and Co complexes. All the melting points were sharp, proving that these complexes were of high purity. It can be seen that the melting point of each complex is related to the nature of substituent on the nitrogen backbone, where the highest melting points were associated with those complexes having rigid backbones (cyclohexyl and phenyl) compared to the more flexible propyl and *tert*-butyl substituted complexes.

2.4 Summary

The preparation of eight novel compounds has been achieved through adaptation of literature procedures. All Ru complexes were successfully characterised with IR, MS, melting point, elemental analysis and NMR. Due to the diamagnetic nature of the Ru compounds, noticeable shifts in characteristic NMR peaks were observed in the complex spectra compared to those of the ligands. The Co compounds were also characterised with the above mentioned techniques, however, the paramagnetic Co compounds' unresolvable NMR data is not reported in this thesis. The MS and elemental analyses were confirmation that all complexes synthesised were pure. Crystal structures of catalysts **RI**, **RII**, **RIII** and **CV** were obtained and will be discussed in the following chapter.

2.5 References

1. O. Dayan, N. Özdemir, Z. Şerbetci, M. Dinçer, B. Çetinkaya and O. Büyükgüngör, *Inorganica Chimica Acta*, 2012, **392**, 246-253.
2. D. Gallego, S. Inoue, B. Blom and M. Driess, *Organometallics*, 2014, **33**, 6885-6897.
3. S. Mollin, R. Riedel, K. Harms and E. Meggers, *Journal of Inorganic Biochemistry*, 2015, **148**, 11-21.
4. C. Li, C. Ma, P. Xu, Y. Gao, J. Zhang, R. Qiao and Y. Zhao, *The Journal of Physical Chemistry B*, 2013, **117**, 7857-7867.
5. K. Visvaganesan, R. Mayilmurugan, E. Suresh and M. Palaniandavar, *Inorganic Chemistry*, 2007, **46**, 10294-10306.
6. D. W. Wright, H. J. Mok, C. E. Dubé and W. H. Armstrong, *Inorganic Chemistry*, 1998, **37**, 3714-3718.
7. J. W. Shin, A. R. Jeong, K. S. Min, S. Hayami and D. Moon, *Inorganic Chemistry Communications*, 2015, **51**, 46-49.
8. Y. Peng, C.-B. Tian, Y.-H. Lan, N. Magnani, Q.-P. Li, H.-B. Zhang, A. K. Powell and S.-W. Du, *European Journal of Inorganic Chemistry*, 2013, **2013**, 5534-5540.
9. D. Kim, S. Kim, E. Kim, H.-J. Lee and H. Lee, *Polyhedron*, 2013, **63**, 139-146.
10. Y.-H. Zhou, J. Tao, Q.-C. Lv, W.-G. Jia, R.-R. Yun and Y. Cheng, *Inorganica Chimica Acta*, 2015, **426**, 211-220.
11. S. Lindsay, S. K. Lo, O. R. Maguire, E. Bill, M. R. Probert, S. Sproules and C. R. Hess, *Inorganic Chemistry*, 2013, **52**, 898-909.
12. P.-H. Lanoe, J.-L. Fillaut, V. Guerchais, H. Le Bozec and J. A. Gareth Williams, *European Journal of Inorganic Chemistry*, 2011, **2011**, 1255-1259.
13. M. A. H. Moelands, D. J. Schamhart, E. Folkertsma, M. Lutz, A. L. Spek and R. J. M. Klein Gebbink, *Dalton Transactions*, 2014, **43**, 6769-6785.
14. M. J. Carney, N. J. Robertson, J. A. Halfen, L. N. Zakharov and A. L. Rheingold, *Organometallics*, 2004, **23**, 6184-6190.
15. Y. Song, D. Kim, H.-J. Lee and H. Lee, *Inorganic Chemistry Communications*, 2014, **45**, 66-70.
16. M. A. Bennett and A. K. Smith, *Journal of the Chemical Society, Dalton Transactions*, 1974, 233-241.
17. H. Mishra, A. K. Patra and R. Mukherjee, *Inorganica Chimica Acta*, 2009, **362**, 483-490.

18. J. Clayden, N. Greeves, S. Warren and P. Wothers, *Organic Chemistry*, Oxford University Press 2001, 2001.
19. E. R. Milaeva, D. B. Shpakovsky, Y. A. Gracheva, S. I. Orlova, V. V. Maduar, B. N. Tarasevich, N. N. Meleshonkova, L. G. Dubova and E. F. Shevtsova, *Dalton Transactions*, 2013, **42**, 6817-6828.
20. F. R. Louka, M. L. Spell, J. Grebowicz, J. H. Albering, F. A. Mautner and S. S. Massoud, *Journal of Molecular Structure*, 2011, **995**, 103-108.
21. J. P. Coates, *Encyclopedia of Analytical Chemistry*, 2000, 8217-8240.
22. C. Xu, X.-C. Liu, X.-D. Jin, Q. Yang, G.-C. Han, Y.-C. Gang and H.-H. Hu, *Journal of Coordination Chemistry*, 2014, **67**, 352-362.
23. D. Gonzalez Cabrera, B. D. Koivisto and D. A. Leigh, *Chemical Communications*, 2007, 4218-4220.
24. N. H. Martin, R. M. Floyd, H. L. Woodcock, S. Huffman and C. K. Lee, *Journal of Molecular Graphics & Modelling*, 2008, **26**, 1125-1130.
25. O. Rivada-Wheelaghan, A. Dauth, G. Leitus, Y. Diskin-Posner and D. Milstein, *Inorganic Chemistry*, 2015, **54**, 4526-4538.
26. D. Kim, S. Kim, E. Kim, H.-J. Lee and H. Lee, *Polyhedron*, 2013, **63**, 139-146.
27. L. Soobramoney, M. D. Bala and H. B. Friedrich, *Dalton Transactions*, 2014, **43**, 15968-15978.

Chapter Three

Crystal structures of selected Ru and Co complexes

3.1 Introduction

X-ray crystallography is a widely used technique for examining the atomic arrangement in a molecule. Fundamental information can be gathered on specific positions of atoms in the crystal unit, their size, the length and angles of chemical bonds, as well as evidence of disorder in the crystal. Also, the geometry of the compound in question, together with any planarity existing among two individual fragments, can be ascertained. This technique is essential in the sense that some compounds have complex geometries that are too intricate to solve by common methods like IR and NMR spectroscopy.

For a three-dimensional image to be interpreted and refined, the compounds ought to be crystalline for the X-ray beam to diffract into specific directions. It is, therefore, crucial that compounds are crystalline enough for diffraction studies to be carried out and for atoms to arrange themselves in an ordered fashion. Sometimes compounds can crystallise well, however, some crystals, upon microscopic inspection, may not be of a suitable quality to analyse, which could possibly be due to disorder in the crystal or the crystals may be twinned. There are various tried and tested techniques for growing suitable crystals for single crystal XRD, from layering and slow diffusion to slow evaporation. These techniques have been employed in the crystal growth for compounds **RI**, **RII**, **RIII** and **CV**.

3.2 Experimental

For the crystal structure of complex **RI**, single-crystal X-ray diffraction data were collected on a Bruker KAPPA APEX2 DUO diffractometer using graphite-monochromated Mo-Kα radiation (λ = 0.71073 Å). Data collection was carried out at 173(2) K. Temperature was controlled by an Oxford Cryostream cooling system (Oxford Cryostat) operating at a 100(1) K. Cell refinement and data reduction were performed using the program *SAINT*[1]. The data were scaled and absorption correction performed using *SADABS*[2] multi-scan technique.

The structure was solved by direct methods using *SHELXS*-2014[2] and refined by full-matrix least-squares methods based on F^2 using the graphics interface program *X-Seed*[3, 4]. The programs *X-Seed* and *POV-Ray*[5] were both used to prepare molecular graphic images.

All non-hydrogen atoms were refined anisotropically. All hydrogen atoms were placed in idealised positions and refined in riding models with U_{iso} assigned 1.2 or 1.5 times U_{eq} of their parent atoms and the bond distances were constrained in the range from 0.95 Å to 0.99 Å.

Single crystal X-ray diffraction data for complexes **RII**, **RIII** and **CV** were collected on a Bruker Smart APEX2 diffractometer with graphite monochromated Mo K_α radiation (50 kV, 30 mA and λ = 0.71073 Å) using the *APEXII*[6] data collection software. Data collection was carried out at 100(2) K. Temperature was controlled by an Oxford Cryostream cooling system (Oxford Cryostat) operating at a 100(1) K. The collection method involved ω-scans of width 0.5° and 512 x 512 bit data frames. Data reduction was carried out using the program *SAINT*[1] and the data were scaled and absorption corrections performed using *SADABS*[7] multi-scan technique. The structures were solved by direct methods using *SHELXS*[8]. Isotropic refinement was first done on non-hydrogen atoms, followed by anisotropic refinement by full-matrix least-squares methods based on F^2 using *SHELXL*[8]. Hydrogen atoms were first located in the difference map, then positioned geometrically and allowed to ride on their respective parent atoms. Diagrams and publication material were generated using *SHELXL*[8], *PLATON*[9] and *MERCURY*[10]. Reports were subjected to online check cif validation which shows no structural disorder in **RI**-**RIII** and **CV**. Table 3.1 represents selected crystal refinement data for the Ru complexes **RI**-**RIII** with structure refinement data for complex **CV** reported in Table 3.2. Supporting information on each crystal can be found in Appendix A3.

Table 3.1: Crystallographic and structure refinement data for complexes **RI**, **RII** and **RIII**.

	RI	**RII**	**RIII**
Chemical formula	$C_{21}H_{23}F_{12}N_3P_2Ru$	$C_{22}H_{27}F_{12}N_3P_2Ru$	$C_{24}H_{29}F_{12}N_3P_2Ru$
Formula weight	708.43	724.48	750.51
Crystal size (mm^3)	0.14 x 0.15 x 0.17	0.290 x 0.160 x 0.130	0.230 x 0.180 x 0.110
Crystal system	Monoclinic	Monoclinic	Monoclinic
Space group	$P2_1/c$	$P2_1/c$	$P2_1/c$
Unit cell dimensions			
a (Å), α (º)	8.8604(7), 90	10.4929(7), 90	9.8297(4), 90
b (Å), β (º)	18.2578(13), 96.950(2)	14.5886(11), 92.510(2)	14.3986(6), 114.967(2)
c (Å), γ (º)	16.0917(12), 90	17.2377(13), 90	10.5116(4), 90
Volume ($Å^3$)	2584.1(3)	2636.2(3)	1348.72(10)
Z	4	4	2
σ_{calc} ($Mg\ m^{-3}$)	1.821	1.825	1.848
Absorption coefficient (mm^{-1})	0.835	0.820	0.805
F(000)	1408	1448	752
Theta range for data collection (°)	1.7 to 27.9	1.829 to 28.307	2.137 to 28.348
Index ranges	-11≤ h≤10	-13≤h≤14	-12≤h≤13
	-24≤ h≤24	-19≤k≤=17	-19≤k≤19
	-21≤ h≤21	-21≤l≤22	-14≤l≤14
Reflections collected	30308	21606	26345
Independent reflections	6197 [R(int) = 0.071]	6456 [R(int) = 0.0364]	6452 [R(int) = 0.0359]
Completeness to theta (%)	99.9	99.8	100.0
Max. and min. transmission	0.906 and 1.000	0.911 and 0.790	0.928 and 0.825
Data / restraints / parameters	6197 / 0 / 353	6456 / 0 / 363	6452 / 1 / 379

Goodness-of-fit on F^2	1.02	1.023	1.057
Final R indices [I>2σ(I)]	R1 = 0.0389, wR2 = 0.0993	R1 = 0.0483, wR2 = 0.1113	R1 = 0.0396, wR2 = 0.0908
R indices (all data)	N/A	R1 = 0.0625, wR2 = 0.1183	R1 = 0.0426, wR2 = 0.0922
Largest diff. peak and hole ($eÅ^{-3}$)	-0.64 and 0.83	1.310 and -1.092	1.125 and -0.650

Table 3.2: Crystallographic and structure refinement data for complex **CV**.

	CV
Chemical formula	$C_{15}H_{21}Cl_2CoN_3$
Formula weight	389.18
Crystal size (mm^3)	0.080 x 0.180 x 0.200
Crystal system	Triclinic
Space group	*P*1
Unit cell dimensions	
a (Å), α (º)	7.9230(2), 87.5750(10)
b (Å), β (º)	13.8852(3), 86.637(2)
c (Å), γ (º)	15.2566(4), 8.2600(10)
Volume ($Å^3$)	1673.37(7)
Z	4
σ_{calc} (Mg m^{-3})	1.545
Absorption coefficient (mm^{-1})	1.349
F(000)	804
Theta range for data collection (°)	2.68 to 28.36
Index ranges	-10≤h≤10
	-18≤k≤18
	-20≤l≤20

Reflections collected	40307
Independent reflections	8277 [R(int) = 0.0322]
Completeness to theta	98.8
Max. and min. transmission	0.9009 and 0.7751
Data / restraints / parameters	8277 / 0/ 381
Goodness-of-fit on F^2	1.012
Final R indices [I>2σ(I)]	R1 = 0.0572, wR2 = 0.1614
R indices (all data)	R1 = 0.0635, wR2 = 0.1656
Largest diff. peak and hole ($eÅ^{-3}$)	1.674 and -0.754

3.2.1 Crystal structures

3.2.1.1 Crystal structure of RI

Dark green rod-like crystals of **RI** were grown overnight through a process of vapour diffusion into a concentrated acetonitrile solution. Complex **RI** crystallises in the monoclinic $P2_1/c$ space group and, as represented by the crystal structure, exists in a monomeric state in the asymmetric unit cell. Fig. 3.1 shows the single crystal structure of complex **RI**. Compound **RI** exists as a monomer partially due to the hard electron donating N-donor atoms stabilising the metal centre. Hence, the propensity of the complex to dimerise is low and it thus forms a monomeric molecule.[11]

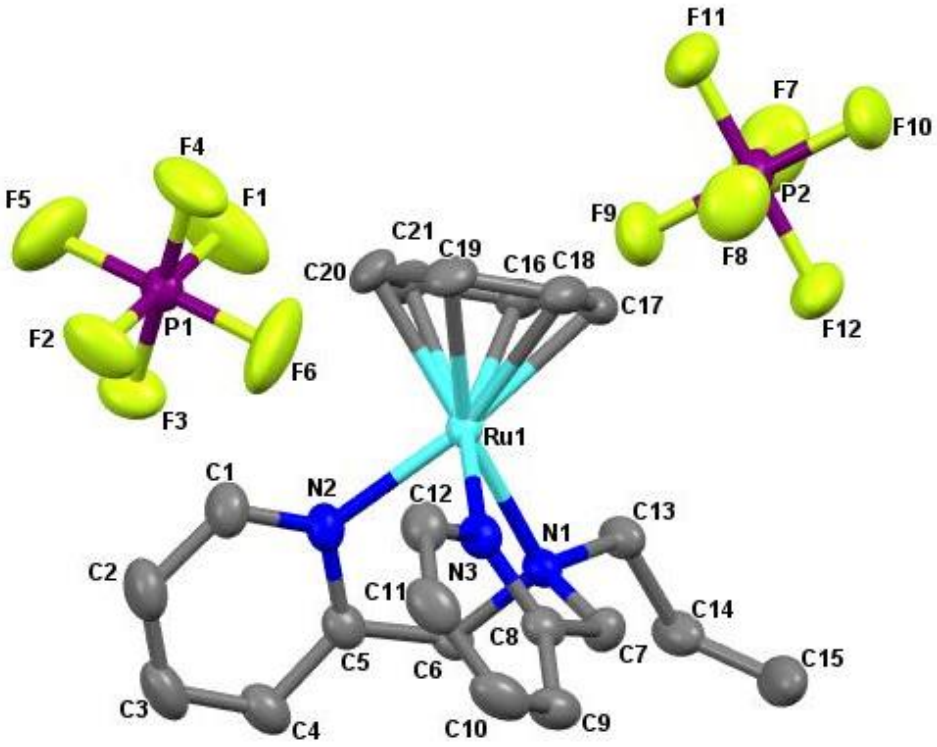

Figure 3.1: Single crystal structure of complex **RI** drawn at 50% thermal ellipsoid probability, with omission of hydrogen atoms for clarity.

The crystal structure depicted in Fig. 3.1 exhibits a piano stool geometry[12, 13] in which the Ru atom binds to three N-donor atoms, in a terdentate fashion, and to the electron rich benzene ring. The NNN coordinating ligand occupies the positions as the legs of the piano stool, whilst the benzene ring, occupying the remaining coordination site, takes up the position as the seat of the piano stool.

It is evident that complex **RI** exists as a highly unsymmetrical molecule with the two pyridyl rings and the propyl group lying in three different planes relative to each other. This correlates to the observation reported in the NMR spectrum (Chapter 2) of complex **RI**, where the methylene protons are spilt into an AB quartet, originally seen as a singlet in the ligand spectrum.

Table 3.3 shows selected bond lengths and bond angles of complex **RI**. The closest reported example resembling the crystal structure of complex **RI** is a half sandwich complex of a $((\eta^6\text{-}C_6H_6)Ru)^{2+}$ moiety with a symmetrical NNN-methylamine ligand.[12] The Ru-C bond distances in **RI**, i.e. the distances of the benzene ring carbons to the Ru^{2+} ion, range from 2.205(3) Å to 2.220(3) Å. This shows that the benzene ring is more weakly bound to the metal ion in

comparison to the reported Ru-C bond distances of 2.196(4)-2.212(4) Å of the NNN-methylamine $((\eta^6\text{-}C_6H_6)Ru)^{2+}$ complex. This implies that the Ru^{2+} centre draws more electron density from the benzene ring, thus making the Ru^{2+}-coordinated benzene ring more electrophilic.[12, 14] The Ru-Cg distance (the distance of the Ru to the midpoint of the benzene ring) of 1.462 Å, is comparable to the Ru-Cg distance of 1.463 Å recorded for **RIII** (reported later).

Table 3.3: Selected bond lengths (Å) and angles (º) for complex **RI**.

Bond lengths (Å)	
N(1)-Ru(1)	2.173(2)
N(2)-Ru(1)	2.098(3)
N(3)-Ru(1)	2.082(3)
Bond angles (º)	
N(2)-Ru(1)-N(3)	79.05(10)
N(2)-Ru(1)-N(1)	80.63(10)
N(3)-Ru(1)-N(1)	79.24(10)

Slight geometric differences are noted between reported examples of Ru(II) half sandwich complexes with related bond distances and bond angles reported herein. For instance, the Ru(1)-N(1) distance found for complex **RI**, with a value of 2.173(2) Å, is slightly longer compared to 2.152(3) Å reported for the NNN-methylamine $((\eta^6\text{-}C_6H_6)Ru)^{2+}$ complex.[12] The Ru-N(py) distances of 2.098(3) Å and 2.082(3) Å are comparable to similar distances of 2.091(3) Å and 2.087(3) Å reported. It is worth noting that the symmetric NNN ligand binds strongly to the Ru metal as revealed from the metric parameters presented in Table 3.3.

The bite angle, which is defined by the ligand-metal-ligand angle, is in this case the N(py)-Ru-N(py) angle. Angles of 79.24(10)° and 80.63(10)° for the N(3)-Ru(1)-N(1) and N(2)-Ru(1)-N(1) are relatively acute and therefore reveal that the metal is in a more compact coordination sphere. These bite angle values are comparable to similar values (79.58° and 80.06°) reported for the similar Ru NNN complex.[12]

The two pyridyl rings, N(2), C(1), C(2), C(3), C(4), C(5) and N(3), C(8), C(9), C(10), C(11), C(12) are seen at an acute angle of 63.34°. It is seen from Fig. 3.1, that these aromatic rings

lie along the face of their individual planes. Furthermore, due to the slight twisting of the methylene linker, the pyridyl rings relative to each other, as well as the methyl moiety, are all non-co-planar to one another.

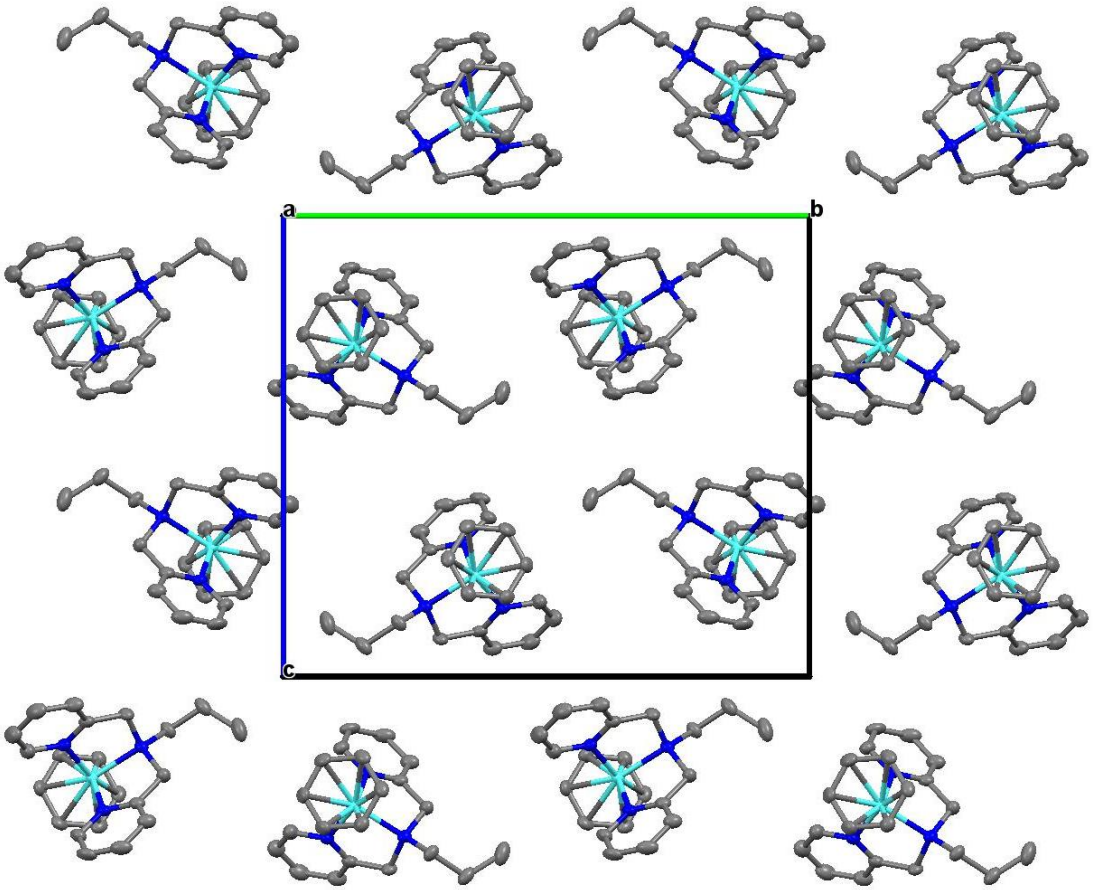

Figure 3.2: The crystal packing diagram of complex **RI** viewed along the crystallographic *a*-axis, with the hydrogen atoms and PF_6^- counterions omitted for clarity.

From Fig. 3.2, which shows the crystal packing of complex **RI**, it is seen that the arrangement of each crystal is ordered in alternating rows. Due to the propyl group being flexible, it has a higher degree of freedom and therefore can rotate freely. The crystal structure of **RI** features mainly C-H…F intermolecular interactions, where an F atom on the PF_6^- counterion is linked to a methylene C-**H** atom on one **RI** molecule (C(6)-H(6B)…F(2)) with a second F atom interacting with a pyridyl C-**H** atom on a neighbouring **RI** molecule (C(12)-H(12)…F(6)). Furthermore, two F atoms on different counterions interact (through intermolecular C-H…F hydrogen bonds) with two different benzene C-**H** atoms on one molecule, C(16)-H(16)…F(10) and C(17)-H(17)…F(7) interactions (Fig. 3.3).

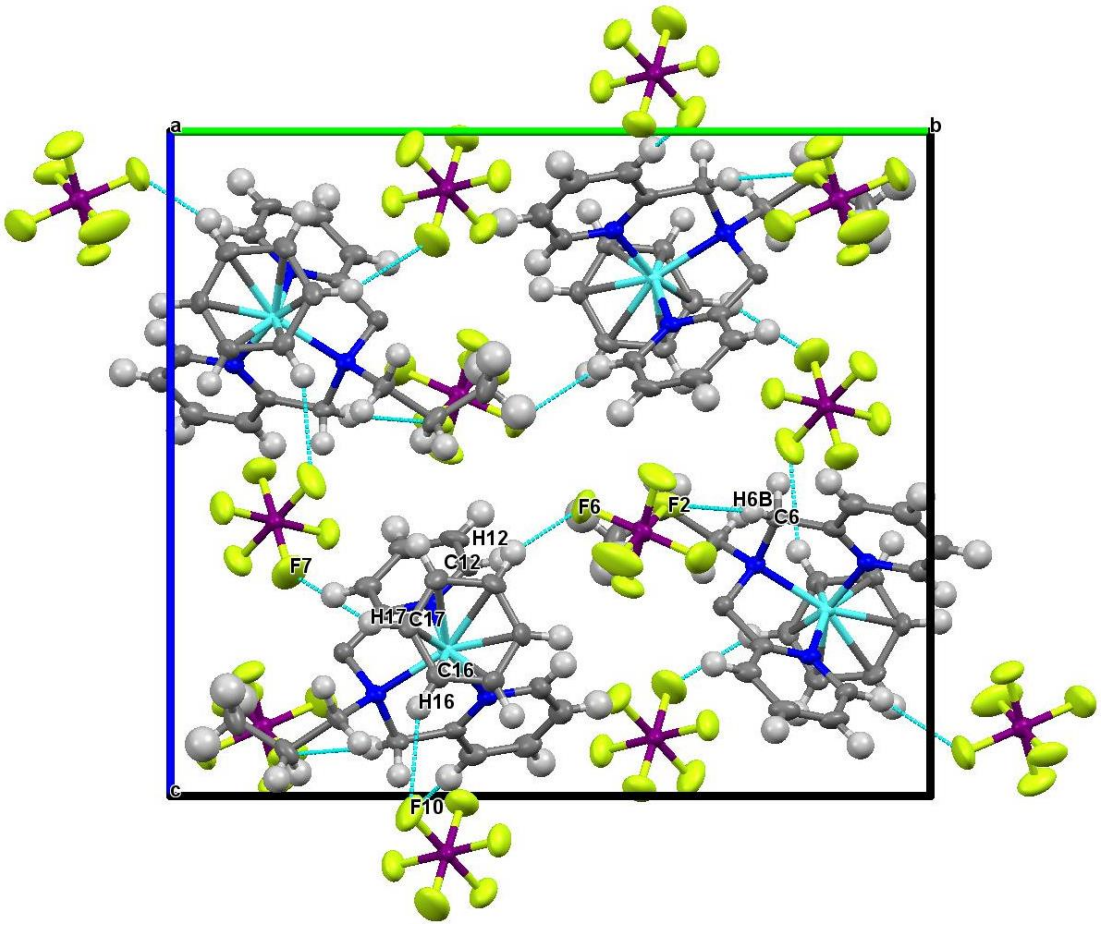

Figure 3.3: The hydrogen bonding patterns (blue lines) present in **RI**, viewed along the crystallographic *a*-axis.

3.2.1.2 Crystal structure of RII

Bright-yellow single crystals of complex **RII** were obtained over a week through vapour diffusion of a concentrated acetonitrile solution, crystallising in the monoclinic $P2_1/c$ space group. The crystal structure of complex **RII** is represented in Fig. 3.4.

As with **RI**, the crystal structure of complex **RII**, presented in Fig. 3.4, displays a piano stool or half sandwich geometry. From the structure, the ligand is highly symmetrical and binds to the Ru in a terdentate fashion. Furthermore, complex **RII** exists as a monomer for the same rationale as presented for complex **RI**, whereby the metal centre is electron rich because of electrons donated to it from the three N-donor atoms, which stabilises the Ru ion. Thus, dimerisation of the molecule is hindered as expected.

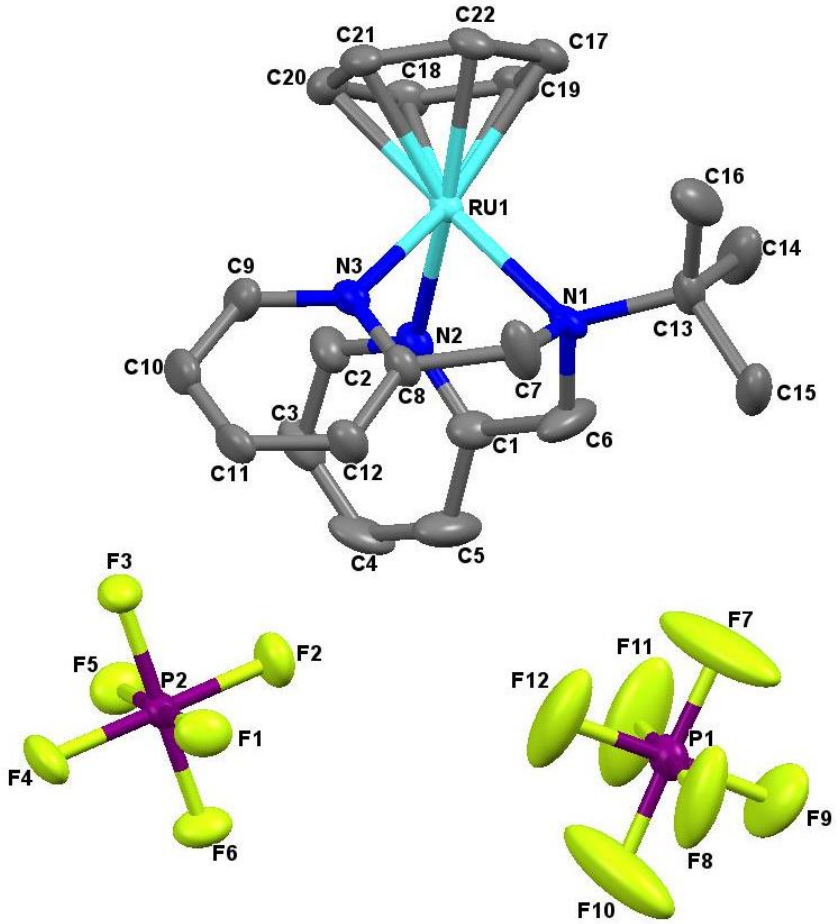

Figure 3.4: Single crystal structure of complex **RII** drawn at 50% thermal ellipsoid probability, with omission of hydrogen atoms for clarity.

Correlating the crystal structure of **RII** to its NMR spectrum, the aromatics (pyridyl rings) and bulky nature of the aliphatic moiety (*tert*-butyl group) induce non-co-planarity among the individual fragments. Hence, a change in the NMR splitting pattern of the methylene singlet in the ligand, to an AB quartet in the complex, was apparent in the respective NMR spectra (Chapter 2).

Selected bond distances and angles of complex **RII** are tabulated in Table 3.4. Geometric differences between complex **RII** and literature examples, and with complex **RI**, were noted. The Ru-Cg distance recorded was 1.470 Å, and this value compared to the Ru-Cg distances of 1.462 Å and 1.463 Å for compounds **RI** and **RIII** respectively, show that the benzene ring in this case, is bound most weakly to the metal ion and thus the electron density at the metal centre is reduced. In addition, due to elongation of the N(1)-Ru(1) bond (2.242(3) Å) bearing the *tert*-butyl moiety, there is a weaker electron flow to the metal centre, despite the *tert*-butyl group being a good source of electron density. Hence, the majority of the electrons are

supplied from the pyridyl rings as evidenced by their shorter bond distances of 2.082(3) Å for the N(2)-Ru(1) bond and 2.089(3) Å for the N(3)-Ru(1) bond.

The bite angles defined by the N(2)-Ru(1)-N(1) and N(3)-Ru(1)-N(1) angles of 79.23(12)º and 78.66(12)º respectively, deviate somewhat from a 90º terdentate facial coordination. These values are comparable to the ones found for **RI** (79.24º and 80.63º, respectively) and to the values reported for a similar Ru NNN complex which have bond angles of 79.58º and 80.06º, respectively.[12]

The planes along which the two pyridyl rings [N(2), C(1), C(2), C(3), C(4), C(5) and N(3), C(8), C(9), C(10), C(11), C(12)] are seen at a dihedral angle of 63.13º, which is more or less the same as the dihedral angle of 63.34º for the aromatics in complex **RI**. Also, noticeable is the highly ordered packing of the crystal unit, with well-ordered structures in alternating rows as shown in Fig. 3.5.

Table 3.4: Selected bond lengths (Å) and angles (º) for complex **RII**.

Bond lengths (Å)	
N(1)-Ru(1)	2.242(3)
N(2)-Ru(1)	2.082(3)
N(3)-Ru(1)	2.089(3)
Bond angles (º)	
N(2)-Ru(1)-N(3)	78.66(12)
N(2)-Ru(1)-N(1)	79.23(12)
N(3)-Ru(1)-N(1)	78.66(12)

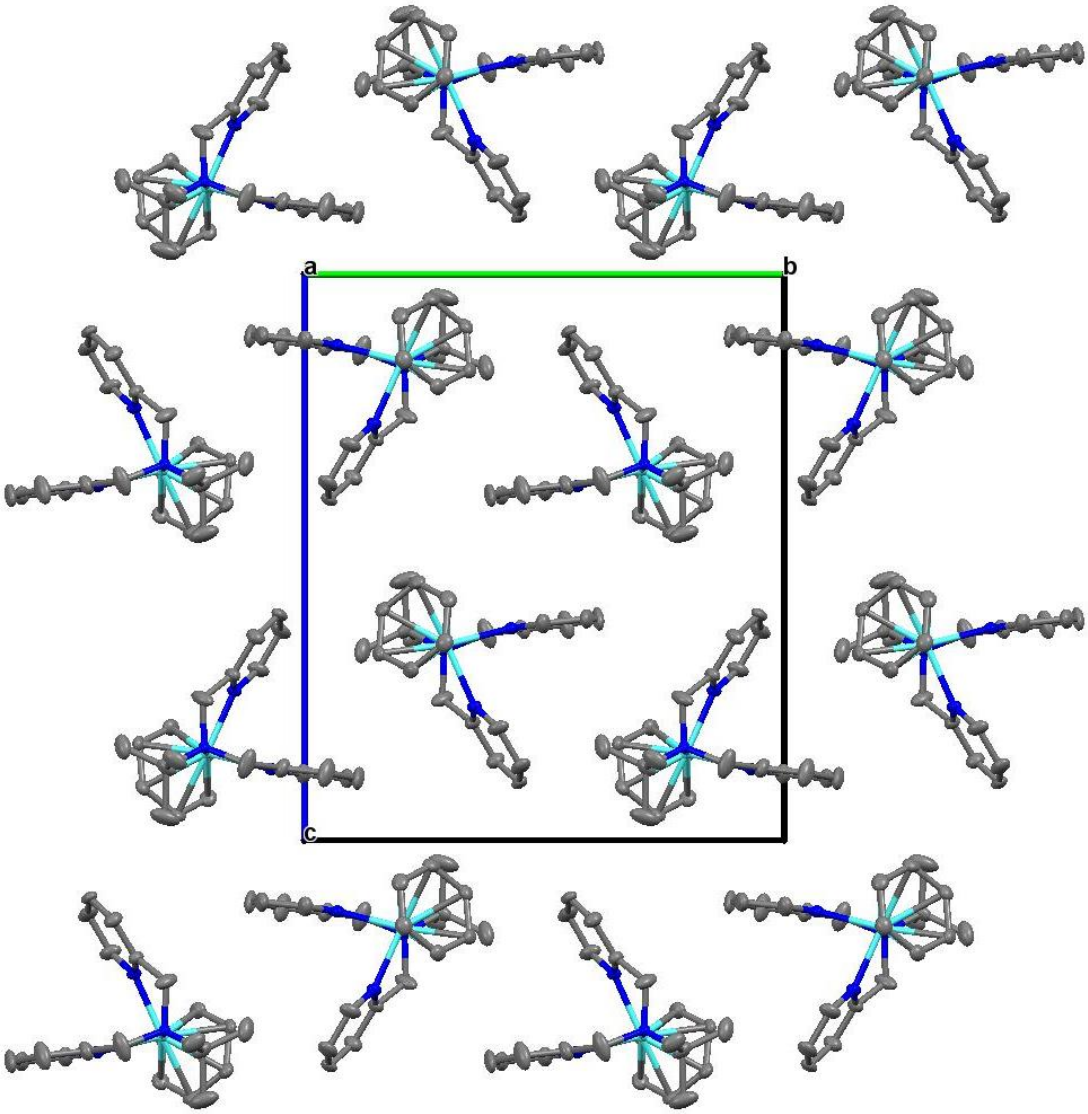

Figure 3.5: The crystal packing diagram of complex **RII** viewed along the crystallographic *a*-axis, with the hydrogen atoms and PF_6^- counterions omitted for clarity.

The crystal structure of **RII** shows non-classical hydrogen bonds where two pyridyl C-**H** atoms on one ring of the **RII** molecule, are linked to two F atoms on two different counterions, through C-H…F intermolecular interactions (C(11)-H(11)…F(6) and C(12)-H(12)…F(6)). A single benzyl C-**H** atom and a methylene C-**H** atom on the same moiety are linked to two F atoms on a third counterion (C(22)-H(22)…F(8) and C(7)-H(7B)…F(12)). The third F atom on the same counterion interacts with a neighbouring pyridyl C-**H** atom, C(5)-H(5)…F(12), thus providing a link between the two molecules (Fig. 3.6).

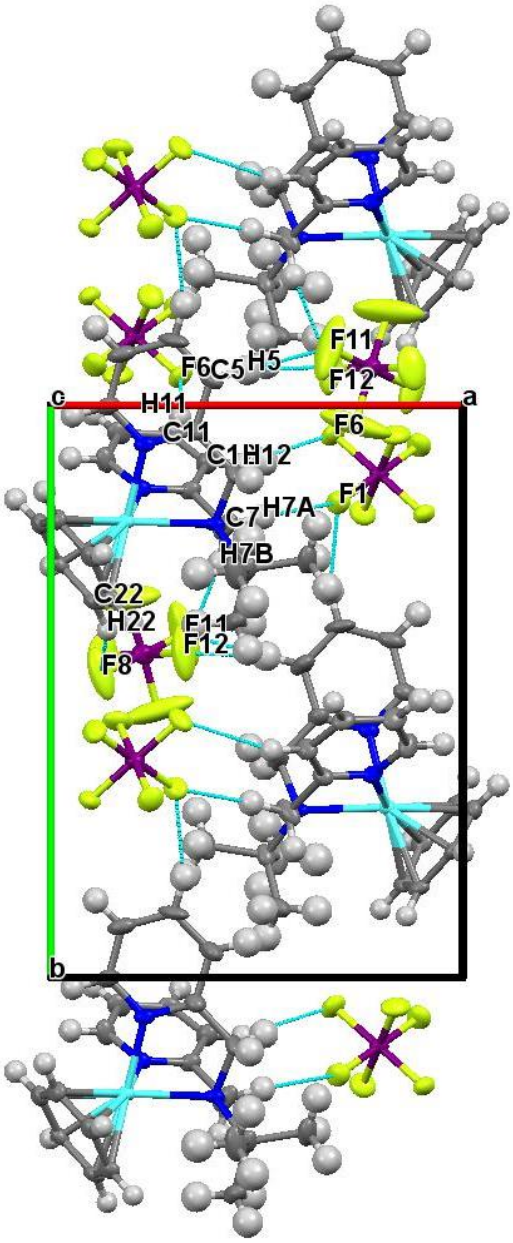

Figure 3.6: The hydrogen bonding patterns (blue lines) present in **RII**, viewed along the crystallographic *c*-axis.

3.2.1.3 Crystal structure RIII

Crystals of compound **RIII** were grown in a concentrated acetonitrile solution through a process of vapour diffusion. Plate-like crystals, golden-yellow in colour, were obtained over a week. The single crystal molecular structure is presented in Fig. 3.7.

As seen from Fig. 3.7, like **RI** and **RII**, complex **RIII** exhibits a piano stool geometry. It has a monoclinic crystal system with the space group P_{21}/c. Comparable to **RI** and **RII**, the hard

N-donor ligand binds to the metal in a terdentate fashion forming a stable pincer complex. The rich electron donating substituents, i.e. the cyclohexyl moiety on the central N-donor atom and the pyridyl rings, all contribute to the stability of the complex. As a result, electron density at the metal centre is amplified. The cyclohexyl fragment, taking on a chair conformation as shown by Fig. 3.7, is also a good source of electrons and for this reason, complex **RIII** also does not dimerise. Both the NMR and crystallographic techniques applied to complex **RIII** complement each other, where the NMR spectrum reveals split methylene peaks due to non-co-planarity in the structure.

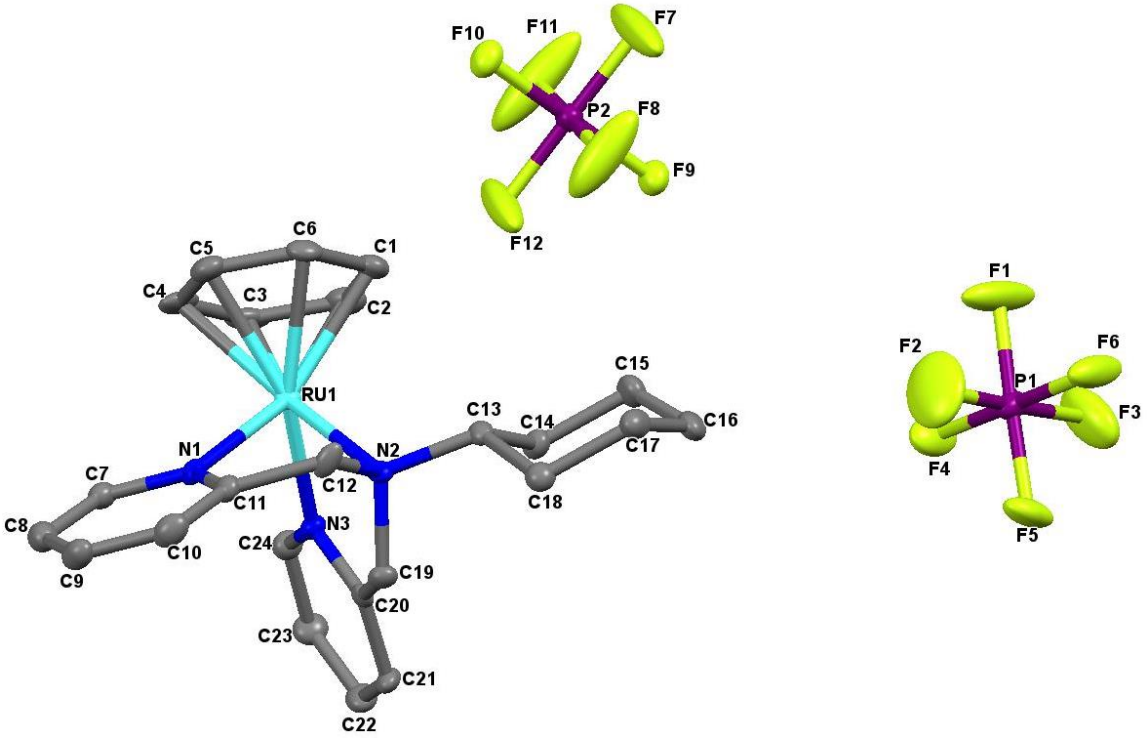

Figure 3.7: Single crystal structure of complex **RIII** drawn at 50% thermal ellipsoid probability, with omission of hydrogen atoms for clarity.

Table 3.5 shows selected bond distances and angles of complex **RIII**. Slight deviation in the geometry is noted between the more strained structure of complex **RIII** and complexes **RI** and **RII**. The Ru-Cg distance of 1.463 Å is comparable to the Ru-Cg distance of 1.462 Å recorded for **RI**, and shows that the benzene ring is bound more tightly to the metal than in the case of **RII** (1.470 Å). **RIII** reveals a more compact geometry around the metal centre, with a less open coordination sphere to potential binding substituents compared to the geometry of the aforementioned complexes **RI** and **RII**. Complex stability is also accounted for through the N(1)-Ru(1) distance of 2.177(4) Å, which is shorter in comparison to the

distance (2.242(3) Å) in complex **RII**. This is in accordance with the theory that the cyclohexyl group is also a strong electron donor, thus strengthening and shortening the N(1)-Ru(1) bond and increasing the electron density at the metal centre.

Table 3.5: Selected bond lengths (Å) and angles (º) for complex **RIII**.

Bond lengths (Å)	
N(1)-Ru(1)	2.090(5)
N(2)-Ru(1)	2.177(4)
N(3)-Ru(1)	2.091(5)
Bond angles (º)	
N(2)-Ru(1)-N(3)	88.66(19)
N(2)-Ru(1)-N(1)	76.22(18)
N(3)-Ru(1)-N(1)	88.66(19)

The bite angles of complex **RIII**, noted by the N(2)-Ru(1)-N(3) and N(2)-Ru(1)-N(1) angles of 88.66(19)º and 76.22(18)º respectively, tend more closely to the tridentate facial coordination angle of 90º. Slight differences are noted to the example of **RII**, which has bite angles of 79.23(12)º and 78.66(12)º for the N(2)-Ru(1)-N(1) and N(3)-Ru(1)-N(1) angles, respectively.

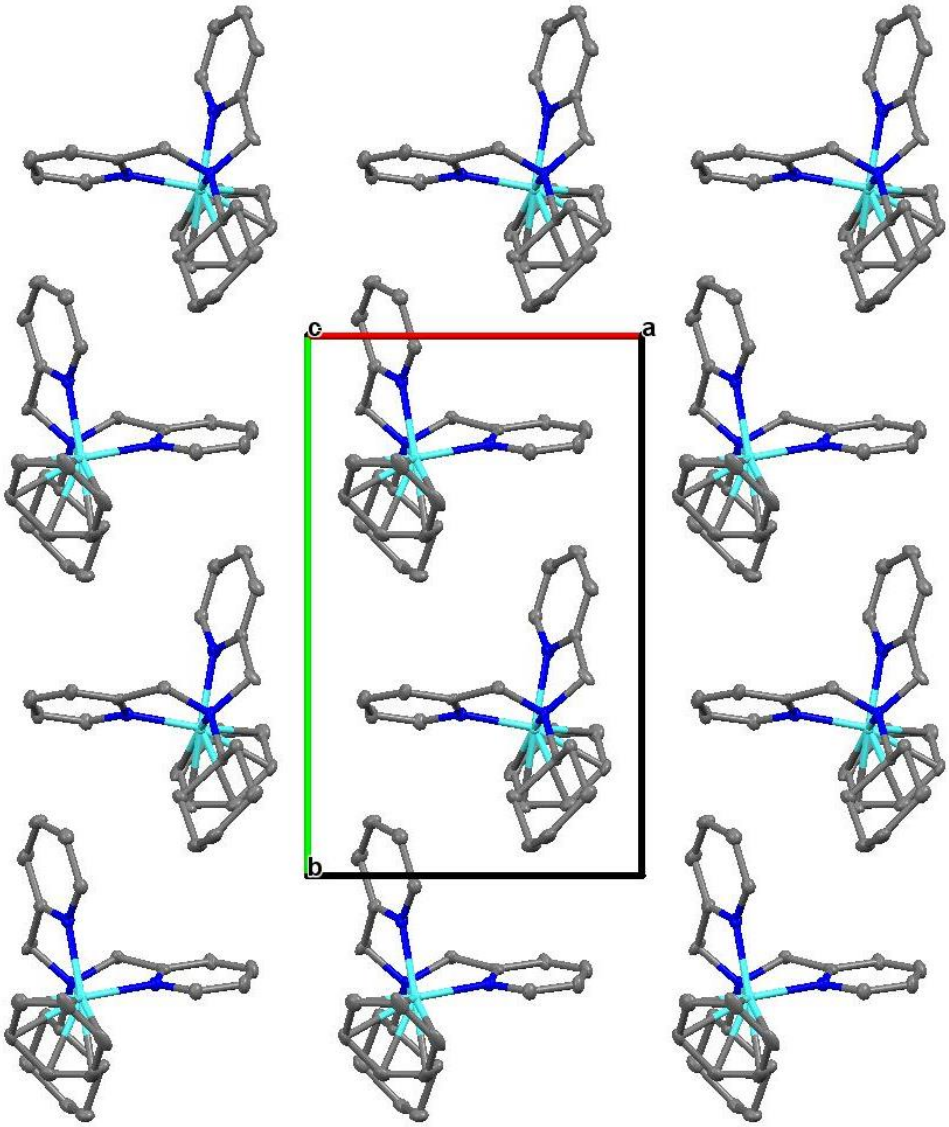

Figure 3.8: The crystal packing diagram of complex **RIII** viewed along the crystallographic *c*-axis, with the hydrogen atoms and PF_6^- counterions omitted for clarity.

The dihedral angle defined by the [N(1), C(7), C(8), C(9), C(10), C(11)] and [N(3), C(20), C(21), C(22), C(23), C(24)] pyridyl rings is seen at an acute angle of 88.31º. This deviates significantly to the dissection angles of complexes **RI** and **RII**, with angles of 63.13º and 63.34º, respectively. This effect is rationalised through twisting of the methylene linker on the side of the [N(3), C(20), C(21), C(22), C(23) and C(24)] pyridyl ring. Noteworthy is the ordered arrangement of the crystal unit occurring in alternating rows in the unit cell as seen in Fig. 3.8.

Non-classical hydrogen bonding is established between two **RIII** molecules in which a cyclohexyl C-**H** atom on one molecule interacts with a fluorine on one counterion (C(13)-H(13)…F(12)), and a second F atom on the same counterion, interacts with a methylene C-**H** atom on the second **RIII** molecule (C(12)-H(12B)…F(9)). C-H…F interactions are also established through a single pyridyl C-**H** atom interacting with a fluorine atom on a second PF_6^- counterion (C(6)-H(6)…F(1)). A fourth interaction exists between a pyridyl C-**H** atom and a fluorine on the third PF_6^- counterion, C(21)-H(21)…F(5), (Fig. 3.9).

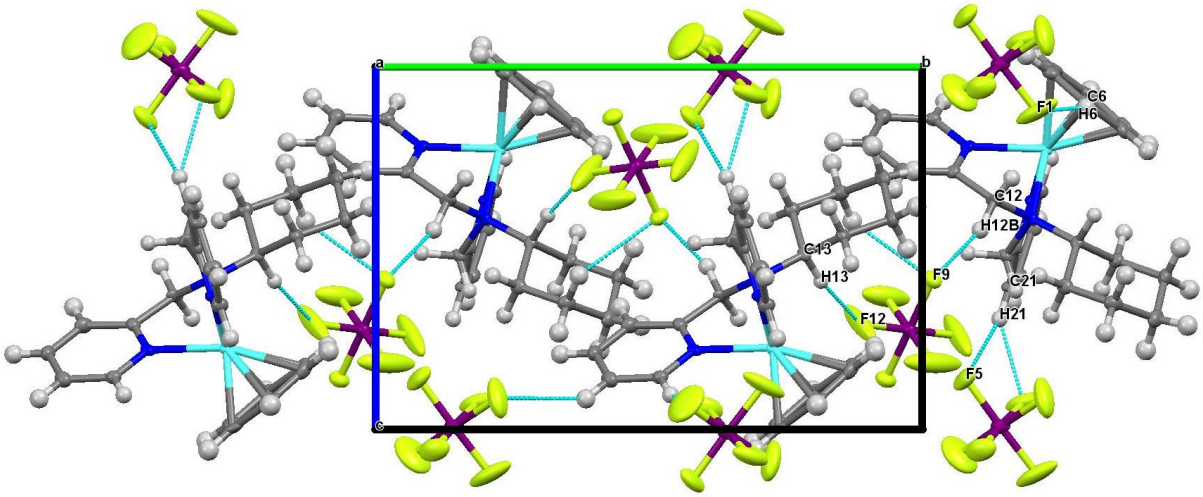

Figure 3.9: The hydrogen bonding patterns (blue lines) present in **RIII**, viewed along the crystallographic *a*-axis.

3.2.1.4 Crystal structure of CV

Deep purple cubic-like single crystals were obtained within a 24 h growth period from a concentrated DCM solution layered with diethyl ether. A representation of complex **CV** is presented in Fig. 3.10.

Complex **CV**, belonging to the triclinic *P*1 space group, crystallises as two independent molecules (A and B, Fig. 3.10) within the asymmetric unit cell. The individual parameters of both the molecular species are essentially similar and therefore a detailed discussion will be given with reference to molecule A only. The overlay diagram shown in Fig. 3.11 confirms that species A and B are similar, with the only difference seen in the twisting of the propyl moieties on the central N-donor atoms on both molecules. Furthermore, the distance between the C14 (molecule A) and C29 (molecule B) atoms is represented as 1.744 Å and further highlights the planes in which these functional groups lie relative to each other.

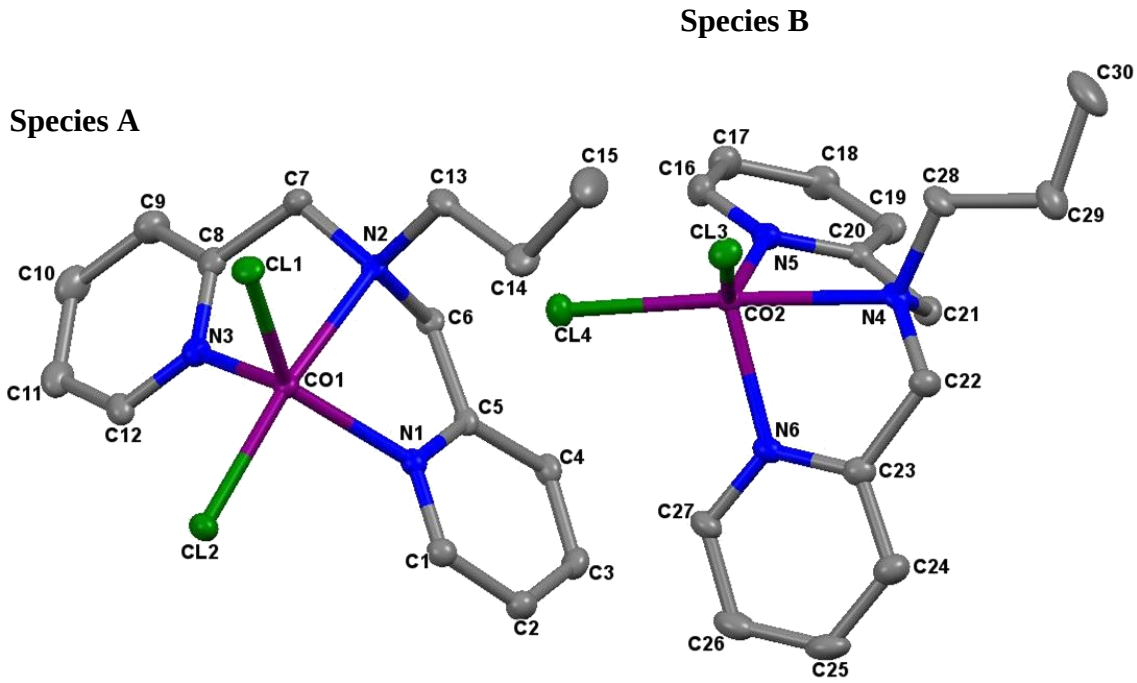

Figure 3.10: Single crystal structure of complex **CV** drawn at 50% thermal ellipsoid probability, with omission of hydrogen atoms for clarity.

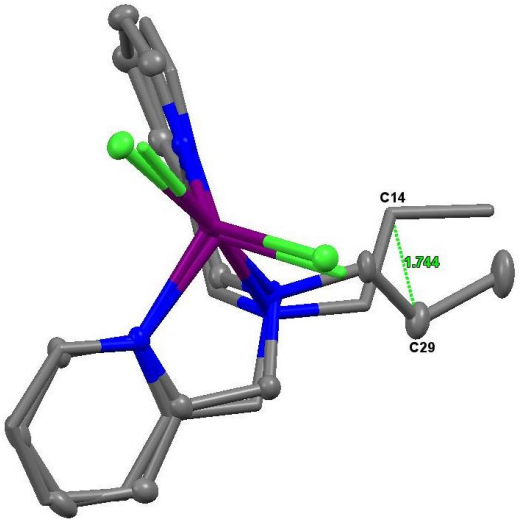

Figure 3.11: An overlay diagram of the single crystal structures of complex **CV** drawn at 50% thermal ellipsoid probability, with omission of hydrogen atoms for clarity.

As seen from Fig. 3.10, the Co complex is stabilised through a terdentate ligand and also coordinated to two terminal chlorine atoms, thus existing as a five coordinate monomer. It is also noted that complex **CV** exists as a highly unsymmetrical molecular specie with each aromatic pyridine ring and the propyl moiety lying in three different planes to each other.

Selected bond lengths and angles for complex **CV** are tabulated in Table 3.6. Noteworthy are the distances of the two pyridyl rings to the metal centre, i.e. the N(1)-Co(1) and the N(3)-Co(1) distances which are 2.086(3) Å and 2.084(3) Å. These are fairly equal to each other and shorter compared to the distance of the central N-donor atom to the metal centre, which is 2.252(3) Å. This implies that the two pyridyl rings are bound more strongly to the metal ion than the central N-donor atom. Due to the greater bond length to the central nitrogen of the backbone, a lower electron density is supplied from the electron rich propyl moiety compared to the case with complex **RI**, having lengthened Ru-C and Ru-N(1) bonds.

Table 3.6: Selected bond lengths (Å) and angles (º) for complex **CV**.

Bond lengths (Å)	
N(1)-Co(1)	2.086(3)
N(2)-Co(1)	2.252(3)
N(3)-Co(1)	2.084(3)
Cl(1)-Co(1)	2.3154(11)
Cl(2)-Co(1)	2.3240(11)
Bond angles (º)	
N(1)-Co(1)-N(2)	76.77(12)
N(2)-Co(1)-N(3)	77.00(13)
N(1)-Co(1)-N(3)	109.95(13)
N(1)-Co(1)-Cl(1)	136.34(10)
N(2)-Co(1)-Cl(1)	89.35(9)
N(3)-Co(1)-Cl(2)	99.60(10)
N(1)-Co(1)-Cl(2)	95.22(10)
N(2)-Co(1)-Cl(2)	169.33(9)
N(3)-Co(1)-Cl(2)	106.69(10)
Cl(1)-Co(1)-Cl(2)	101.33(4)

Due to the more obtuse N(1)-Co(1)-N(3) bite angle of 109.95(13)º, complex **CV** exhibits a distorted trigonal bipyramidal geometry with a more open coordination sphere. Due to the larger N(2)-Co(1)-Cl(2) bond angle of 169.33(9)º, the central N-donor atom, together with the chlorine atom, lie in the axial position, while the equatorial positions are occupied by the

N-donor atoms of the pyridyl rings. This opposes the more traditional scenario observed for Co SNS complexes with a similar geometry reported by Soobramoney *et al*., where the axial positions are occupied by the S-donor atoms, having a more obtuse bite angle.[11] This supports the theory that the hard nitrogen atoms of complex **CV** supply an increased flow of electron density to the metal, thus strengthening the bonds between the N-donor atoms and the metal centre. This is evident through the shorter bond distances, compared to the more loosely bound hemilabile nature of the S-coordinating atoms, which have a larger bite angle and a less compact geometry.

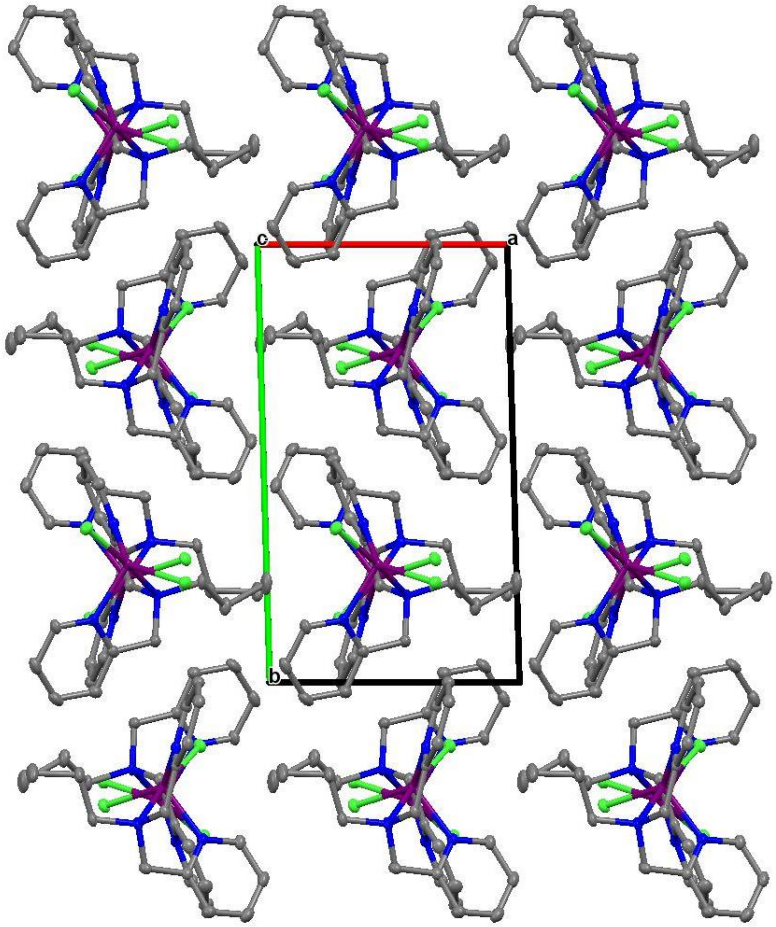

Figure 3.12: The crystal packing diagram of complex **CV** viewed along the crystallographic *c*-axis, with the hydrogen atoms omitted for clarity.

Due to twisting of the methylene linker between the central N-donor atom and the pyridine rings, the planes of the pyridyl rings, i.e. the [N(1), C(1), C(2), C(3), C(4), C(5)] and [N(3), C(8), C(9), C(10), C(11), C(12)] planes, have an acute angle of 75.23°, making the binding ligand a non-symmetrical one. However, apart from this distortion, the crystal packing in

alternating rows within the crystal unit shows signs that the complex is ordered (Fig. 3.12). The crystal structure of **CV** shows non-classical C-H…Cl intramolecular interactions, where one Cl atom on a single **CV** molecule is linked to a single pyridyl C-**H** atom on a neighbouring molecule, C(2)-H(2)…Cl(3), whilst the second Cl is linked to another pyridyl C-**H** atom and a methylene C-**H** atom on two different molecules, C(4)-H(4)…Cl(4) and C(7)-H(7B)…Cl(4), respectively (Fig. 3.13).

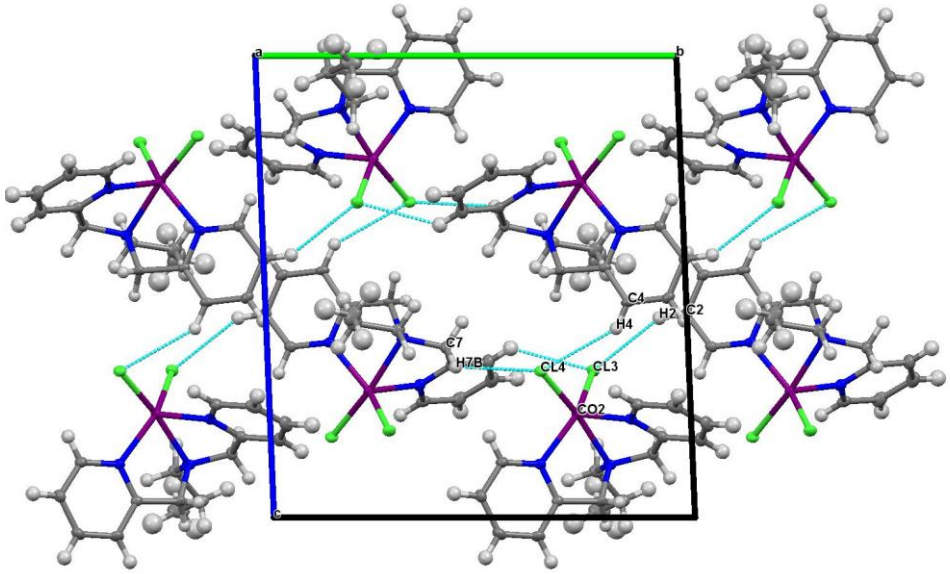

Figure 3.13: The hydrogen bonding patterns (blue lines) present in **CV**, viewed along the crystallographic *a*-axis.

3.3 Summary

Crystal structures of complexes **RI**, **RII**, **RIII** and **CV** were successfully obtained through methods of vapour diffusion and layering. Furthermore, it was shown from the crystal structures that all Ru complexes exhibited a piano stool geometry whilst **CV** took on a trigonal bypyramidal geometry. From the metric parameters, the pyridine rings were seen to be bound most tightly to the metal centre. Each crystal showed signs of order by their arrangement in alternating rows shown in each packing diagram. Non-classical intermolecular C-H…F and intramolecular C-H…Cl hydrogen bonding were observed in the Ru and Co packing, respectively. Ligands were seen to bind in a terdentate fashion to the metal centre in complexes **RI**, **RII**, **RIII** and **CV**, as intended.

3.4 References

1. Bruker (2012) *SAINT* and *XPREP*, Bruker AXS Inc., Madison, Wisconsin, USA.
2. G. M. Sheldrick, *SHELXS*-2008, *SHELXL*-2014 and *SADABS* version 2.05, University of Göttingen, Germany, 1997.
3. L. J. Barbour, *Journal of Supramolecular Chemistry*, 2001, **1**, 189-191.
4. J. L. Atwood and L. J. Barbour, *Crystal Growth and Design*, 2003, **3**, 3.
5. *POVRAY*. Persistence of Vision Raytracer 3.6.
6. Bruker (2012) APEX2 (Version 2012.10-0), Bruker AXS Inc., Madison, Wisconsin, USA.
7. Bruker (2012) SADABS (version 2012/1), Bruker AXS Inc, Madison, Wisconsin, USA.
8. G. M, Sheldrick, (2008). Acta Crystallographica Section A64, 112-122.
9. A. L. Spek, *Journal of Applied Crystallography*, 2003, ***36***, 7-13.
10. C. F. Macrae, I. J. Bruno, J. A. Chisholm, P. R. Edgington, P. McCabe, E. Pidcock, L. Rodriguez-Monge, R. Taylor, J. van de Streek and P. A. Wood, *Journal of Applied Crystallography*, 2008, **41**, 466-470.
11. L. Soobramoney, M. D. Bala and H. B. Friedrich, *Dalton Transactions*, 2014, **43**, 15968-15978.
12. H. Mishra, A. K. Patra and R. Mukherjee, *Inorganica Chimica Acta*, 2009, **362**, 483-490.
13. J. M. Gichumbi, H. B. Friedrich and B. Omondi, *Journal of Molecular Catalysis A: Chemical*, 2016, **416**, 29-38.
14. Z. Shirin, R. Mukherjee, J. F. Richardson and R. M. Buchanan, *Journal of the Chemical Society, Dalton Transactions*, 1994, 465-469.

Chapter Four

Oxidation studies of *n*-octane

4.1 Introduction

This chapter describes the investigation carried out on the functionalisation of a saturated, medium chain hydrocarbon, *n*-octane, using Ru and Co NNN-pyridine based catalysts. Various examples outlining the C-H bond activation of several substrates, using enzymatic models and chemical systems, have been reported in Chapter one, Sections 1.1 and 1.2. To date, there have been limited published reports detailing oxidation studies on Co and Ru NNN pincer complexes. Therefore, the novelty of this work is further accentuated by the application of new Ru and Co NNN-pyridine based pincer complexes.

There have been few reports highlighting the application of Co tridentate systems in paraffinic oxidation. The formed ROO• and RO• radicals from Co^{3+} alkyl peroxo complexes applied in hydrocarbon activation have been deemed as the active species involved in oxidising the hydrocarbon substrate.[1] Furthermore, the oxidation of *n*-octane has been achieved using pincer type SNS complexes which served as efficient catalysts in oxidising the alkane using *t*-BuOOH as a mild source of oxygen over that of H_2O_2.[2]

Reports on C-H activation of alkanes using pincer Ru complexes are scarce. One such report highlighted polymer-supported Ru catalysts using *t*-BuOOH in the oxidation of cyclohexane, that efficiently gave cyclohexanol and cyclohexanone as products. The mechanistic pathway was established though a radical scavenging reaction using 2,6-di-*tert*-butyl-4-methyl phenol (BHT), in which a marginal reduction in yield was observed and thus the oxidation reaction proceeding *via* a free radical pathway was suppressed. Due to the robustness and easily available Ru=O species, ruthenium complexes with 2,2'-bipyridines or 1,10-phenanthrolines have been attractive and efficient systems in the catalytic oxidation of cyclohexane to the corresponding alcohols and ketones.[3] Furthermore, oxidation of linear alkanes catalysed by homogeneous Ru complexes have been scarcely reported in the literature.

The production of oxygenates, occurring *via* the reaction between the saturated hydrocarbon substrate and a peroxo species, is a process that very commonly occurs through a radical mechanism, apart from others which have been discussed in Chapter 1, Section 1.2. A wide

range of oxidising agents including iodosylbenzene (PhIO), alkyl hydroperoxides, sodium hypochlorite (NaOCl), hydrogen peroxide, percarboxylic acids and molecular oxygen have all been noted in the literature.[3] Furthermore, many of the biological systems reported in Section 1.1 have been effective in C-H bond functionalisation and product formation was also believed to proceed *via* radical pathways.

The oxidation of hydrocarbons using hydrogen peroxide proceeds *via* the steps described below (equations **1**-**4**):

1. The generation of oxy radicals, HO•, occurs through decomposition of the peroxide species that is catalysed by the metal (eq **1**).
2. The abstraction of the hydrogen atom from the alkane substrate by the oxy radical HO•, creates an alkyl radical, R• (eq **2**).
3. A reaction between the alkyl radical R• and O_2 produces the peroxo radical ROO• (eq **3**).
4. As seen from eq **4**, the peroxo radicals react with the hydrocarbon substrate to produce the alkyl hydroperoxide. The production of alcohol and ketone oxygenates occurs through decomposition of the alkyl hydroperoxide occurring as the reaction proceeds.

Essentially, the ketone, as well as aldehyde and carboxylic acid oxygenates, form through a process known as deep oxidation. This is a common process occurring through further oxidation of alcohols to produce e.g. ketones or *via* over-oxidation of the terminal hydrocarbon, aldehydes and subsequently, carboxylic acids.

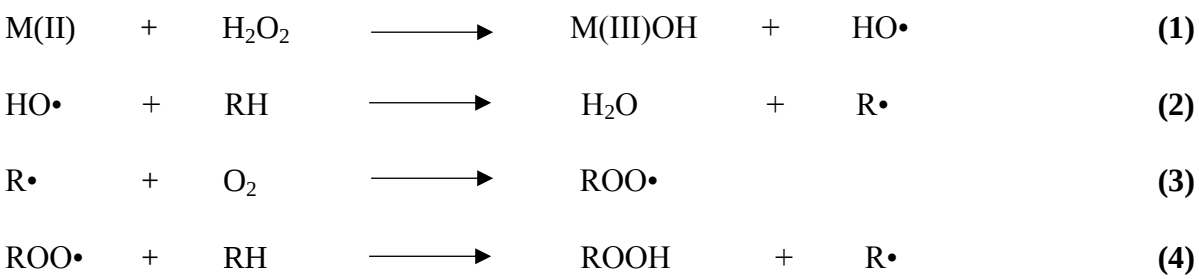

Scheme 4.1: Radical steps in the oxidation of hydrocarbons represented by equations **1**-**4**.

When *tert*-butylhydroperoxide is used as an oxidant, *tert*-butyl peroxo (*t*-BuOO•) and *tert*butoxyl radicals (*t*-BuO•) are formed in the initiation step instead of HO• radicals. Reports have shown that the *t*-BuOO• possesses insufficient radical strength to abstract a proton from

the hydrocarbon substrate and hence decomposes to yield the *t*-BuO• radical that is sufficiently active to abstract the hydrocarbon H atom.[4]

There are two other types of hydrocarbon oxidation. The first can be described through the production of organometallic intermediates or final products that are produced *via* "True" organometallic C-H bond activation. The other type is classed through the role of the metal complex in abstracting a hydrogen or electron from the hydrocarbon substrate. The C-H bond can be cleaved *via* a ligand and contact can be maintained between the metal complex and C-H bond.

Some of the common problems associated with efforts to functionalise C-H bonds are seen through the production of terminal oxygenates. The activation of the terminal hydrocarbon is usually rare and is associated to the strength of the terminal C-H bond, which is the most difficult to cleave since it is the strongest hydrocarbon bond in a linear chain.[5] For this reason, together with the overall inert nature of the C-H bonds in the saturated hydrocarbon chain, low conversions are generally expected.[6]

Another problem faced is the preferential oxidation of one carbon atom over another.[7] The regioselectivity (preferential functionalisation of a particular carbon position over another in a hydrocarbon chain) and stereoselectivity (formation of a particular stereoisomer over another) parameters can be enhanced through modification of the metal catalyst by incorporating bulky ligands into the framework, hence subsequently enhancing its reactivity.[7, 8]

In this study, the prepared Ru and Co catalysts, **RI-CVIII**, were applied in the C-H bond activation of *n*-octane using two sources of peroxide, *t*-BuOOH and H_2O_2. Acetonitrile was the selected solvent medium in which all catalysts were miscible, with varying reaction temperatures ranging from room temperature to 80 °C. Optimisation studies using both metal catalysts were made based on the conversion of *n*-octane and the product distribution profiles of each system.

4.2 Experimental methods

4.2.1 Materials and instrumentation

All catalytic reactions were carried out under inert nitrogen atmosphere in a sealed system using moisture free glassware to circumvent air oxidation. The solvent (acetonitrile) was saturated with nitrogen for 10-15 min prior to use. The internal standard used in calibrating the GC comprised of 1-octanol (99%), 2-octanol (97%), 3-octanol (98%), 4-octanone (99%), octanal (99%) and octanoic acid (99%), which were obtained from Sigma-Aldrich; 2-octanone (97%), 3-octanone (97%), 4-octanol (98%) which were sourced from Fluka and *n*-octane (99%) which was obtained from Merck. The internal standard, cyclopentanone (99%), and solvent, acetonitrile (99%), were obtained from Sigma-Aldrich and Merck, respectively. The oxidants, *tert*-butylhydroperoxide (70%) and hydrogen peroxide (30%) were sourced from Sigma-Aldrich and DLD Scientific, respectively.

All products were analysed using a Claurus 580 Auto System Gas chromatograph integrated with a Flame Ionisation Detector (FID). Column specifications and GC parameters are listed in Table 4.1. The duration of each run excluding the oven cooling period was 49 min.

Table 4.1: Column specifications and GC parameters used in quantifying the oxygenated products.

Column	**Pona 50 m x 0.2 mm x 0.5 µm**				
Injector temperature	240 °C				
Detector temperature	300 °C				
Split	On flow rate: 8.16 mL min^{-1}				
Attenuation	8				
Range	1				
	Column programme				
Initial temperature/ °C	**Ramp one/ °C/ min**	**Temperature two/ °C**	**Ramp two/ °C/ min**	**Temperature three/ °C**	**Ramp three/ °C/ min**
40	15	80	5	100	240

4.2.2 General procedure

Oxidation studies were carried out under inert atmosphere in a sealed system comprising of a 50 mL pear shaped flask equipped with a condenser. The substrate, *n*-octane, was added relative to the amount of catalyst added and the mass of cyclopentanone was kept constant at < 20 mg. The reaction mixture comprised of the catalyst (~3 mg for all Co complexes, ~6 mg for all pincer Ru complexes, **RI**-**RII**, and ~3 mg for the bidentate **RIV** catalyst) in 10 mL of acetonitrile with subsequent addition of the hydrocarbon substrate and internal standard. The peroxides (*t*-BuOOH or H_2O_2) were added at differing ratios relative to amount of substrate added. The mixture was stirred in an oil bath at varying temperatures in order to establish the optimum reaction conditions, after which an aliquot of the mixture was removed with a Pasteur pipette and filtered through silica. Of this mixture, 0.5 μL was injected into the GC for quantification of the products.

The reaction masses and volumes of reaction mixtures (including those in the absence of catalysts) at the varying temperatures are shown in Appendix A4 (Tables A4.2-A4.6), whereby the quantity of catalyst added was kept constant at 1 mol%. This implies that the ratio of catalyst to substrate was 1:100. The optimum conditions were established through testing various mole ratios of substrate to oxidant in which the oxidant was added in excess. All data reported are within acceptable limits of error, since reproducibility checks were conducted and the average of two values within 1% difference are reported.

Studies investigating the mechanism of each catalytic system were done using 2,2,6,6-tetramethylpiperidine-1-oxyl (TEMPO) as a radical scavenger. A five equivalent ratio of the scavenger relative to the substrate was added with addition of *t*-BuOOH as the sole oxidant at the optimum reaction conditions.

Furthermore, a study with 2-octanol as a substrate was conducted in order to ascertain the rate of over-oxidation occurring in a particular reaction. This study, which included blank reactions, was performed in a similar manner as that of *n*-octane, in which the ratio of catalyst (Co) to substrate to oxidant was 1:100:105, whilst the ratio for the Ru catalyst was 1:100:116 and the reactions were monitored over a period of 9 hours in both cases (Appendix A4, Table A4.9).

The oxidation of *n*-octane was also carried out using H_2O_2 under the optimum conditions established with *t*-BuOOH catalysed by the Co and Ru complexes.

4.3 Results and discussion

4.3.1 The oxidation of *n*-octane using *t*-BuOOH as the oxidant

The catalytic oxidation of *n*-octane by an environmentally attractive oxidant, *t*-BuOOH, was chosen as one approach to sustainable chemistry.[9] The idea behind this choice of oxidant was further promoted by its use as a milder oxidant than H_2O_2, which thus may prevent decomposition of catalysts containing soft ligand systems in their framework.[7] Furthermore, this type of oxidant has been widely explored due to its ease of handling, whilst being cost effective at the same time.[10] Acetonitrile was the choice of solvent because all catalysts were soluble in it and its high polarity[8] allows miscibility with water that makes up 30% and 70% of the total volume of the added *t*-BuOOH and H_2O_2 solutions, respectively.

To determine if *t*-BuOOH is active in the absence of the catalyst or if any thermally initiated oxidation is possible, blank reactions were carried out at the optimum temperature of 80 °C at varying substrate to oxidant mol ratios of 1:3, 1:6, 1:9, 1:12 and 1:15. From Fig. 4.1, a total conversion of 2% and 3% was achieved with ratios of 1:3 and 1:6 respectively, and a relatively constant conversion of 5% was seen with mol ratios of 1:9, 1:12 and 1:15 thereafter (Fig. 4.1). These conversions compared to previous reports which show relatively low conversions of 1% at varying substrate to oxidant content, and may be attributed to a thermodynamic effect[11], as seen in Fig. 4.1. This effect was further confirmed by conducting control experiments in the dark, since UV radiation can be a radical initiator (a process known as photo-oxidation), however, similar conversions at the varying substrate to oxidant ratios were observed. Furthermore, when conducting blank reactions at 50 °C, conversions of 1-4% were observed at ratios of 1:3-1:15 (Fig. 4.1). These results support thermally induced oxidation of the substrate.

Two other blank studies were conducted where no conversion was observed for both cases. The first blank reaction contained the catalyst in the absence of oxidant, whilst the second blank was conducted to test the stability of the internal standard, where the substrate was omitted from the reaction mixture.

4.3.1.1 Optimisation studies: time, temperature and *n*-octane to *t*-BuOOH ratio for the Co systems

A time dependent study on the reaction was carried out, in which the reaction mixture was refluxed at 80 °C for periods of 24 hours and 48 hours at the varying substrate to oxidant ratios. Complex **CV** was used as a representative catalyst for this study. From the results in Figs. 4.2 and 4.3, a 24 hour time period was chosen as the optimum time for the oxidation of *n*-octane, since it gave the same conversion as seen over 48 hours. The highlight of the study was associated with the high content of alcohols produced in comparison to the formation of ketones. As time progressed, over-oxidation was evident after 48 hours, with a significantly larger production of ketones and a noticeable decrease in the production of alcohols (Fig. 4.4). Moreover, a similar study conducted using flexible SNS systems in the oxidation of *n*-octane produced ketones as the major product in 24 hours[2], and this has also been a common trend observed in literature.[11-14]

The formation of primarily alcohols may be attributed to the sterics of the ligand, where the rigid systems containing stable pyridine rings are less accommodating to the binding substrate due to a more compact coordination sphere. This makes the catalyst more selective, rather than active, and can be viewed as a system which slows down the rate of over-oxidation.

Investigating the effect of temperature on the system, a study using **CV** as a model catalyst was carried out at 50 °C. From these results (Figs. 4.5 and 4.6), a high selectivity to alcohols was found over 24 hours, however, the conversions observed were significantly lower.

Reactions with similar *n*-octane to *t*-BuOOH ratios (1:3, 1:6, 1:9, 1:12 and 1:15) used in the blank studies were carried out with **CV** as the representative catalyst to establish the optimum peroxide content. It can be noted from Fig. 4.1 that, initially, as the amount of oxidant in the reaction mixture increases, so did the overall conversion. However, at higher *n*-octane to *t*-BuOOH ratios of 1:20, a drop in conversion from 9% to 8% was observed and this was attributed to the attack on the catalyst by the high content of peroxide in the system (Appendix A4, Fig. A4.1). Also, from these findings, the catalyst was seen to withstand a high concentration of oxidant (1:15) and this may be due the complex having pyridine rings in the structure which are stable towards oxidative attack. The data presented shows that from both the selectivity profiles and substrate conversion, the optimum reaction conditions for the

Co catalysts appear to be a 1:15 substrate to oxidant ratio, at 80 °C within 24 hours. These conditions were chosen to test the remaining catalysts. The active role of the catalyst is further exemplified in the product distribution profiles between the catalyst **CV** and the blank reaction at 80 °C with a 1:15 substrate to oxidant ratio, that implies that a parallel mechanism may be occurring. Thus the catalyst produces alcohols that are then further oxidised, relatively slowly, to produce ketones. In the absence of interaction with the catalyst, the rate of over-oxidation caused by the peroxide, is uncontrolled and occurs rapidly to produce a higher content of ketones than alcohols (Appendix A4, Fig. A4.2).

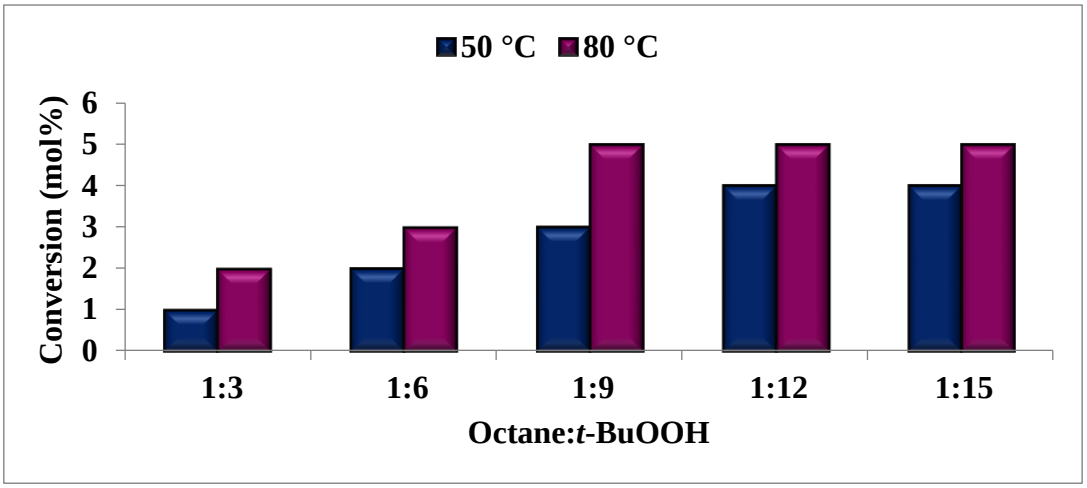

Figure 4.1: The total conversion of *n*-octane at varying substrate to oxidant ratios for the blank reactions over 24 h at 50 °C and 80 °C.

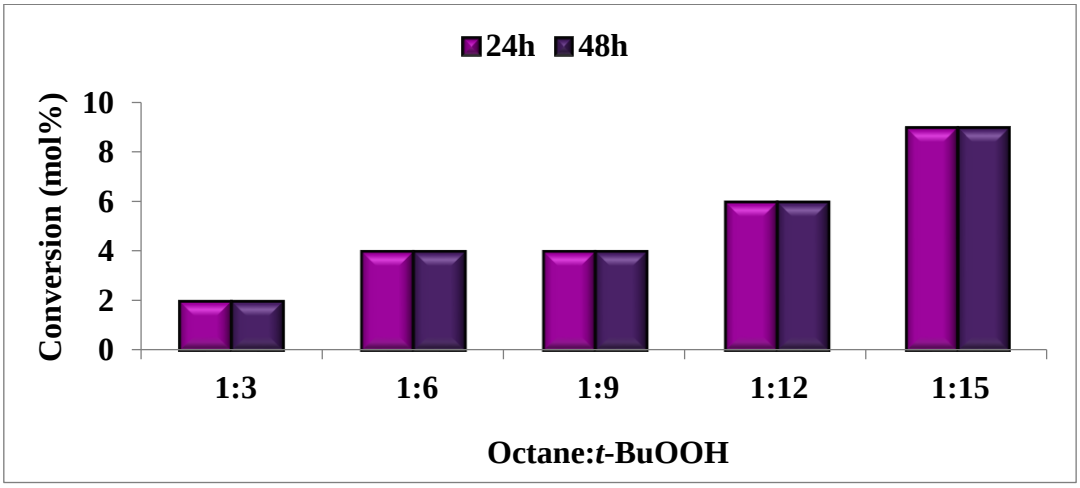

Figure 4.2: The total conversion of *n*-octane at 80 °C within 24 h and 48 h over **CV**.

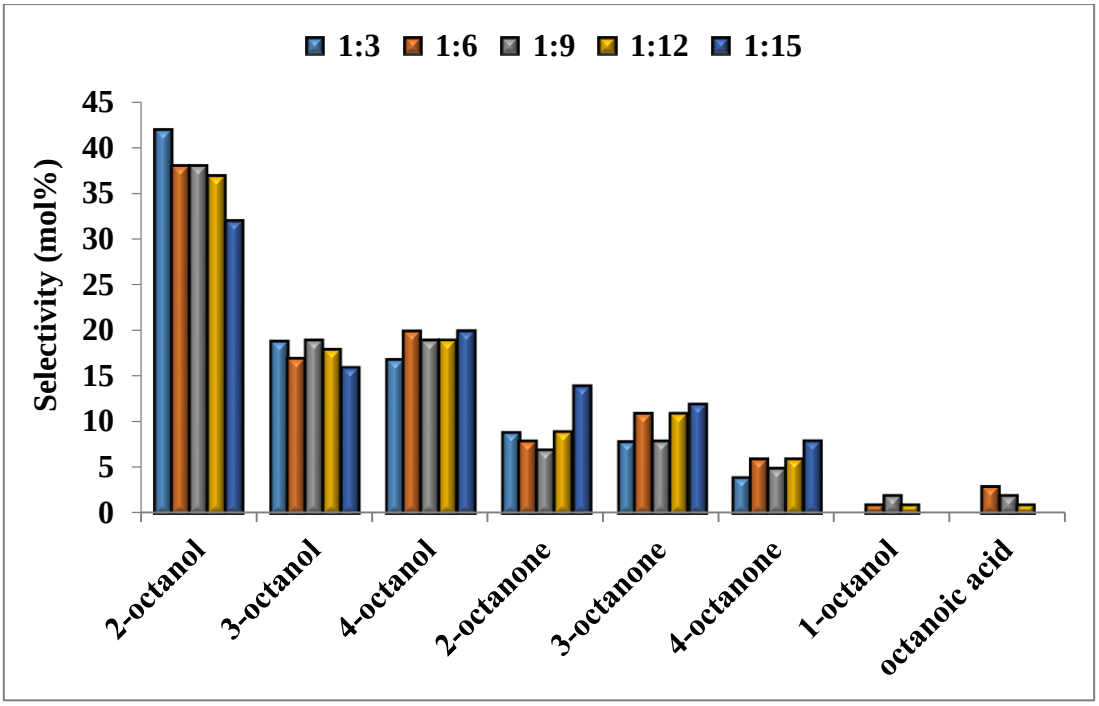

Figure 4.3: The selectivity profiles showing products formed over 24 h at 80 °C for **CV**.

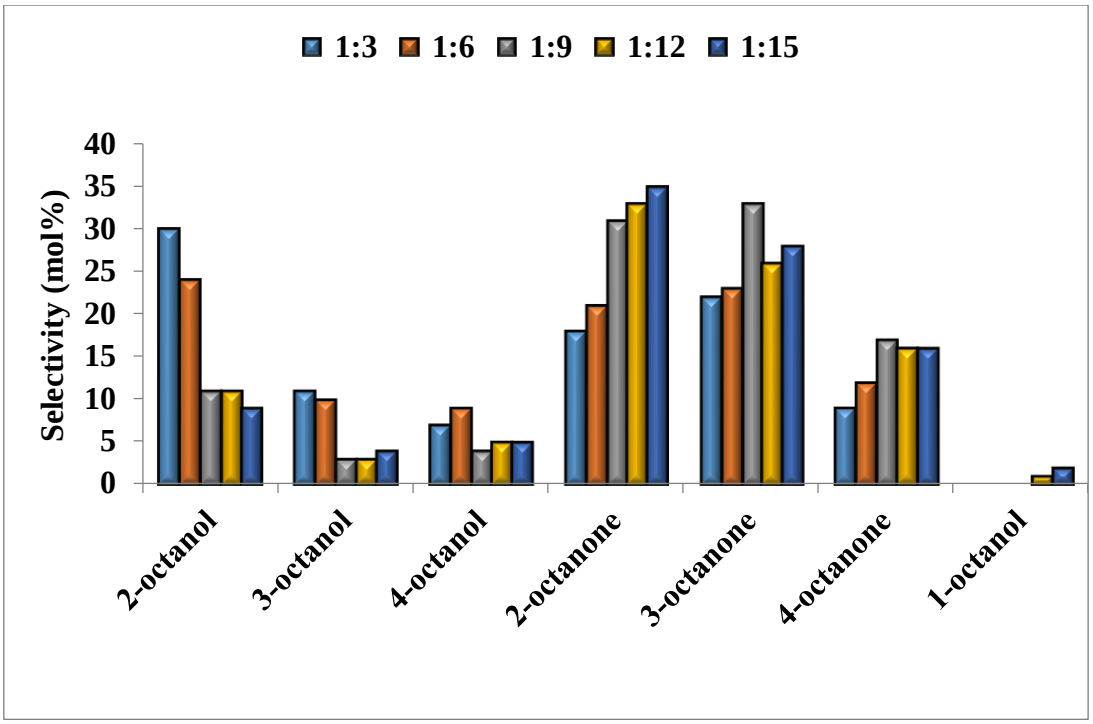

Figure 4.4: The selectivity profiles showing products formed over 48 h at 80 °C for **CV**.

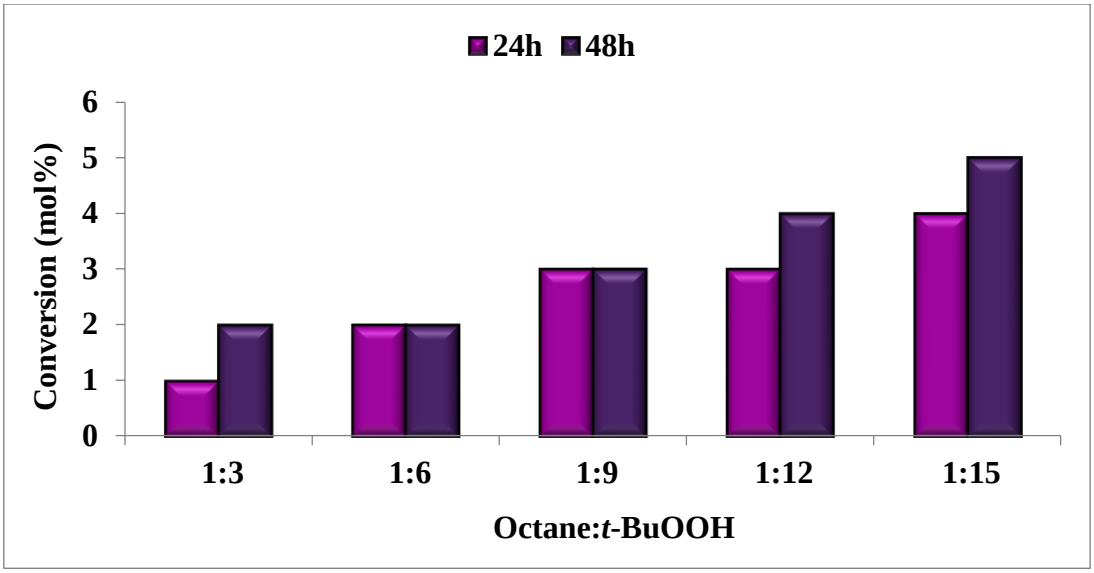

Figure 4.5: The total conversion of *n*-octane at 50 °C over 24 h and 48 h for **CV**.

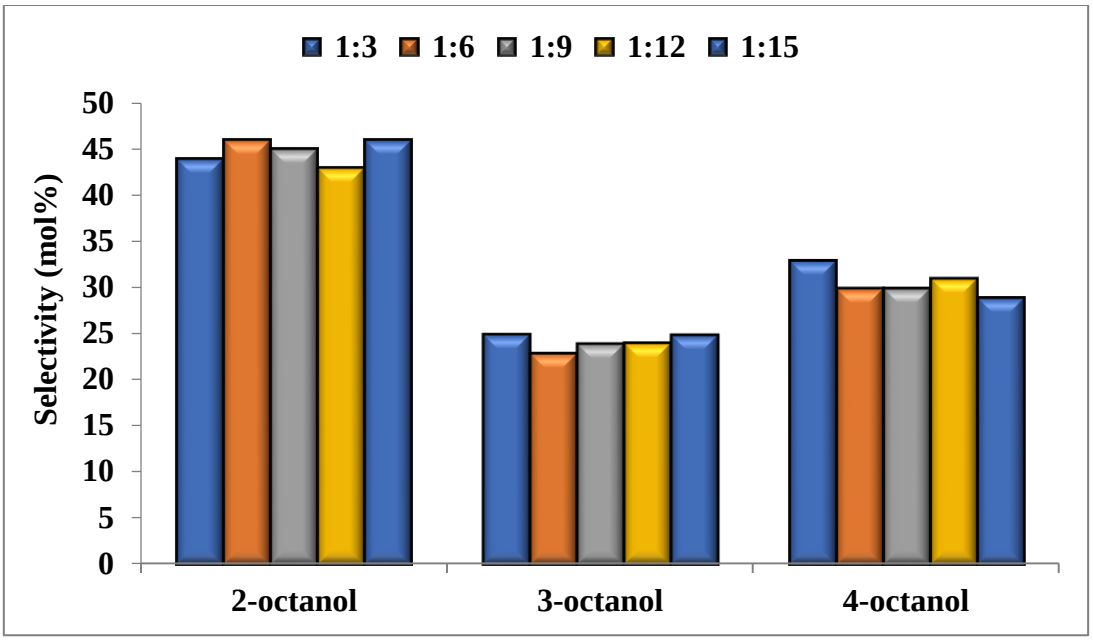

Figure 4.6 The product distribution profiles for **CV** over 24 h at 50 °C.

4.3.1.2 Catalytic testing of Co complexes CV-CVIII at the optimum conditions

The production of isomeric C8 oxygenates (alcohols and ketones) through oxidation of *n*-octane by *t*-BuOOH at carbon positions: C(1), C(2), C(3) and C(4) was catalysed by **CV-CVIII**. The data is presented in Figs. 4.7 and 4.8 which show the total conversion obtained

over each catalyst, as well as the product distribution profiles over 24 hours, respectively. It is important to note that octane loss can occur although all reactions were carried out in a sealed system. This was compensated for by calculating the total conversion based on the total moles of product formed over the initial moles of *n*-octane, whilst the selectivity is reported as the total moles of a particular product formed over the total moles of all products produced. Both calculations were expressed as percentages. The individual selectivity profiles of the cobalt catalysts are presented in Appendix A4, Fig. A4.3.

The information depicted in Fig 4.7 concisely illustrates that catalyst **CVI** was most active with a total conversion of 10%. This confirms theoretical expectations for the conversion over **CVI**, since the *tert*-butyl group on the central N-donor atom is expected to enhance the activity of the catalyst. The activity is thus influenced by a steric and an electronic factor, since the *tert*-butyl group is more electron donating and bulky. Reports have shown that an increase in steric interactions promotes ligand dissociation from the metal centre and thus enhances the reactivity of the metal.[15] However, from the metric parameters presented in Chapter three (metal-ligand bond strengths), ligand dissociation is unlikely to occur due to tightly bound pyridyl rings to the metal centre. With regards to **CV**, the propyl substituent on the central N-donor atom is less electron donating than the *tert*-butyl group on **CVI** and therefore accounts for a recorded conversion of 8%. The least active catalyst, with a total conversion of 7%, was complex **CVIII** and may be rationalised through the steric influences of the catalyst on the conversion of *n*-octane.

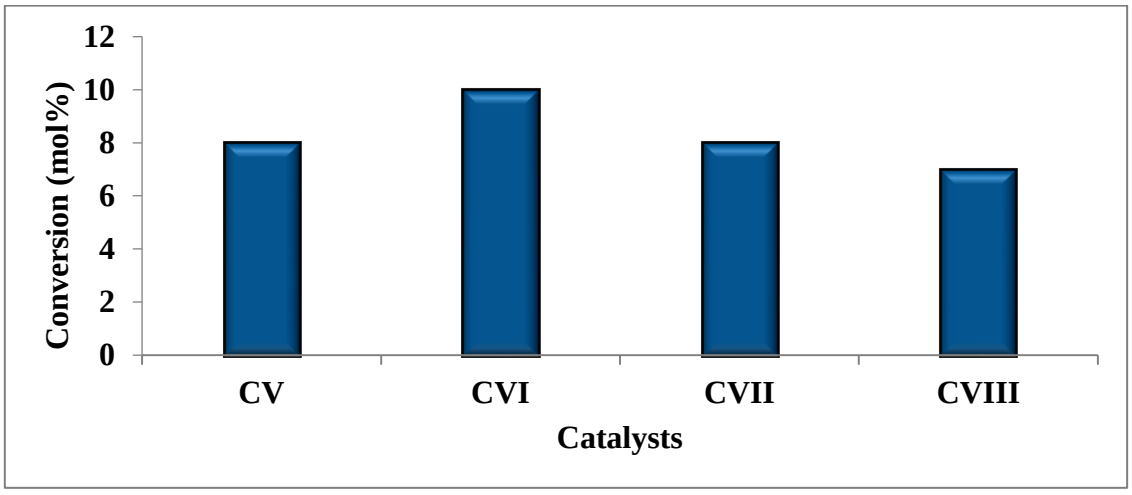

Figure 4.7: The total conversion of *n*-octane under the optimum conditions after 24 h for catalysts **CV-CVIII**.

The lower conversions of catalysts **CVII** and **CVIII** (8% and 7%, respectively) relative to **CVI**, are expected since the cyclohexyl and phenyl moieties (**CVII** and **CVIII**, respectively) are more sterically hindered than the *tert*-butyl group. Also, the introduction of these substituents together with the rigid pyridyl rings of the ligand, introduce overall stability to the catalysts. This reduces easy access to the metal centre and restricts binding of the substrate, which may reduce the catalytic activity of the system compared to **CVI**. In summary, an electronic effect is evident up to a point (catalyst **CVI**), with steric effects dominating thereafter (catalysts **CVII** and **CVIII**).

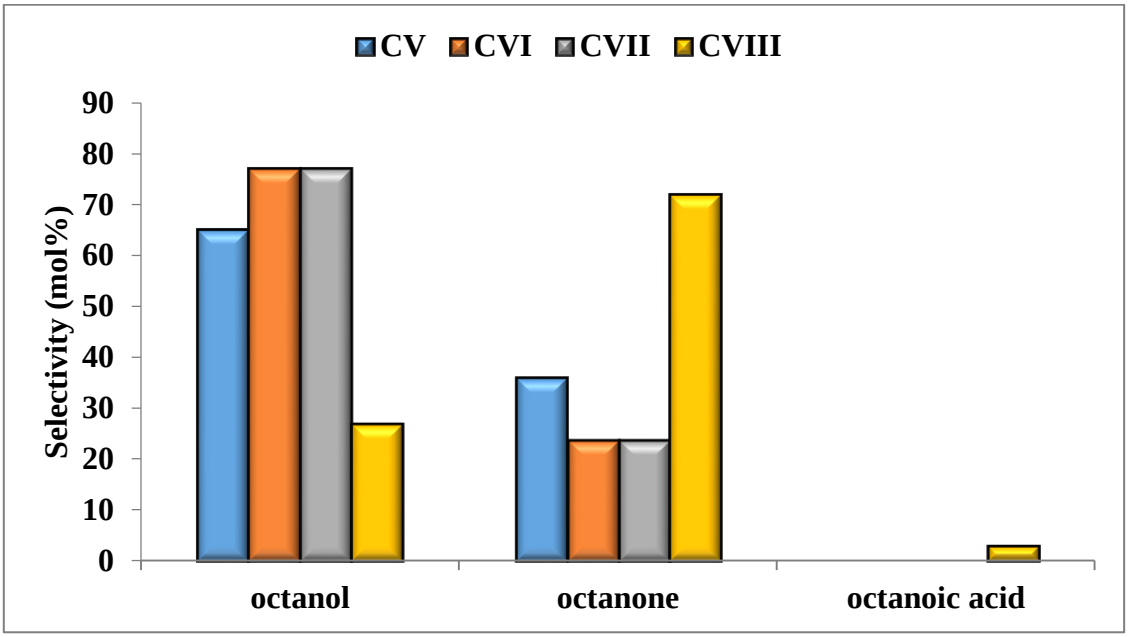

Figure 4.8: The product distribution profiles under the optimum conditions over catalysts **CV-CVIII** within 24 h.

Considering the product distribution of oxygenates formed in 24 hours, alcohols were found to be the dominant oxygenates produced, with the exception over catalyst **CVIII** (Fig. 4.8). The selectivities to alcohols were ca. 65-80% for catalysts **CV-CVII** with a low selectivity to ketones up to ca. 20-30%. Catalysts **CVI** and **CVII** were most selective to the alcohol products, whilst **CVIII** was most selective to the ketones (70%). The trend in alcohol formation may be attributed to a high concentration of alkyl hydroperoxides initially in the reaction mixture which was reduced upon addition of the reducing agent, PPh_3 (a key step in the quantification of oxygenates reported in literature).[16, 17] A possible reason for the pronounced selectivity to ketones for **CVIII** may be due to the catalyst becoming inactive

after 15 hours of reaction (Section 4.3.1.3, Fig. 4.16 of this report). This is supported by a blank study carried out using 2-octanol as a substrate. The oxidant *t*-BuOOH, in the absence of any catalyst, converted all of 2-octanol to 2-octanone between 6 and 9 hours of reaction. This highlights the activity of the catalyst in controlling the selectivity during the initial stages of the reaction and shows that the rate of over-oxidation (in the absence of a catalyst) is fast. The rate constant of **CVIII** is 0.0154 s^{-1} and shows that alcohols produced (until 15 hours of reaction) are more quickly over-oxidised to ketones than with **CVII** having a rate constant of 0.01055 s^{-1}, producing the most amount of alcohols and therefore a slower over-oxidation process is seen. The production of 2-octanol in the cases of **CV-CVII** was dominant, whilst 2-octanone was the predominant product formed for **CVIII**.

The selectivity to the terminal products, which include 1-octanol, octanal and octanoic acid showed no coherent trend over all the Co catalysts, since 1-octanol and octanoic acid were only produced by **CVIII** (Fig. 4.9). This information suggests that **CVIII** was the most regioselective catalyst in the cobalt series with the ability to attack the terminal carbon atom. Selectivity to trace amounts of 1-octanol was also observed in similar oxidation studies with *n*-octane, in which activation of the C-H bond at the C(1) position in the hydrocarbon chain using cobalt PNP and SNS pincer catalysts was observed, however, in those systems, ketones were produced as the dominant products within 24 hours.[2, 14] The 1-octanol to octanoic acid ratio is 3:1, where the formation of octanoic acid likely occurred through complete oxidation of octanal. Since the amount of octanoic acid is three times lower than that of 1-octanol, it can be concluded that the rate of over-oxidation over **CVIII** is rather slow and possibly controlled through the catalyst.

The activation of the C(2) position of the hydrocarbon chain produced 2-octanol and 2-octanone products for the cobalt catalysts as depicted in Fig. 4.10. This information shows that **CVI** and **CVII** were most selective to the C(2) position, followed by **CV**, whilst over-oxidation occurs at this carbon position for **CVIII** where the highest selectivity to ketones is observed.

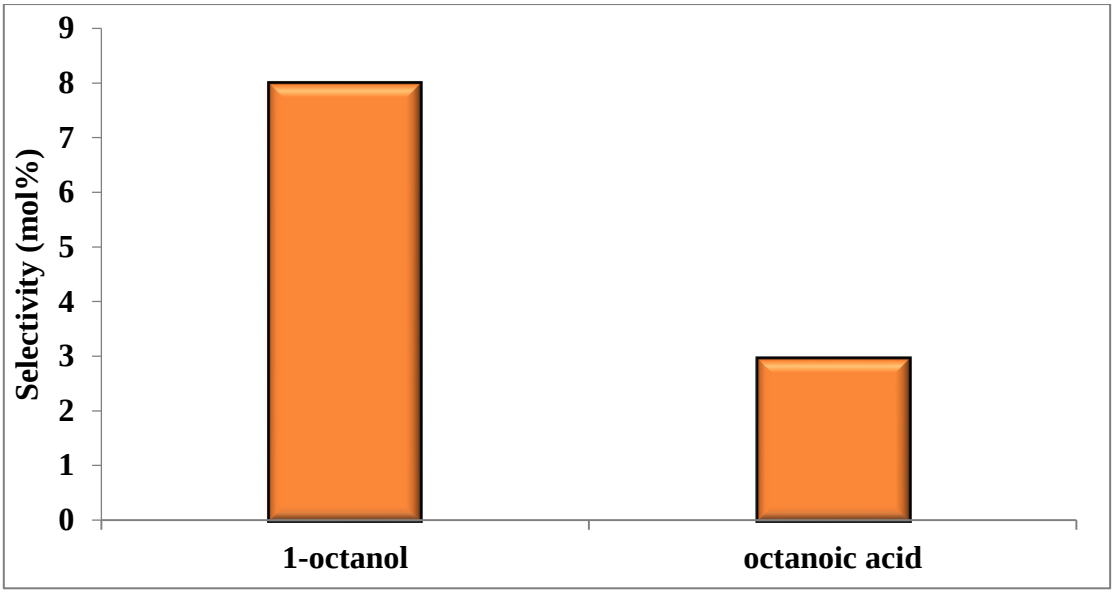

Figure 4.9: The selectivity to C(1) oxygenates produced over catalyst **CVIII** within 24 h.

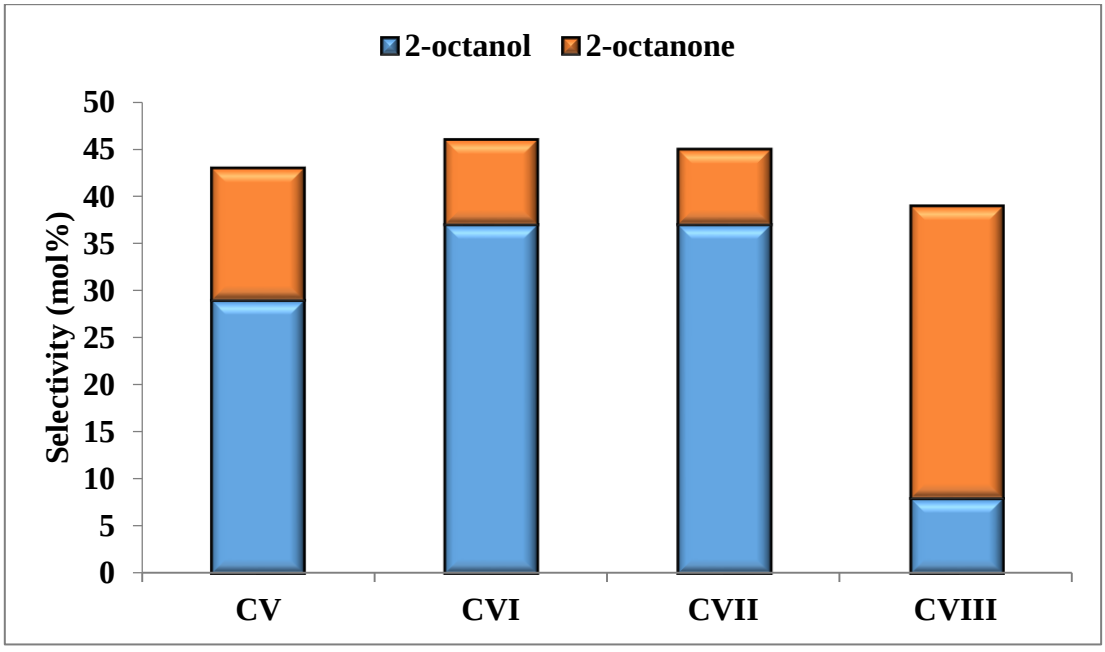

Figure 4.10: The selectivity to C(2) oxygenates produced over catalysts **CV-CVIII** within 24 h.

To track the rate of secondary oxidation of alcohols to ketones, a study with 2-octanol as the substrate was carried out over a 9 hour period, monitoring at 3 hour time intervals using **CVI** as the representative catalyst, since it was shown to be the most active in the Co series. From Fig. 4.11 it was evident that the production of ketones was relatively rapid, with the highest

conversion of 2-octanol (96%) observed at the end of 9 hours. It can be further concluded that although deeper oxidation occurs more quickly than *n*-octane activation (initiated within 3 hours), the rate at which it occurs in this study is still relatively slow, since at the end of 9 hours, some 2-octanol is still present in the system. To determine whether catalyst **CVIII** will convert 2-octanol faster than **CVI**, a reaction was done under the same conditions as with catalyst **CVI**. The results obtained show that the production of ketones occurs more slowly compared to **CVI**, since a conversion of 80% (compared to 96% for **CVI**) was observed over 9 hours. This suggests that the overall nature of the catalyst, in this case the rigidity, plays an important role in the rate of ketone production. Also, the rate of over-oxidation is slow during the initial stages of the reaction and occurs faster nearing the optimum time as seen from the time dependent studies shown later in this report. The blank study carried out further highlights the activity of the catalyst, since all of 2-octanol was oxidised to 2-octanone within 9 hours of reaction in the absence of the catalyst.

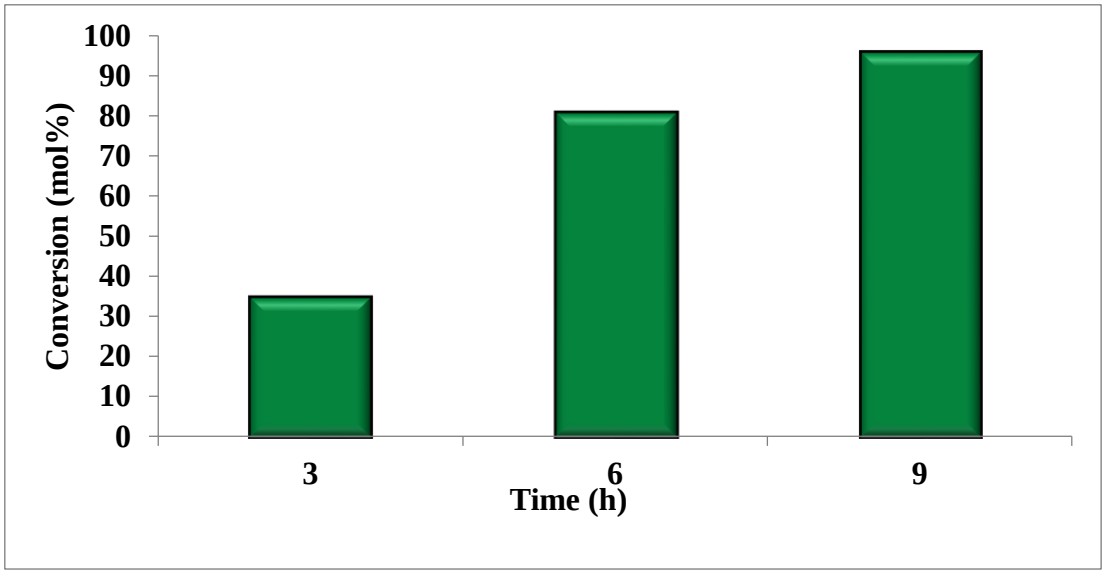

Figure 4.11: The conversion of 2-octanol within 9 h over **CVI**.

Considering the selectivity at the C(3) position (Fig. 4.12), the highest selectivity (18%) to 3-octanol was observed for catalysts **CVI** and **CVII**, with the lowest observed for catalyst **CVIII** (5%). The trend in the activation of the C-H bond at the C(3) position over all catalysts that produced a high amount of alcohols, may be attributed to the rigid nature of the catalysts in controlling the process of deeper oxidation.

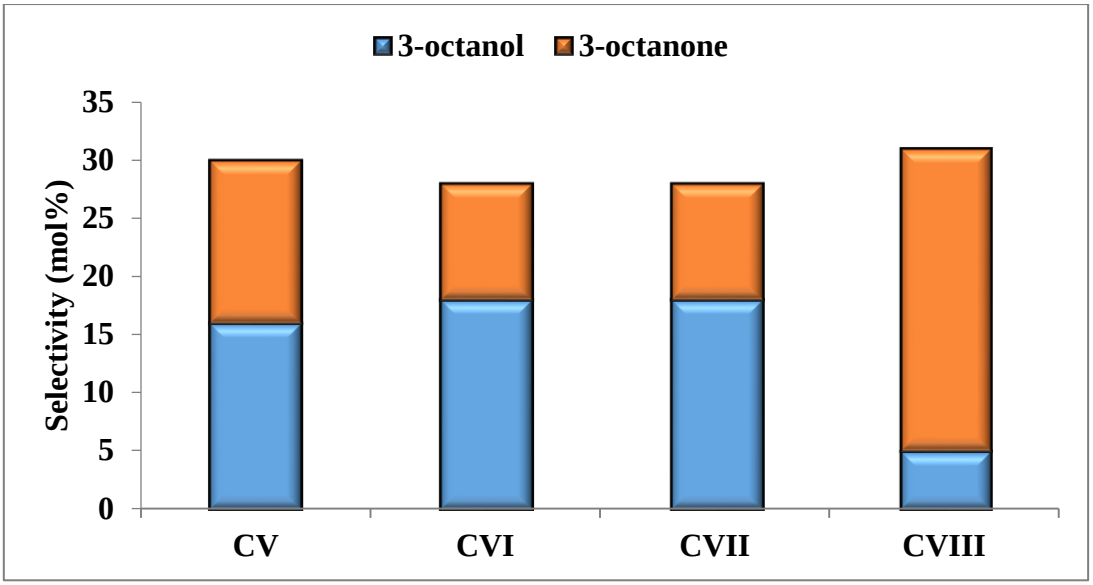

Figure 4.12: The selectivity to C(3) oxygenates produced over catalysts **CV-CVIII** within 24 h.

Activation at the C(4) position (Fig. 4.13) revealed that catalysts **CVI** and **CVII** gave the highest selectivity to 4-octanol (22%), with the lowest observed for catalyst **CVIII** (6%). Noteworthy is the increase in the amount of 4-octanol, produced with catalysts **CV-CVII** from 3-octanol (Figs. 4.12 and 4.13).

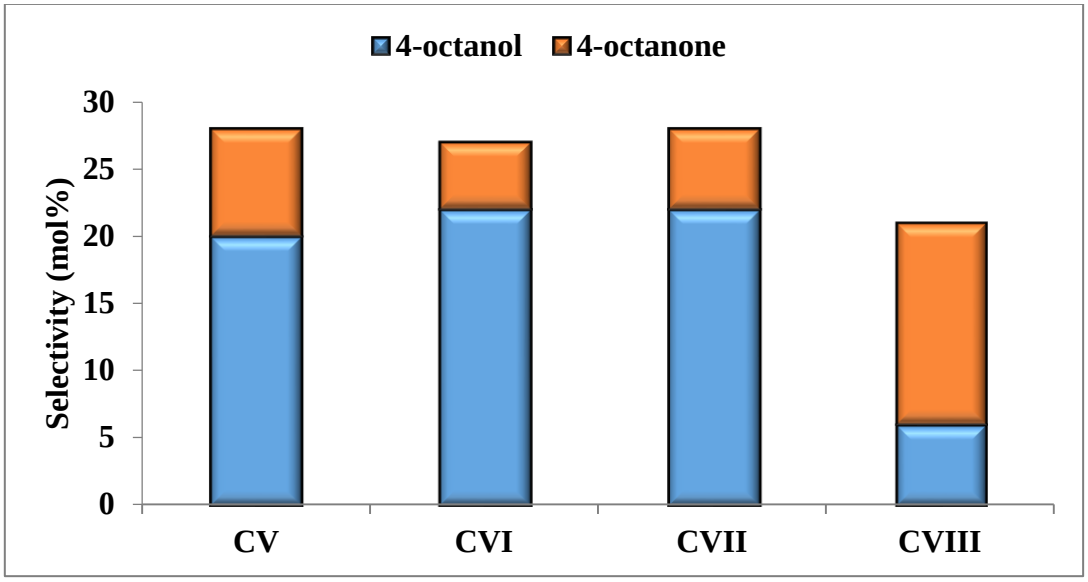

Figure 4.13: The selectivity to C(4) oxygenates produced over catalysts **CV-CVIII** within 24 h.

The data presented in Table 4.2 represents the regioselective parameter C(1):C(2):C(3):C(4), which provides information on the reactivity of the hydrogens at carbon positions 1, 2, 3 and 4 of the *n*-octane chain and are normalised by accounting for the number of hydrogens present on each carbon atom.[14]

The information shown in Table 4.2 illustrates that catalysts **CVI** and **CVII** were the most selective to the alcohol products with OH groups at the C(2), C(3) and C(4) positions, compared to catalysts **CV** and **CVIII** (entries 2 and 3). These catalysts were also significantly selective at C(2). Regarding the production of ketones, a general trend in the selectivity at the C(2), C(3) and C(4) positions was observed for all catalysts, with C(2) being the dominant position of attack for **CVIII**. The total regioselective parameter for each catalyst shows that all catalysts are selective to the C(2) position, which confirms that the hydrogens at this position are more reactive, with C(1) being the least reactive position, which is in accordance with literature reports.[5, 7] Furthermore, it is evident that **CVIII** was the only catalyst which showed selectivity at the C(1) position.

Table 4.2: Regioselectivity parameters C(1):C(2):C(3):C(4) in the oxidation of *n*-octane for **CV-CVIII**.

Entry	Catalyst	Alcohol C(1):C(2):C(3):C(4)	Ketone C(2):C(3):C(4)	Total[a] C(1):C(2):C(3):C(4)
1	**CV**	0:1.8:1:1.3	1.8:1.8:1	0:1.5:1.1:1
2	**CVI**	0:2.1:1:1.2	1.8:2:1	0:1.7:1:1
3	**CVII**	0:2.1:1:1.2	1.3:1.7:1	0:1.6:1:1
4	**CVIII**	1.6:1:1.2:1.1	2.1:1.7:1	1:3.5:2.8:1.9

[a] The total regioselective parameter accounts for all products (octanones, octanols, octanal and octanoic acid). All reactions were carried out at 80 °C with a catalyst loading of 1 mol%, an octane to oxidant ratio of 1:15, cyclopentanone as the internal standard and a reaction time of 24 hours.

In summary, the data presented shows that the C-H bond at the C(2) position is more reactive than the C-H bond at the terminal position since it is the strongest bond in the linear chain and is considered most difficult to cleave. Furthermore, the C(2) position is more sterically

accessible with C(2) isomers favoured thermodynamically according to thermodynamic calculations (ΔG).

4.3.1.3 Reaction rates and time dependent studies

In order to gain some mechanistic insight into the progress of the reaction within the optimum time period (24 hours), a time dependent study was carried out on each reaction, monitored at 3 hour time intervals. The information in Fig. 4.14 suggests that whilst **CVI** was the most active catalyst, **CVIII** was the least active at the end of 24 hours. From the data, it is also evident that a steady increase in conversion is seen for the first 6 hours of the reactions for all catalysts, which plateaus after 15 hours.

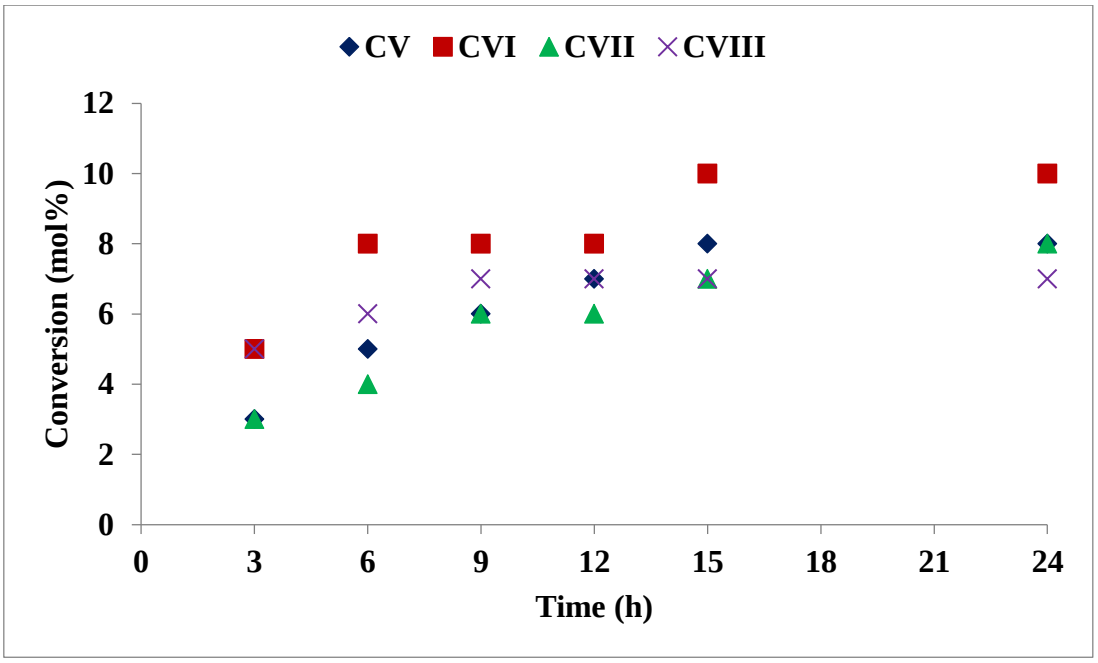

Figure 4.14: A time dependent study for catalysts **CV-CVIII** under the optimum reaction conditions.

The product distribution profiles of catalysts **CV-CVII** at specific time intervals reveals a general trend in which alcohol formation is dominant at the end of the 24 hour period, whereafter the formation of ketones is likely to take precedence through over-oxidation of secondary alcohols. The data reported in Fig. 4.15 shows clearly that alcohols decrease over time with a consequent increase in ketone formation. In the case of each catalyst (**CV-CVII**), the rate at which products of deeper oxidation form is seen to be rather slow, especially in the

case of **CV**, where products of over-oxidation are evident only after 9 hours of reaction (Fig. 4.15). This may be the effect of the catalyst limiting the production of ketones, which is known to be an inevitable process in the production of oxygenates through over-oxidation of the liner substrate. This effect can be further rationalised in the blank study (monitored over 3 hour time intervals) where the decrease in alcohol formation and increased formation in over-oxidised products highlights the importance of the catalyst and its contribution in producing alcohols in a relatively short space of time (Appendix A4, Fig. A4.4). Catalyst **CVIII** deviates slightly from the trend observed with catalysts **CV-CVII**, whereby the production of ketones at the end of 24 hours is prevalent (Fig. 4.16), which can be attributed to the fast reaction rate mentioned previously, although alcohols still dominate at 15 h. The remaining selectivity profiles for the other catalysts can be found in Appendix A4, Figs. A4.5 and A4.6.

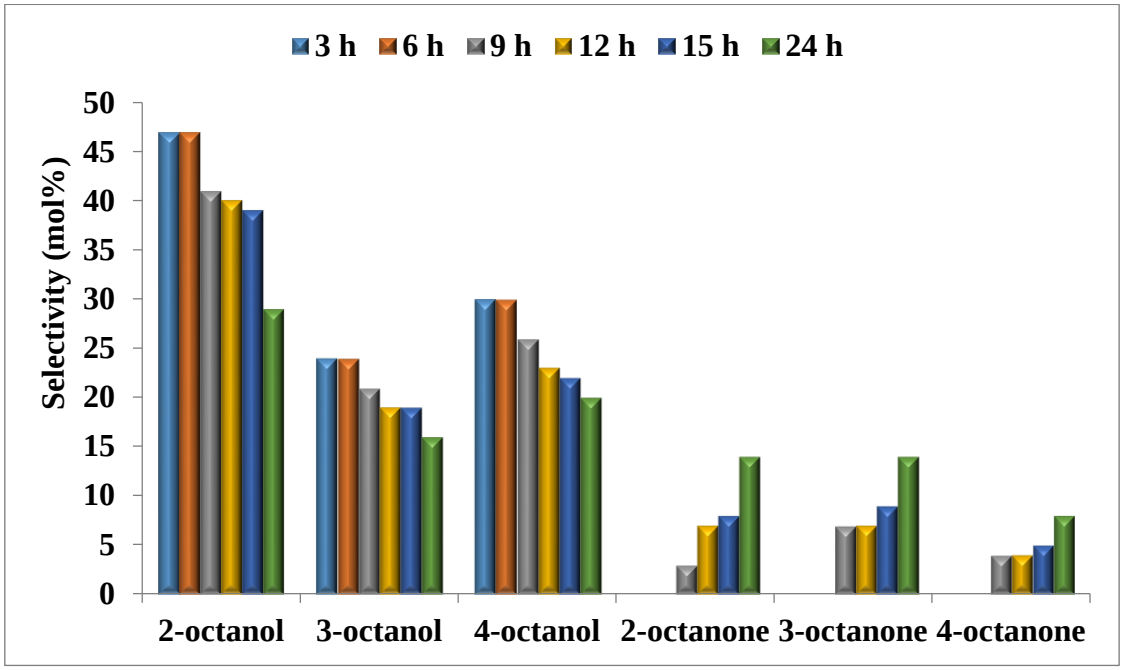

Figure 4.15: The product distribution profiles for **CV** over 3 h time intervals at 80 °C.

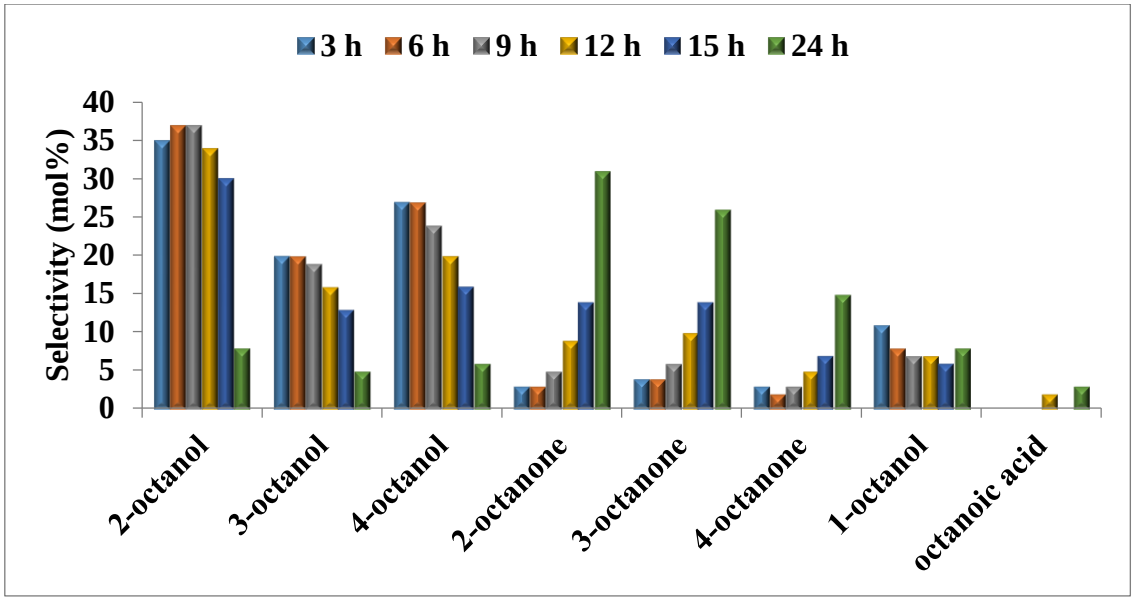

Figure 4.16: The product distribution profiles for **CVIII** over 3 h time intervals at 80 °C.

The turn over number (TON) results presented in Table 4.3 summarise the efficiency of each catalytic system over a 15 hour period. Catalyst **CVI** was the most efficient system with a TON of 10.2 with the least efficient being **CVIII** with a TON of 7.2. This implies that **CVI** produced the highest amount of product per unit mole of catalyst. Reports have shown Co systems, with *t*-BuOOH as the oxidant, to exhibit TONs in the mid-teens.[18] This shows that although there are rare reports on Co systems applied in the oxidation of hydrocarbons, this study shows promise for the development of Co systems by manipulating the substituents of the coordinated ligand to obtain higher catalytic activity and efficiency.

Table 4.3: The turn over numbers (TON) calculated for catalysts **CV-CVIII** over 15 hours.

Catalyst	TON[a]
CV	8.0
CVI	10.2
CVII	8.1
CVIII	7.2

[a]TON = moles total products (mol)/moles of catalyst (mol)

Investigating the initial rates of the reaction, using **CVII** and **CVIII**, the concentration of *n*-octane was seen to decrease linearly with time. Previous studies in hydrocarbon oxidation

have shown that constant conversion over time indicates a first order reaction with respect to the hydrocarbon.[18] Thus, to determine the rate of the reaction, a plot of ln of the concentration of *n*-octane against time (intervals 3-9 hours) was carried out (Fig. 4.17). The straight line obtained shows that the reaction order is one, in accordance with literature. The calculated rate constant was found to be 0.0154 mol dm^{-3} (purple line). It was found that among the Co series, **CVII** produced the most amounts of alcohols in 24 hours and the calculated rate constant of 0.0105 mol dm^{-3} (blue line) showed that this catalyst produced alcohols more slowly compared to **RIII** (rate constant of 0.0264 mol dm^{-3} shown later). This is expected since Ru is proposed as a more reactive metal than Co.

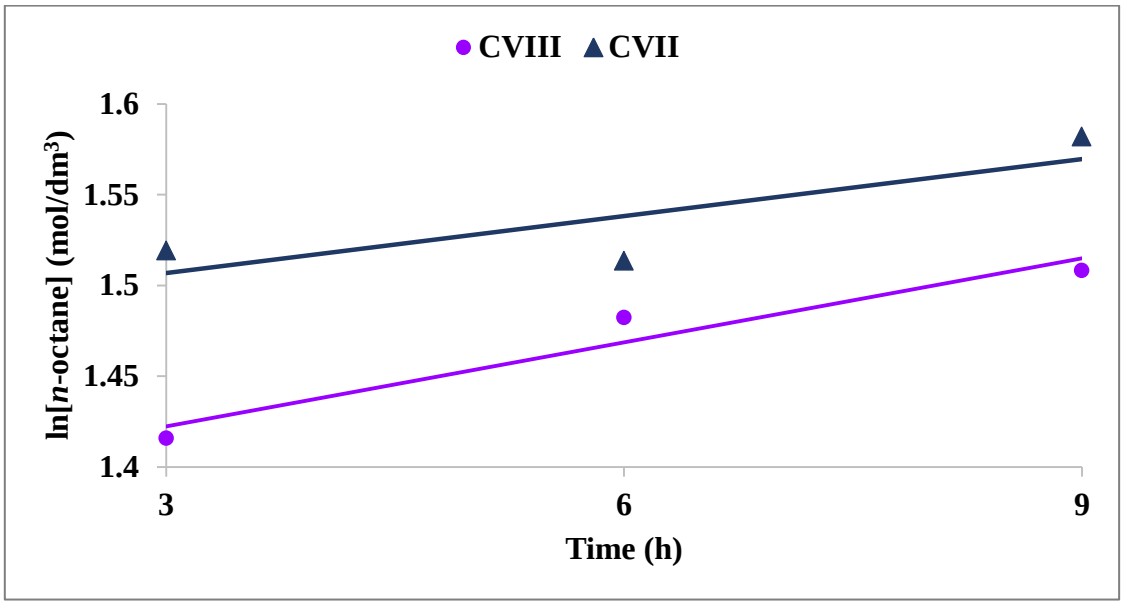

Figure 4.17: A plot of *n*-octane oxidation catalysed by **CVII** and **CVIII** with respect to time.

4.3.1.4 Radical scavenging and mechanism

From another perspective, TEMPO (2,2,6,6-tetramethylpiperidine-1-oxyl) is considered an efficient mediator in the oxidation of alcohols.[19-22] Hence, its cooperative action as a radical scavenger with the most active Co catalyst in this work, **CVI**, in the peroxidative oxidation of the alcohols to ketones, was worth investigating. Also, this might give further insight into the mechanistic pathway followed in the production of oxygenates from *n*-octane.

It was noted that at the end of 24 hours, the reaction (monitored at 3 hour time intervals for 9 hours) with the addition of TEMPO at five times the mol ratio of *n*-octane, was hindered as

there was a drop in conversion from 6% to 4% (within the first 3 hours) at a 1:12 substrate to oxidant ratio. This drop in conversion was associated solely to the activity of the radical scavenger, since a thorough investigation (without addition of TEMPO) on the progress of these reactions show that the catalysts do not deactivate over time. Reports have shown that a decrease in yield is related to the addition of the nitroxyl radical to the reaction system containing the catalyst.[23] When a radical trap (TEMPO) is added to the system, it reacts with *t*-BuO• and *t*-BuOO• radicals generated from *t*-BuOOH to form peroxides **1** and **2** according to the mechanism shown in Scheme 4.2. Studies have also shown that the abstraction of hydrogen atoms from alcohols as well as the production of the oxoammonium cation **3** through the oxidation of nitroxides, both occur *via* the presence of hydroxyl radicals.[23, 24] Furthermore, the selectivity profiles are different with the added TEMPO, where ketones dominate over time and this is expected since the oxoammonium cation **3** is considered an oxidant. This further confirms the reaction between TEMPO and the generated *t*-BuO• radicals produced upon reaction of the catalyst with *t*-BuOOH.

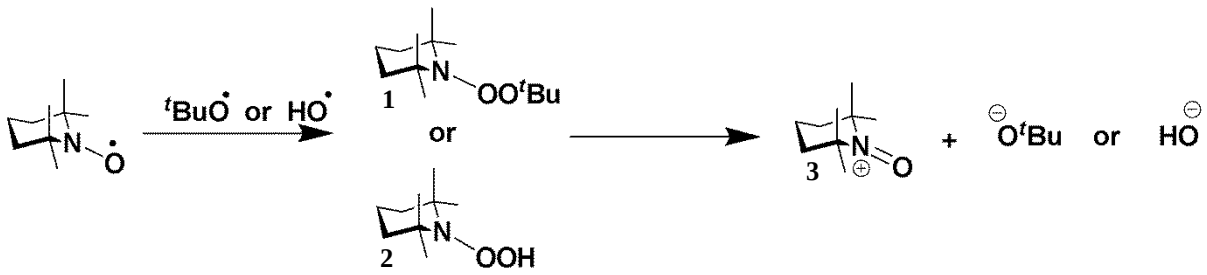

Scheme 4.2: Oxidation of TEMPO *via* *t*-BuO• and OH• radicals.

The observed colour change of the reaction mixture (without TEMPO) from pink to dark green, indicates the oxidation of Co(II) to Co(III) that ultimately forms a Co(III)-OOR species.[25] This Co(III)-alkylperoxide intermediate is considered crucial in the production of radicals and the decomposition of alkyl hydroperoxides.[25-27] Other studies have also shown specific Co systems to promote the decomposition of *t*-BuOOH to generate *t*-BuO• and *t*-BuOO• radicals.[28-31] A proposed mechanistic pathway in the oxidation of hydrocarbons by the Co-NNN-*t*-BuOOH system is presented in Scheme 4.3.

The initiation step involves the generation of the *t*-BuO• radical upon reduction of *t*-BuOOH *via* the Co^{2+}(NNN) catalyst (eq **1**). The produced Co^{3+}-hydroxo species can further react with *t*-BuOOH to produce Co^{3+}(NNN)(OOBu-*t*) and water (eq **2**). The generated *t*-BuOO• radical upon decomposition of Co^{3+}(NNN)(OOBu-*t*) (eq **3**) further decomposes to yield *t*-BuO•, (the

more reactive radical species) and oxygen (eq **4**). The reactive radical species then abstracts a hydrogen from the hydrocarbon substrate (RH) to produce R• radicals (eq **5**). Reaction of the R• radical with oxygen produces peroxo radicals ROO• (eq **6**) that can subsequently lead to the production of the alkyl hydroperoxide, ROOH (eq **7**). The production of the RO• radical upon the reaction between the Co^{2+}(NNN) species and ROOH (eq **8**) abstracts a hydrogen from the alkane (*n*-octane) to give rise to the alcohols and more R• radicals (eq **9**). This mechanism is postulated for catalysts **CV**-**CVII**, where predominantly alcohols are produced. For catalyst **CVIII**, where over-oxidation is evident over 24 hours, the peroxo radical, ROO• can either decompose to produce alcohols and ketones (eq **10**) or it can undergo a mixed bimolecular Russel termination to produce more ketones and *t*-BuOH (eq **11**), thus accounting for the increased selectivity to ketones. Furthermore, an increased production in ketones (eq **12**) is possible through over-oxidation of secondary alcohols catalysed by Co^{2+}(NNN) species, especially for catalyst **CVIII**.

Co^{2+}(NNN) + *t*-BuOOH ⟶ Co^{3+}(NNN)(OH) + *t*-BuO• **1**

Co^{3+}(NNN)(OH) + *t*-BuOOH ⟶ Co^{3+}(NNN)(OOBu-*t*) + H_2O **2**

Co^{3+} (NNN)(OOBu-*t*) ⟶ Co^{3+} (NNN) + *t*-BuOO• **3**

t-BuOO• ⟶ *t*-BuO• + ½ O_2 **4**

t-BuO• + RH ⟶ R• + *t*-BuOH **5**

R• + O_2 ⟶ ROO• **6**

ROO• + RH ⟶ ROOH + R• **7**

Co^{2+} (NNN) + ROOH ⟶ Co^{3+}(NNN)(OH) + RO• **8**

RO• + RH ⟶ ROH + R• **9**

2ROO• ⟶ ROH + R_{-H}=O + O_2 **10**

ROO• + *t*-BuOO• ⟶ R_{-H}=O + *t*-BuOH + O_2 **11**

ROH + *t*-BuOOH ⟶ R_{-H}=O **12**

Scheme 4.3: Proposed mechanistic steps in the oxidation of *n*-octane catalysed by Co-NNN-*t*-BuOOH systems **CV**-**CVII** and **CVIII**.

4.3.2 The oxidation of *n*-octane using H_2O_2 as the oxidant

The oxidation of *n*-octane was also investigated with H_2O_2 as the oxidant under the same reaction conditions used for *t*-BuOOH. Hydrogen peroxide is a common oxygen source in hydrocarbon oxidations and is advantageous in that it produces no waste and is therefore economical and environmentally friendly.[6, 8, 32, 33] The oxidation of *n*-octane with H_2O_2 was carried out under the optimised reaction conditions established using *t*-BuOOH, with **CVI** as the representative catalyst, chosen on the basis of it being the most active catalyst in the presence of *t*-BuOOH.

A comparison of the blank reaction (no catalyst) with those in the presence of the catalyst shows that this oxidant was more effective than *t*-BuOOH, giving a total conversion of 20% vs. 8% with *t*-BuOOH, at a substrate to oxidant ratio of 1:15 (Fig. 4.18). From this trend, the remaining Co catalysts were tested, where **CVII** showed to be the most active catalyst in the series, giving a total conversion of 23%. The least active catalyst, **CVIII**, gave a conversion of 6% and this lower catalytic activity compared to the other Co catalysts, may be due to the bulky nature of the catalyst, since **CV**-**CVII** has aliphatic substituents on the central N-donor atom that can freely rotate and thus create more access to the metal. Moreover, the product distribution profiles over all catalysts show that in 24 hours, predominantly alcohols are produced with little formation of ketone products (Fig 4.19), consistent with the trend observed for *t*-BuOOH.

The improved efficiency of the systems in H_2O_2 might be associated to an increased total volume of water compared to *t*-BuOOH. These findings relate to previous reports that show the promoting effect of water in a catalytic system on the product yield.[18, 34, 35] Also, the water in H_2O_2 solutions has been proposed to be directly involved in the generation of hydroxyl radicals.[36, 37] The increased alcohol formation can then be attributed to the decomposition of a high concentration of alkyl hydroperoxides produced, according to the mechanism in Section 4.1 of this report. Furthermore, over-oxidation to produce ketones, which is expected with a high content of peroxide, is hindered due to the high content of water in the system.

Since H_2O_2 is known to decompose over long reaction times and at high temperatures, quantification of this oxidant at the end of the reaction for **CVI** shows that despite being largely consumed in the reaction (from 0.05 mol initially to 1.3×10^{-4} mol), there is still availability of this oxidant at the end of 24 hours. Furthermore, quantification of the blank

reaction at the end of 24 hours shows that 8.9 x 10^{-3} mol are still available from the initial mols of peroxide (0.05 mol) at the end of 24 hours, which emphasises the role of the catalyst and that of the oxidant in producing isomeric oxygenates.

Further investigation into this oxidant at various substrate to oxidant ratios, as well as temperature effects on the conversion and selectivity, are currently underway. From this a comparative study to *t*-BuOOH will be done.

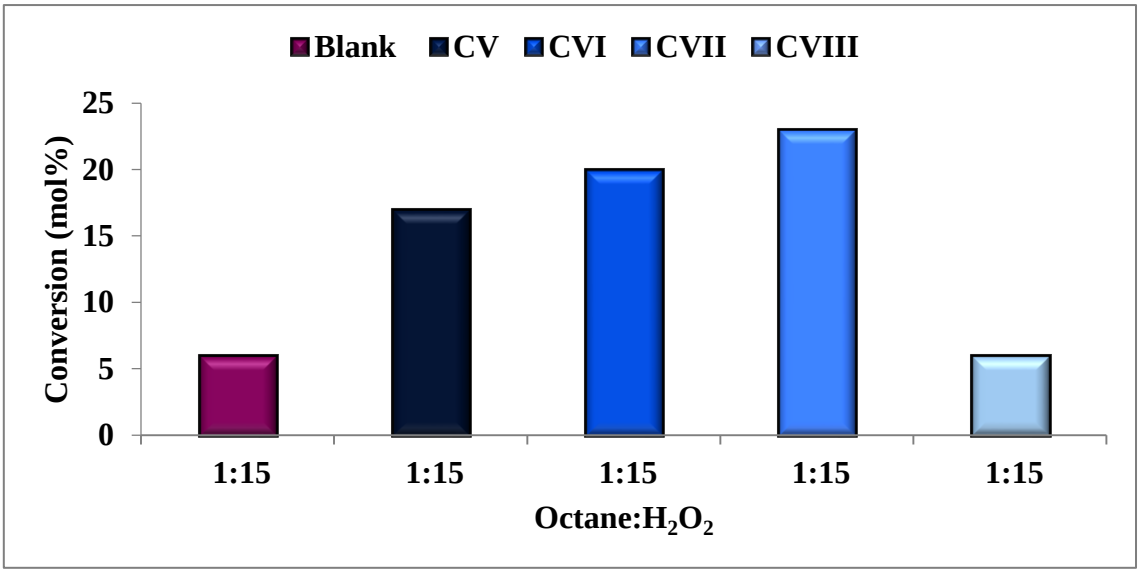

Figure 4.18: The total conversion of *n*-octane with H_2O_2 at 80 °C over 24 h for **CV-CVIII**.

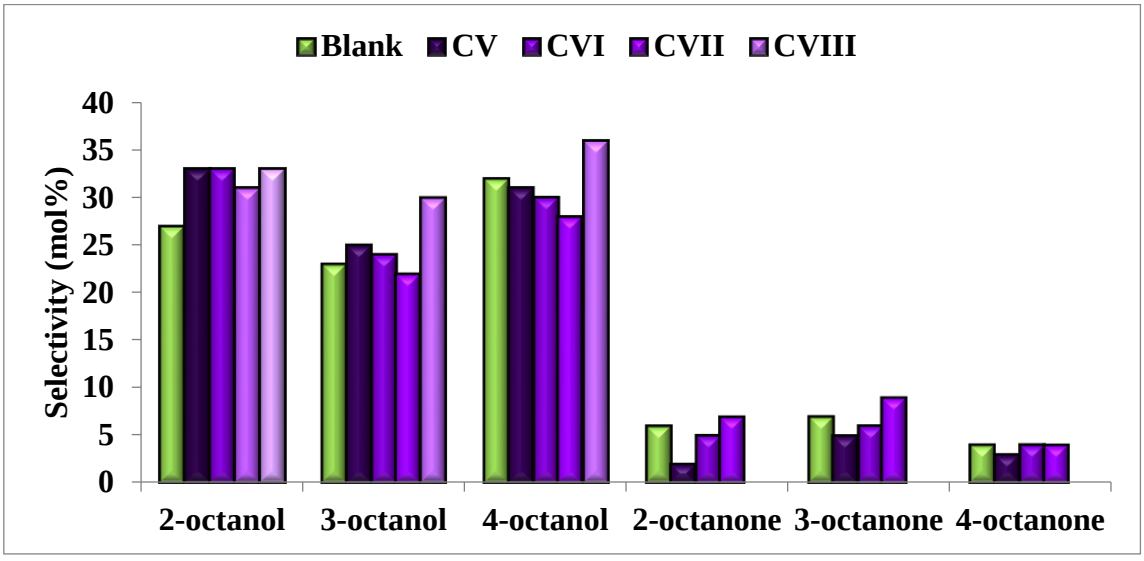

Figure 4.19: The selectivity profile showing products formed over 24 h at 80 °C with H_2O_2 for **CV-CVIII**.

4.3.3 Optimisation studies: time, temperature and *n*-octane to *t*-BuOOH ratio for the Ru systems

Studies investigating the time dependence of reactions catalysed by **RI** as the representative catalyst, were carried out using substrate to oxidant ratios of 1:3, 1:6, 1:9, 1:12 and 1:15 over 24 hour and 48 hour time intervals. The optimum time period was chosen based on the conversion of *n*-octane and the product distribution achieved over both time periods. Fig. 4.20 shows a linear increase in conversion at the varying substrate to oxidant ratios with the highest conversion observed over 48 hours at 13%, however, the selectivity profiles (Fig. 4.21 and Fig. 4.22) shows that over-oxidation of secondary alcohols becomes prevalent from 24 hours to 48 hours. There is less deeper oxidation within the first 24 hours, where a larger content of alcohols is seen which decreases as time proceeds (48 hours). This effect was also observed in the Co series, however, Ru seems to be more active in catalysing the over-oxidation of the substrate, producing more ketones. For these reasons, 24 hours was chosen as the optimum reaction time.

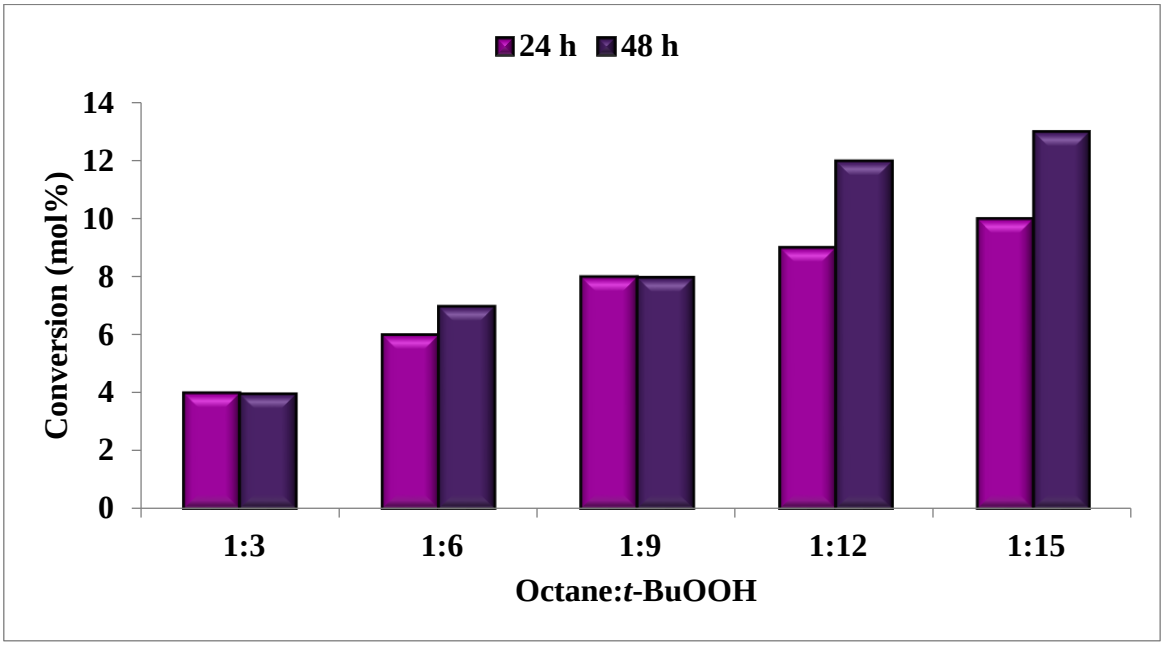

Figure 4.20: The total conversion of *n*-octane at 80 °C within 24 h and 48 h over **RI**.

The rationale for the Ru catalysts being more active than the Co catalysts and slightly more selective to ketone production in 24 hours, was attributed to the ligand pattern on the Ru catalysts. The benzene ring in the structure is capable of dissociating from the metal and thus

allows for easier binding of the substrate to the metal centre. This supports the observed higher conversions and rate of over-oxidation. Furthermore, due to enhanced access to the metal centre, the control over selectivity is reduced and thus accounts for a larger production of ketones.

Concerning the optimum substrate to oxidant ratio, the rate at which over-oxidation takes place, i.e. the rate at which the alcohol products are over oxidised to produce ketones, as well as the activity of the catalyst within 24 hours, were considered. Apart from these factors, a peroxide mol content of twelve times more than that of the substrate was chosen as the optimum ratio, since there was a negligible increase in the conversion of *n*-octane observed at the 1:15 substrate to oxidant ratio (Fig. 4.20).

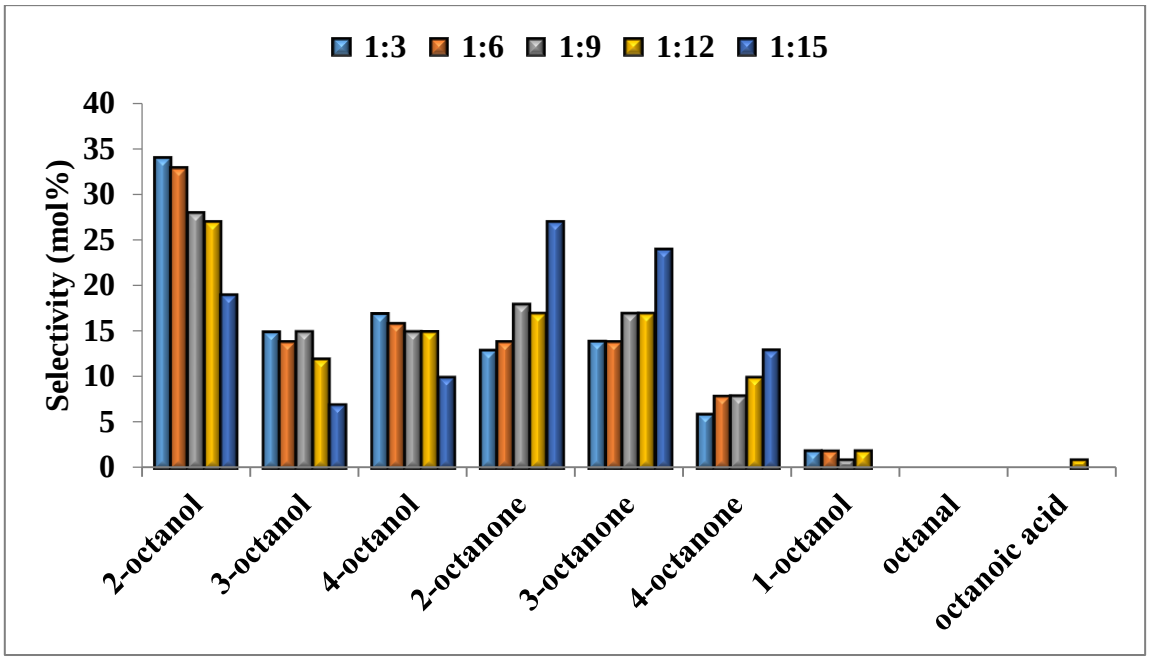

Figure 4.21: The selectivity profiles showing products formed over 24 h at 80 °C for **RI**.

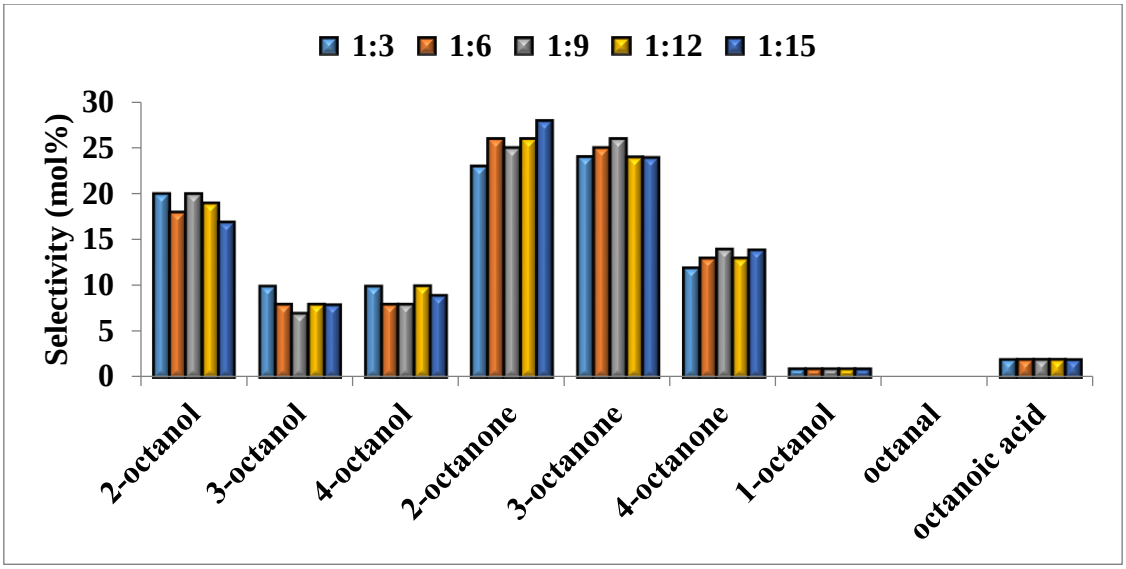

Figure 4.22: The selectivity profiles showing products formed over 48 h at 80 °C for **RI**.

The effect of temperature on the system was investigated using **RI** as a model catalyst at 50 °C and at room temperature. The conversions at room temperature and at 50 °C were 4% and 7% respectively (Fig. 4.23), further heating to 80 °C, as the optimum temperature, gave the highest conversion of 9% within 24 hours. The data in Fig. 4.24 shows that alcohols and ketones were produced at ambient temperature at almost at an equivalent ratio, with ketone products becoming more dominant at higher temperatures (50 °C and 80 °C).

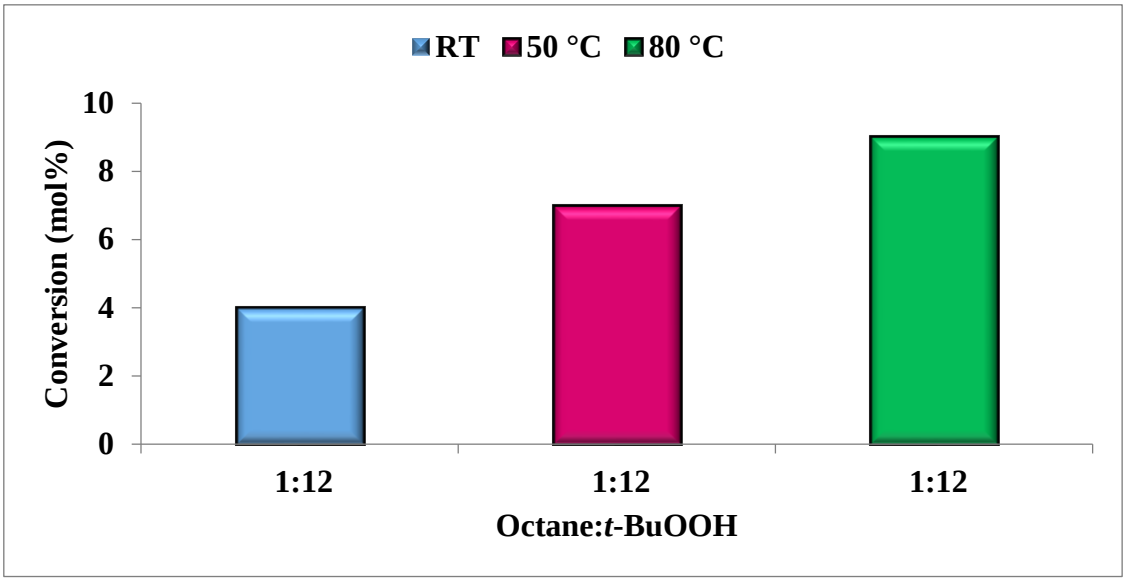

Figure 4.23: The total conversion of *n*-octane at room temperature and 50 °C over 24 h for **RI**.

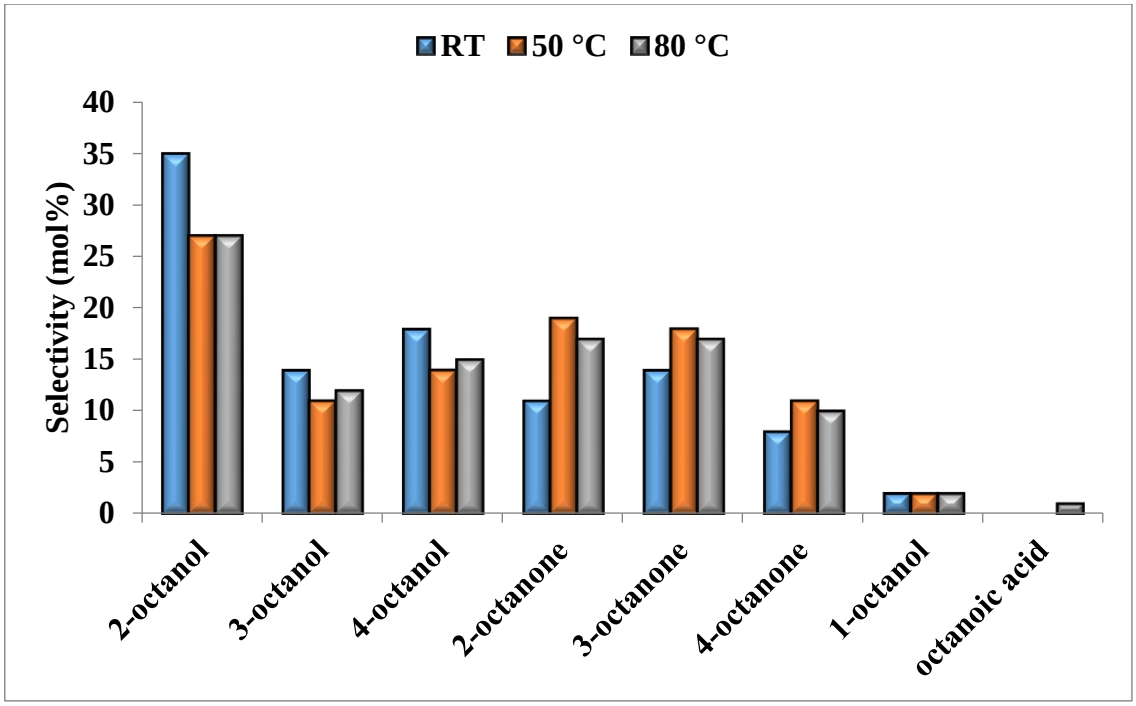

Figure 4.24: The product distribution profiles for **RI** at room temperature and 50 °C over 24 h.

4.3.3.1 Catalytic testing of Ru complexes RI-RIV at the optimum conditions

The oxidation of *n*-octane by *t*-BuOOH to produce isomeric oxygenates, i.e. alcohols, ketones, aldehydes and octanoic acid, were carried out with catalysts **RI-RIV**. The conversions obtained for each catalyst are reported in Fig. 4.25, with the selectivity profile showing the product distribution over 24 hours presented in Fig. 4.26. The information in Fig. 4.25 shows that catalysts **RII** and **RIV** exhibit the highest reactivities with a conversion of 12% at the end of 24 hours, whilst **RIII** was the least active, with a conversion of 7%. The rationale behind the observed trends is the same for the Co series, except for catalyst **RIV** which deviates from the expected lower conversion of *n*-octane. This is due to the bidentate catalyst (**RIV**) having a more accessible metal centre than the tridentate Ru catalysts (**RI-RIII**), thus allowing for greater access to the metal for the substrate to bind compared to **RI**, **RII** and **RIII**.

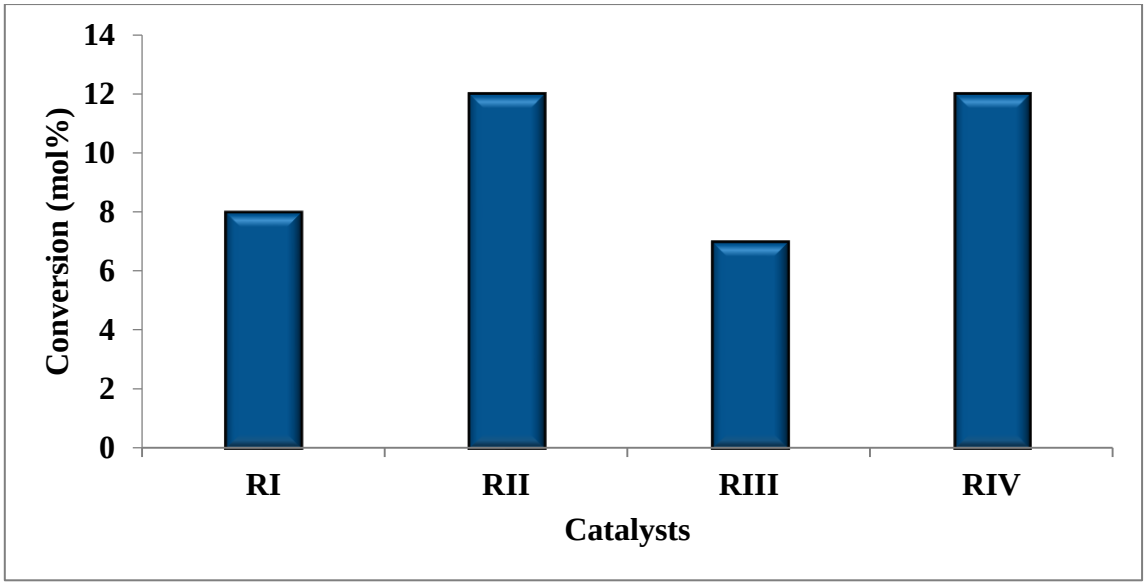

Figure 4.25: The total conversion of *n*-octane under the optimum conditions for catalysts **RI-RIV** within 24 h.

Fig. 4.26 depicts the product profile over each Ru catalyst in 24 hours, where an equivalent ratio of alcohols and ketones are formed in each case. This is associated to the aforementioned activity of Ru in which the over-oxidation process occurs relatively quickly as compared to the Co systems, where a large content of alcohols was produced. The selectivities to alcohols for catalysts **RI** and **RIV** were ca. 10-20%, whilst the highest production of alcohols was observed for catalysts **RII** and **RIII**, ca. 35-45%. The high concentration of ketones formed over catalysts **RI** and **RIV** may be attributed to ligand flexibility and the bidentate nature of **RIV**, respectively. In the case of **RI**, the free rotation of the propyl group may allow for improved accommodation of the substrate, which in turn offers less control over the selectivity, hence a high production of ketones within 24 hours is observed. With catalyst **RIV**, the cleavage of the benzene ring together with the bidentate nature of the catalyst, allows for enhanced access to the metal centre, which relates to the observed elevated production of ketones. The steric influences of catalysts **RII** and **RIII** are responsible for the high content of alcohols produced within 24 hours and therefore these catalysts are seen to offer more control over the selectivity than in the cases with catalysts **RI** and **RIV**. Furthermore, **RII** and **RIII** were the only catalysts among the Ru series in which alkyl hydroperoxides were produced (evident from the exothermic reaction), which were successfully reduced with PPh_3.[16, 17] The individual selectivity profiles of each catalyst can be found in Appendix A4, Fig. A4.7.

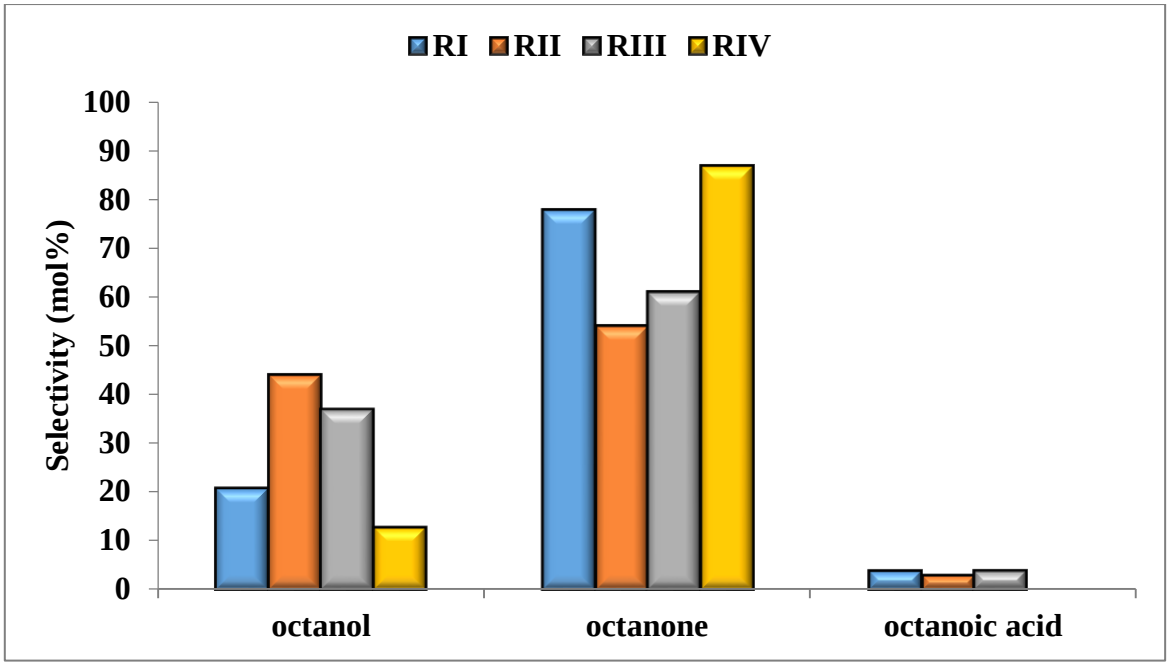

Figure 4.26: The product distribution profiles under the optimum conditions for catalysts **RI-RIV** within 24 h.

The activation of the terminal hydrocarbon, C(1), was successful with catalysts **RI**-**RIII** over which 1-octanol and octanoic acid were produced in 24 hours (Fig. 4.27). This suggests that the activation of this carbon position is ultimately associated to the high activity displayed by the Ru, since the C-H bond at the terminal position is the strongest in the hydrocarbon chain and considered the most difficult to cleave. It has also been well documented that catalytic intermediates controlled by free energies of activation can be selective and therefore C-H bond cleavage can be achieved if the system is sufficiently reactive to cleave a strong bond, in this case with the reactive Ru.[38-40]

The over-oxidation of 1-octanol to octanoic acid is likely very fast since no octanal was seen in the product. The rate of over-oxidation is further exemplified by the amount of octanoic acid produced which is twice the ratio of 1-octanol.

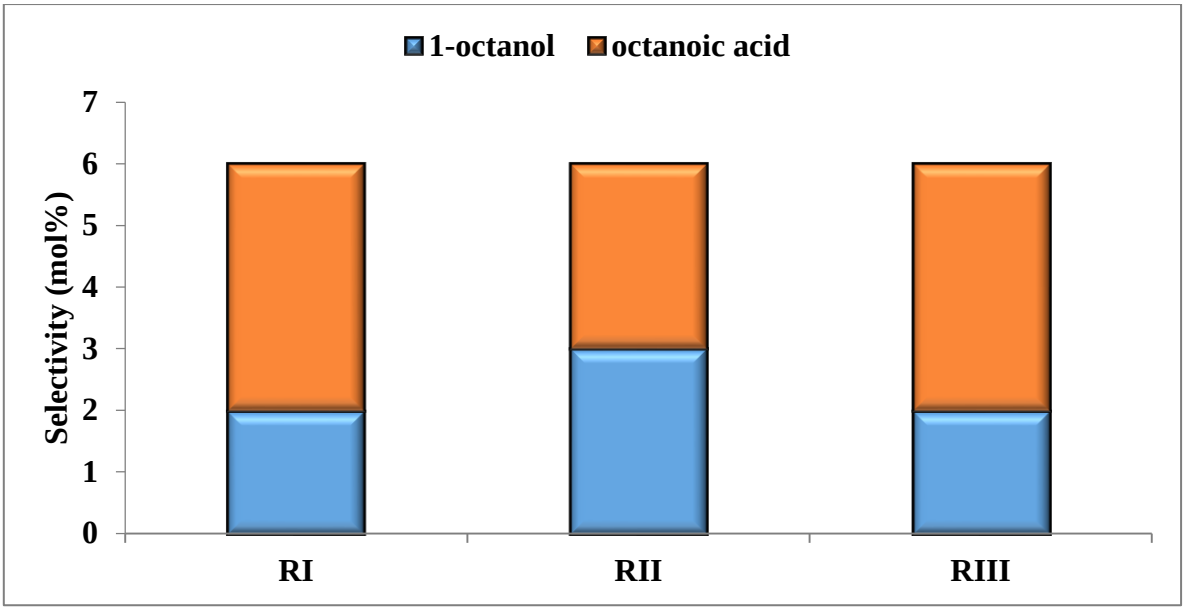

Figure 4.27: The selectivity to C(1) oxygenates produced over catalysts **RI-RIII** within 24 h.

Fig. 4.28 shows the activation at the C(2) position by all Ru catalysts which are predominantly selective to ketones. This information further illustrates that compared to the activation at the C(3) and C(4) positions (shown later), all catalysts are most selective to the C(2) position, giving predominantly ketones as a result of the increased rate of over-oxidation of the alcohols.

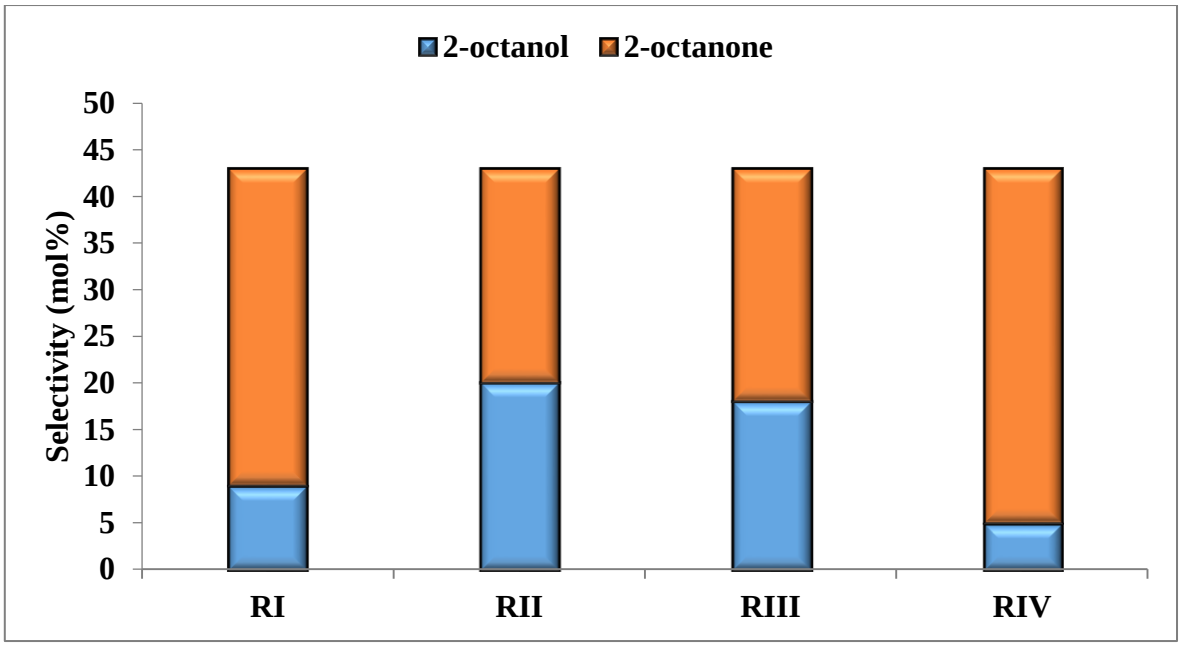

Figure 4.28: The selectivity to C(2) oxygenates produced over catalysts **RI-RIV** within 24 h.

The activity of the Ru complexes was further highlighted when a study was done on the rate of sequential over-oxidation using 2-octanol as the substrate instead of *n*-octane and **RII** as the representative catalyst. Results of this study showed that within the first three hours, all of 2-octanol was converted to the ketone. From this study, the rate of over-oxidation can firmly be attributed to the much higher reactivity of the Ru metal compared to the Co series, where over-oxidation occurred much more slowly over a period of 9 hours giving a total conversion of 96%.

The selectivity at the C(3) position (Fig. 4.29), shows that catalyst **RIV** gave the highest selectivity to 3-octanone (32%), with the lowest observed for catalyst **RII** (21%). Catalyst **RIV** showed the highest degree of over-oxidation. This trend was earlier attributed to the flexibility of **RI** and a greater accessible metal centre with **RIV**, where both these catalysts are more active than selective.

Activation at the C(4) position (Fig. 4.30) revealed that catalysts **RI** and **RIV** gave the highest selectivity to 4-octanone (14% and 17%, respectively). Catalyst **RII** was the least selective to 4-octanone giving a selectivity of 10%. These trends further show that **RIV** gave the lowest selectivity to the alcohol products within 24 hours.

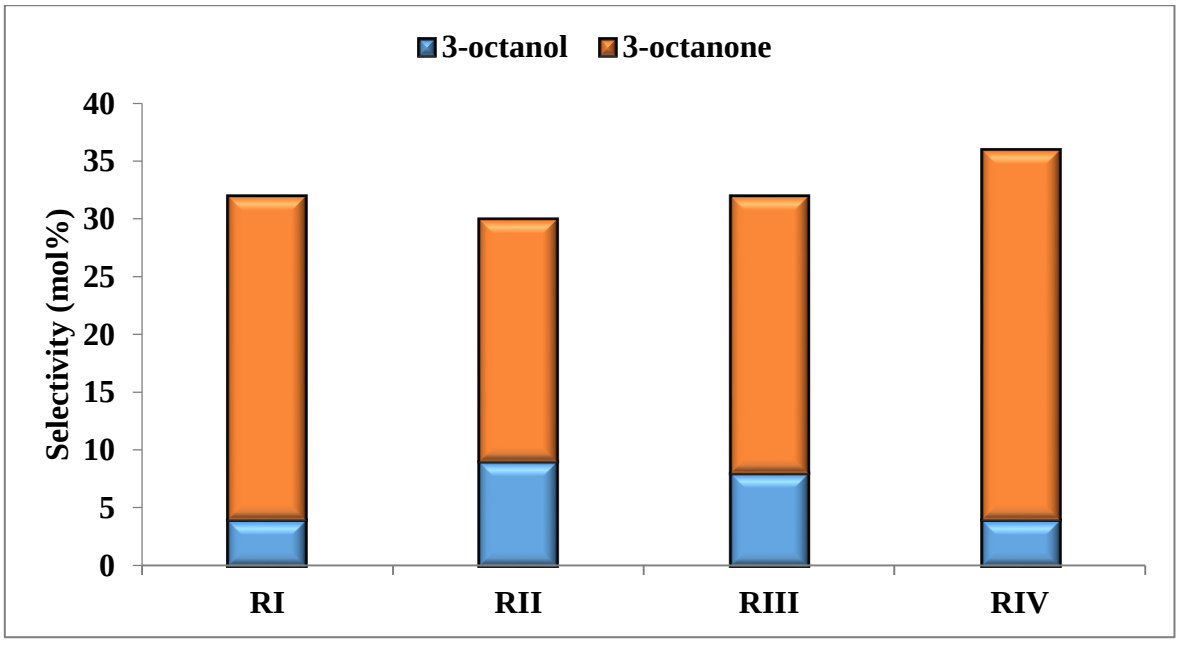

Figure 4.29: The selectivity to C(3) oxygenates produced over catalysts **RI-RIV** within 24 h.

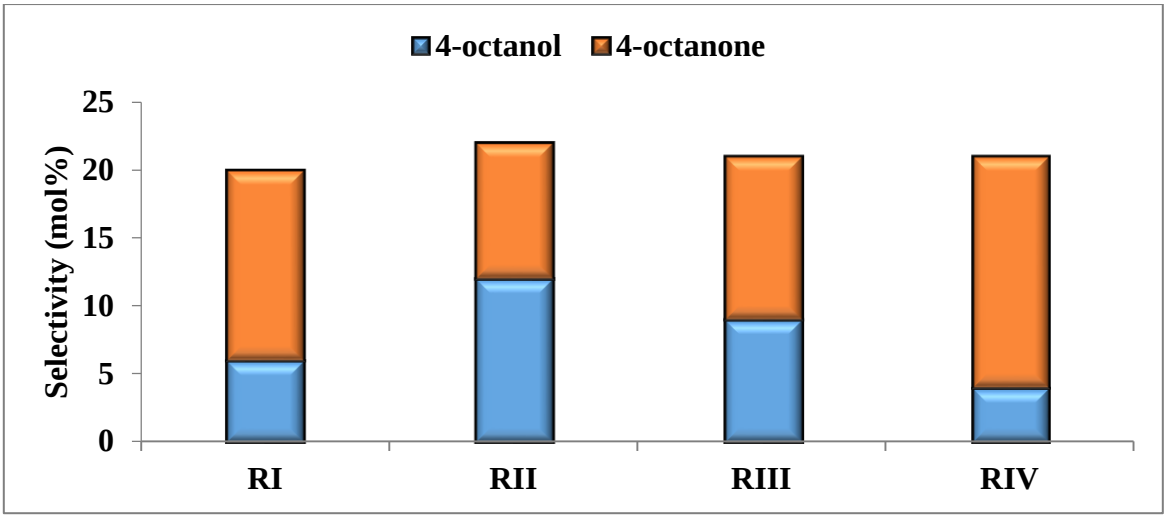

Figure 4.30: The selectivity to C(4) oxygenates produced over catalysts **RI-RIV** within 24 h.

Table 4.4 illustrates the regioselective parameter C(1):C(2):C(3):C(4) for all Ru catalysts. The information shows that catalyst **RIII** was most selective to the alcohol products at the C(1), C(2), C(3) and C(4) positions (entry 2) compared to catalysts **RI**, **RII** and **RIV** (entries 1, 2 and 4), where the lowest selectivity towards alcohols was observed for **RIV** (entry 4). Regarding the selectivity to ketones, a general trend was observed at the C(2), C(3) and C(4) positions among all catalysts, namely C(2) that was the dominant position of attack as this carbon position is more susceptible to oxidation compared to C(1) and according to thermodynamic calculations (ΔG), this gives the most stable product, thermodynamically.[41]

Table 4.4: Regioselectivity parameters C(1):C(2):C(3):C(4) in the oxidation of *n*-octane for **RI-RIV**.

Entry	Catalyst	Alcohol	Ketone	Total[a]
		C(1):C(2):C(3):C(4)	C(2):C(3):C(4)	C(1):C(2):C(3):C(4)
1	**RI**	1:7.5:3.3:5	1.2:1:1	1:10.8:8:5
2	**RII**	1:10:4.5:6	2.3:2.1:1	1:10.8:7.5:5.5
3	**RIII**	1:15:6.7:7.5	2.1:2:1	1:10.8:8:5.3
4	**RIV**	0:1.3:1:1	2.2:1.9:1	0:2:1.7:1

[a] The total regioselective parameter accounts for all products (octanones, octanols, octanal and octanoic acid). All reactions were carried out at 80 °C with a catalyst loading of 1 mol%, an octane to oxidant ratio of 1:12, cyclopentanone as the internal standard and a reaction time of 24 hours.

4.3.3.2 Reaction rates and time dependent studies

The activity of each Ru catalyst was monitored over 24 hours at 3 hour time intervals in order to gain further insight on the progress of the reactions (Fig. 4.31). All catalysts were very active over the initial 6 hour period where **RII** and **RIV** were observed to be more reactive than catalysts **RI** and **RIII**. Most reactions were almost complete after approximately 12 hours, which compared to the time-dependant studies carried out on the Co catalysts, where essentially complete reactions were reached within 15 hours. This implies that the Ru catalysts are highly reactive only for a short period of time and therefore the efficiency of each system can be judged within the first 12 hours of the reaction.

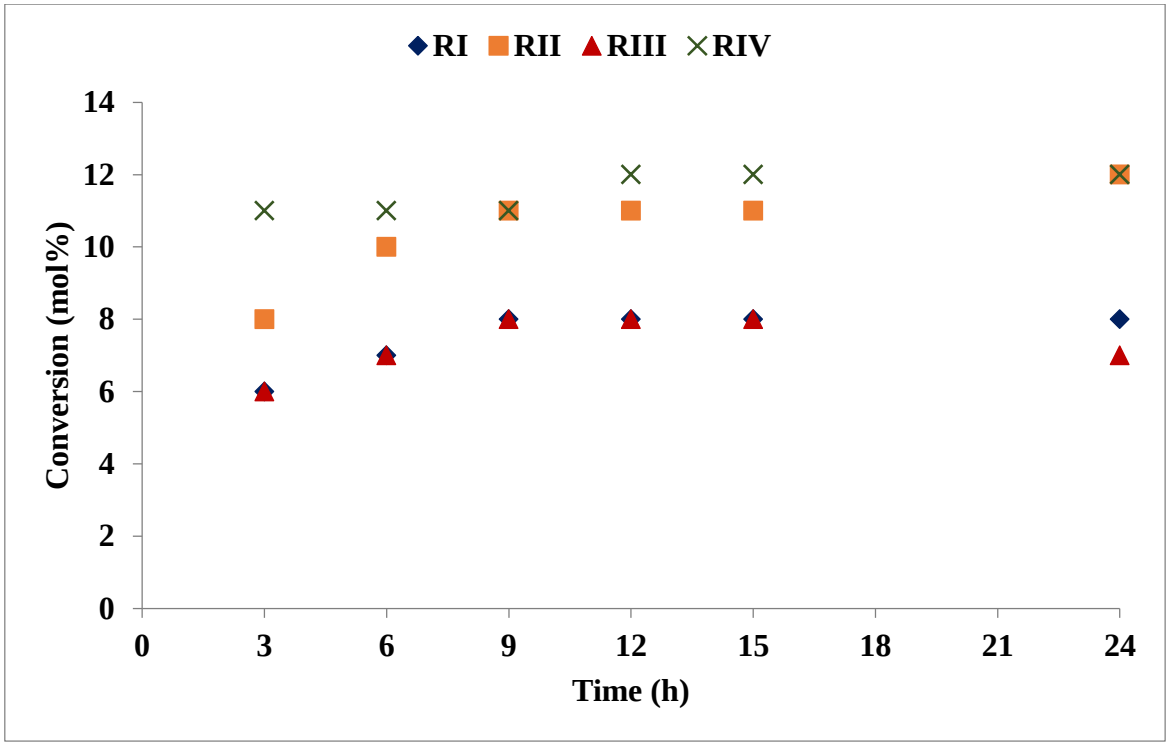

Figure 4.31: A time dependent study for catalysts **RI-RIV** under the optimum reaction conditions.

Regarding the production of isomeric oxygenates over 3 hour intervals for each catalyst, a general trend was observed where the C(2) position was the dominant position of attack (Fig. 4.32). For catalysts **RI-RIII**, 2-octanol was largely produced up to 15 hours. As time proceeded, the selectivity to alcohols, resulting from the activation of the C(2), C(3) and C(4) positions of the hydrocarbon chain, decreased. This suggested that a parallel mechanism was

involved in which each of the catalysts were responsible for the initial production of alcohols that subsequently over oxidised to produce ketone products, which was noted to be significantly more pronounced after 24 hours. An exception to this trend was noted for **RIV**, where substantial selectivity to ketones, through activation of the C(2), C(3) and C(4) positions, was observed from the initial 3 hour period through to 24 hours and may be attributed to **RIV** being a catalyst with a bidentate ligand giving greater accessibility to the metal compared to **RI**, **RII** and **RIII** (pincer complexes), thus decreasing the steric influences of the catalyst on the conversion and selectivity to oxygenates (Fig. 4.33). Furthermore, the dominant position of attack was the C(2) position, as noted with the other catalysts. Other Ru catalyst selectivity profiles can be found in Appendix A4, Figs. A4.8 and A4.9.

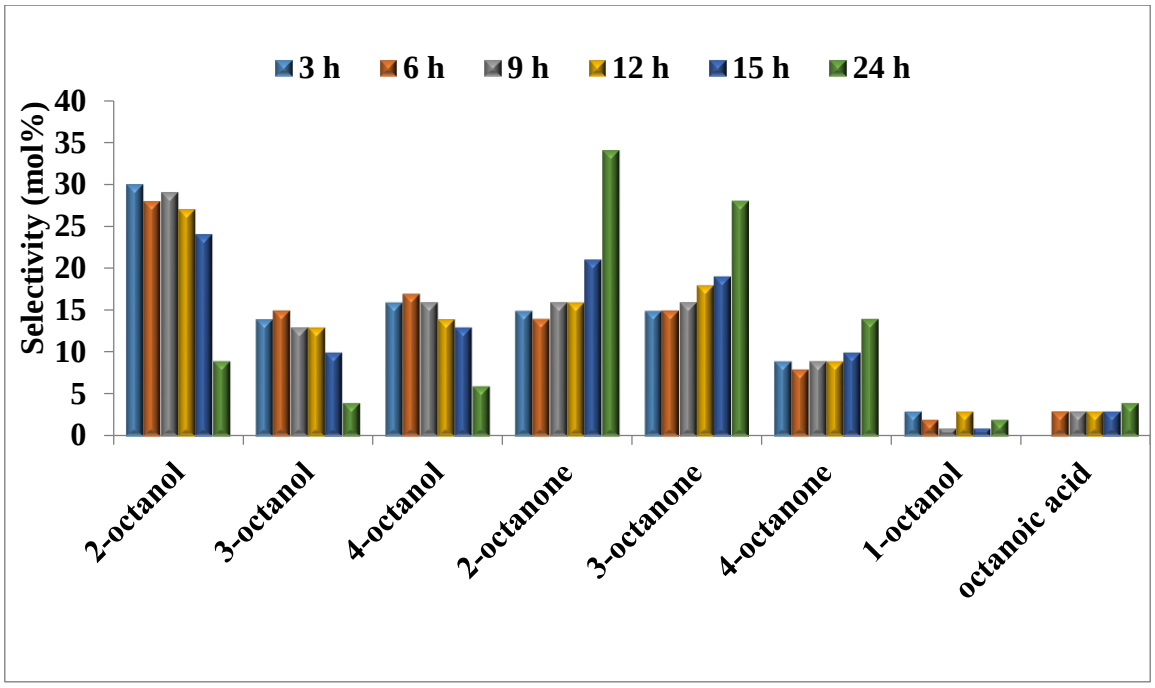

Figure 4.32: The product distribution profiles for **RI** over 3 h time intervals at 80 °C.

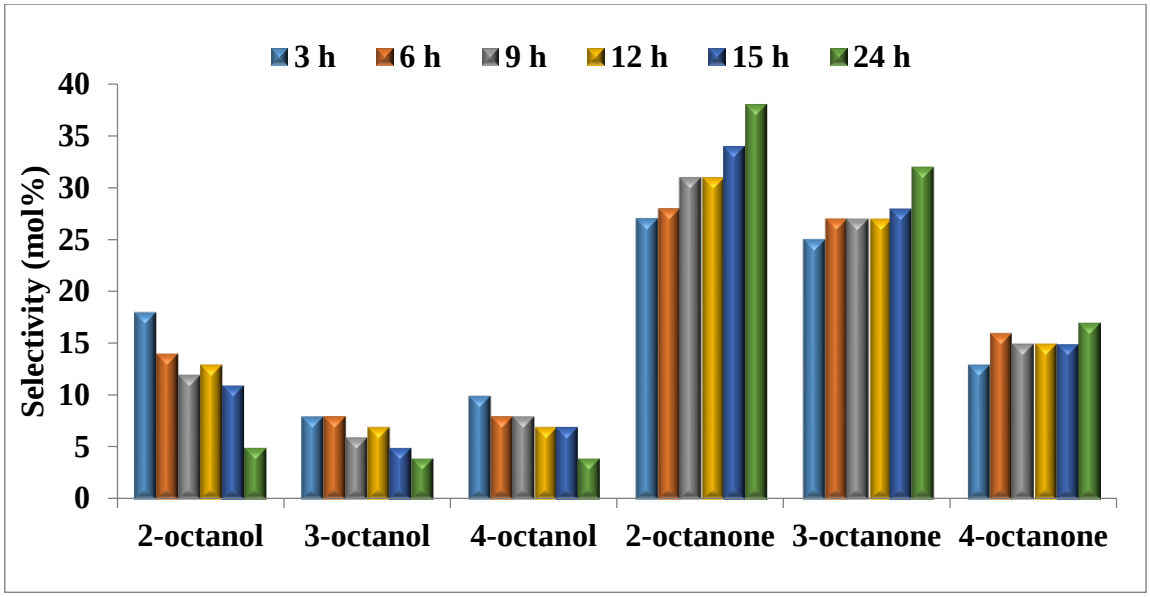

Figure 4.33: The product distribution profiles for **RIV** over 3 h time intervals at 80 °C.

Since all reactions catalysed by the Ru catalysts were essentially complete within the first 12 hours (from the time-dependent study carried out), the efficiency of each system was analysed based on their turn over numbers at this time period. The results presented in Table 4.5 show that **RIV** was the most active catalyst with a TON of 12.6 followed by **RII** with a TON of 11.1, whilst **RI** and **RIII** were the least active having a TON of 8.2. Since the activities of the Ru and Co catalysts, at the 1:12 (Ru) and 1:15 (Co) substrate to oxidant ratios are essentially the same, except for catalysts **RIV**, the expected TONs should be similar.

Table 4.5: The turn over numbers (TON) calculated for catalysts **RI-RIV** over 12 hours.

Catalyst	TON[a]
RI	8.2
RII	11.1
RIII	8.2
RIV	12.6

[a]TON = moles total products (mol)/moles of catalyst (mol)

A calculation of the initial rates of the reaction using **RIV** as a model system shows that each reaction proceeds through first order kinetics. The rate constant of 0.0422 mol dm^{-3} calculated further indicates that, like with Co, these reactions proceed quickly initially (from the steep slope of the graph of Fig. 4.34 (purple line). It was also found that **RIV** is four times more

reactive than **CVIII** within 9 hours into the reaction. Thus, from this study, Ru proves to be a better metal in that it gives greater conversion in less time, having a faster reaction rate relative to Co. However, the alcohol selectivity is lower with the same rationale mentioned earlier.

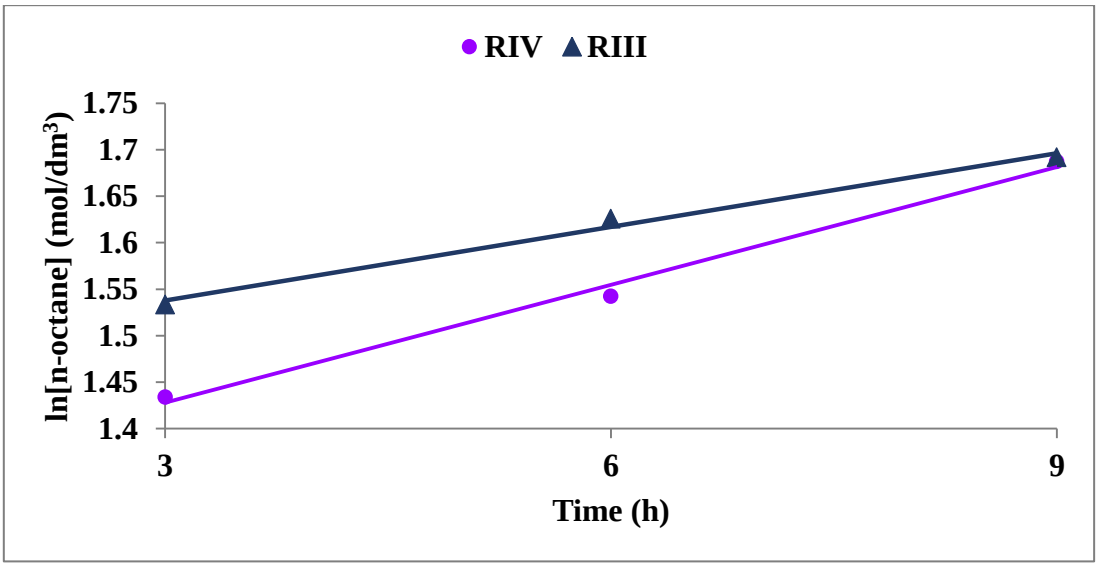

Figure 4.34: A plot of *n*-octane oxidation catalysed by **RIII** and **RIV** with respect to time.

Whilst **CVIII** and **RIV** produce the most amounts of ketones, it was worth investigating the rates of the catalysts that are selective to predominantly alcohols. It is noted that within the first 9 hours of the reaction for catalyst **RIII**, and a rate constant of 0.0264 mol dm^{-3} (represented by the blue line), alcohols are produced rather slowly than in the case with **RIV**, and this is expected due to the steric effect of **RIII**.

4.3.3.3 Radical scavenging and mechanism

To gain further understanding into the mechanistic pathway followed in the production of oxygenates from *n*-octane, the radical scavenger TEMPO was employed. As mentioned earlier, this radical scavenger is considered efficient in the oxidation of alcohols. Therefore, a study done at the optimum conditions, using **RII** as a model catalyst with added TEMPO, produced predominantly ketones due to the formation of the oxoammonium cation which is also an oxidant.

The observation at the end of 24 hours concisely confirmed that a radical mechanism may have been involved since the reaction was significantly hindered upon addition of five equivalents of the radical scavenger relative to the substrate. Thus, the conversion after 24 hours was half the conversion found where TEMPO was omitted in the reaction. This drop in conversion from 12% to 4% was associated solely to the activity of the radical scavenging ability of TEMPO and this trend is consistent with reports that relate a decrease in yield to the addition of a nitroxyl radical from TEMPO in the reaction system containing the catalyst.[23]

The proposed mechanism for the oxidation of *n*-octane catalysed by the Ru NNN catalysts is outlined below, where two pathways, A and B, are considered possible according to Muruhashi *et al*[13]. The ruthenium complex **1**, Ru^{2+}(NNN) reacts with *t*-BuOOH to produce an alkylperoxo-ruthenium(II) complex, **2**. This complex then provides an oxo-ruthenium(IV) species, **3**, through homolytic cleavage of the O-O bond in the alkylperoxo-ruthenium(II) complex. Abstraction of a hydrogen atom from the hydrocarbon *via* the oxo-ruthenium(IV) species gives a Ru^{3+}OHR• radical. The catalytic cycle becomes complete upon transfer of the hydroxy ligand to the R• radical which affords the alcohol, ROH and the Ru^{2+}(NNN) species. Further oxidation of the secondary alcohols results in the corresponding ketones.

When the R• radical (**4**) has a low oxidation potential, fast single electron transfer takes place to give cation **5** (pathway B). This cation reacts with a second molecule of *t*-BuOOH to give the corresponding *tert*-butyldioxy product and water.

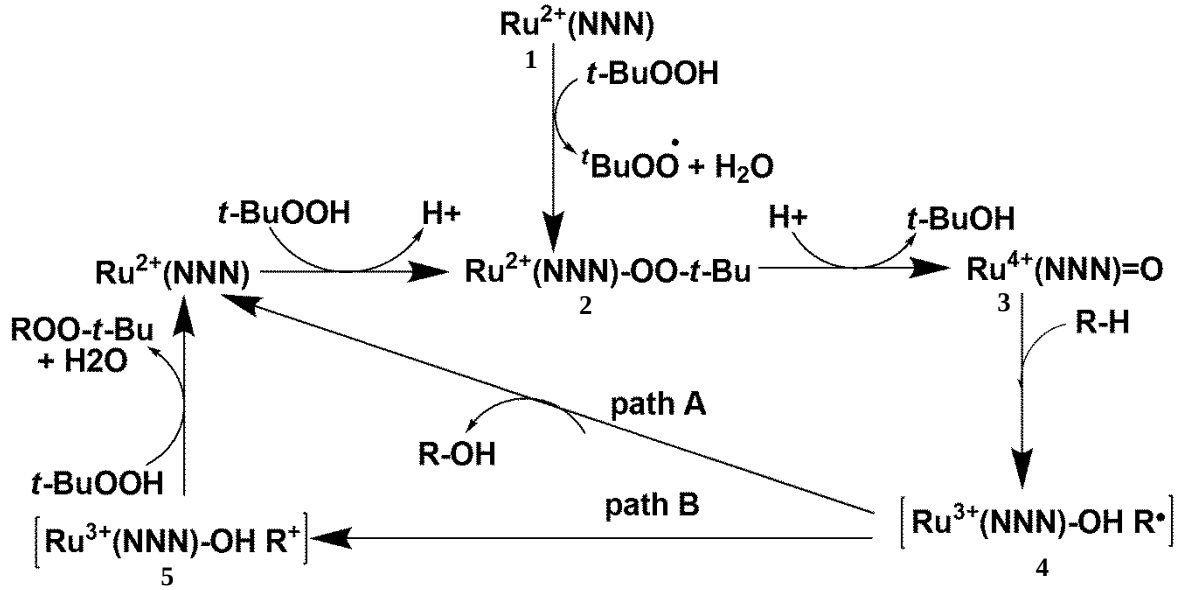

Scheme 4.4: A plausible mechanism in the oxidation of *n*-octane catalysed by **RI**-**RIV** with *t*-BuOOH.

4.3.3.4 The oxidation of *n*-octane using H_2O_2 as the oxidant

An investigation into the oxidation of *n*-octane, using H_2O_2 as the oxidant, was also carried out under the initial optimised conditions established with the Ru series using **RII** as the representative catalyst.

Comparing the results based on the blank reaction to the one in the presence of the catalyst under optimum conditions (1:12 substrate to oxidant ratio at 80 °C over 24 hours), showed promising results. These results further highlighted the role of the catalyst under the subjected reaction conditions in which a total conversion of 23% was achieved in 24 hours (Fig. 4.35). Catalytic testing of the remaining catalysts show that complex **RIV** was least active in the conversion of *n*-octane giving a total conversion of 7% at the end of 24 hours, with the rationale consistent to the catalyst being more prone to peroxidative attack, due to a less sterically hindered catalyst. The product distribution profiles (Fig. 4.36) show a large formation of alcohols in 24 hours with very little selectivity to ketones, which may be due to a lower content of peroxide (1:12) used in this system (Ru/H_2O_2) compared to 1:15 for the Co/H_2O_2 system that produced higher amounts of ketone products. Overall, the high yield of oxygenates by catalysts **RI-RIII** may be associated to the aforementioned promoting effect of water in the system, apart from the reactivity displayed by the Ru catalyst, which originates from the amount of peroxide added, since water makes up 70% of the total volume of hydrogen peroxide.[18, 34, 35] The quantification of H_2O_2 at the end of the reaction proved that a substantial amount was indeed consumed to produce the various oxygenates, with an amount of 8.3×10^{-4} mol remaining compared to the starting amount of 0.04 mol. The blank reaction showed a lower consumption of H_2O_2 (from 0.05 mol to 7.2×10^{-3} mol) which is indeed expected in the absence of the catalyst.

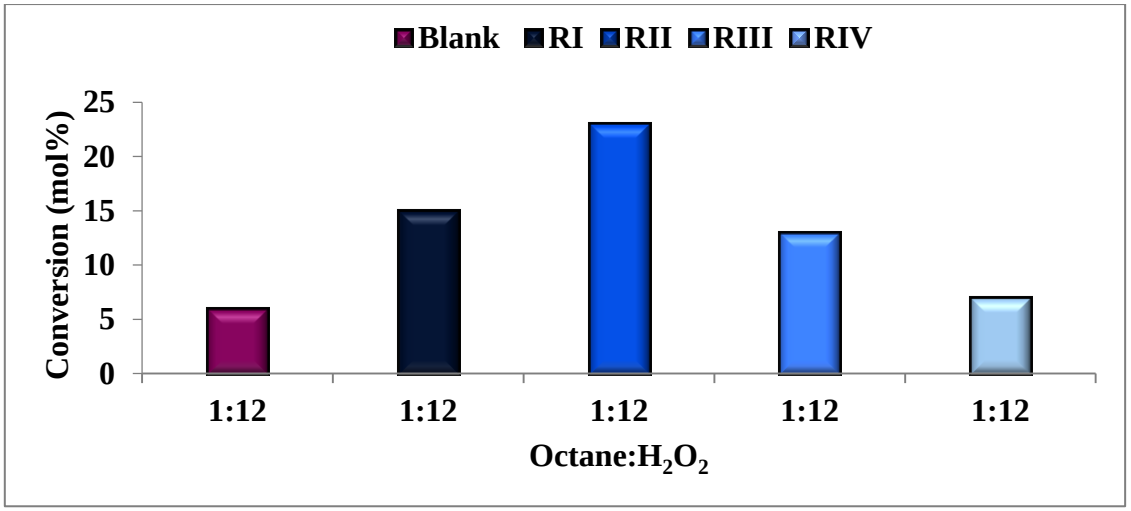

Figure 4.35: The total conversion of *n*-octane with H_2O_2 at 80 °C over 24 h for **RI-RIV**.

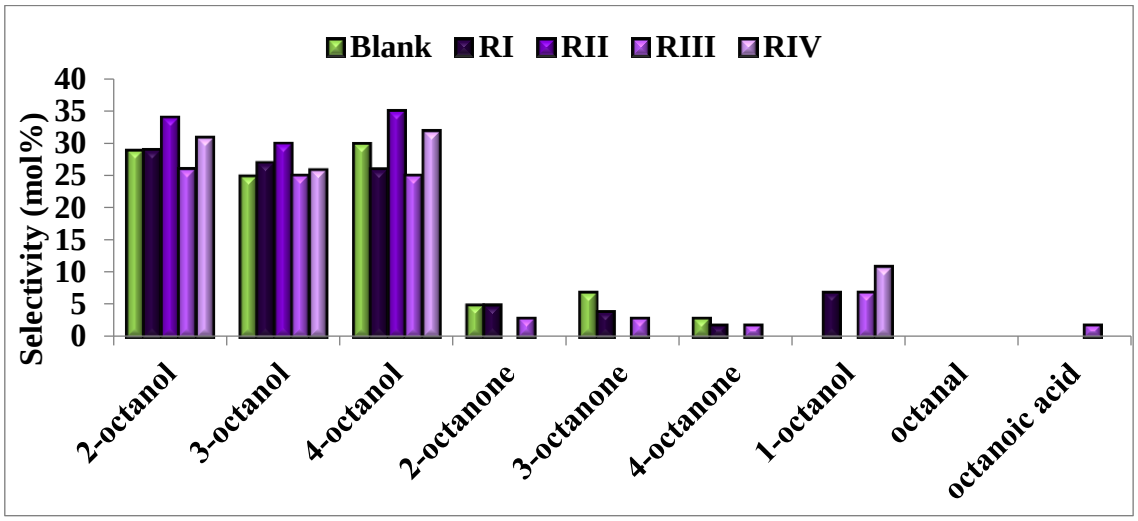

Figure 4.36: The selectivity profiles showing products formed over 24 h at 80 °C with H_2O_2 for **RI-RIV**.

Since predominantly alcohols are produced in the reaction involving *n*-octane and H_2O_2, a plausible mechanism is outlined in Scheme 4.5 where the Ru^{2+}(NNN) catalyst (**1**) reacts with HOO^- to produce the Ru^{2+}OOH species (**2**) which then provides the oxo-ruthenium(IV) species (**3**), through cleavage of the OH bond. The Ru^{3+}OHR• radical (**4**) is formed through abstraction of the hydrogen atom from *n*-octane, *via* the oxo-ruthenium(IV) species. Transfer of the hydroxy ligand to the R• radical affords the alcohol, ROH and the Ru^{2+}(NNN) species, thus completing the cycle. Since alcohols are also formed largely through reaction of the Co

series of catalysts with *n*-octane, this mechanism can also be proposed in the oxidation with H_2O_2 catalysed by Co.

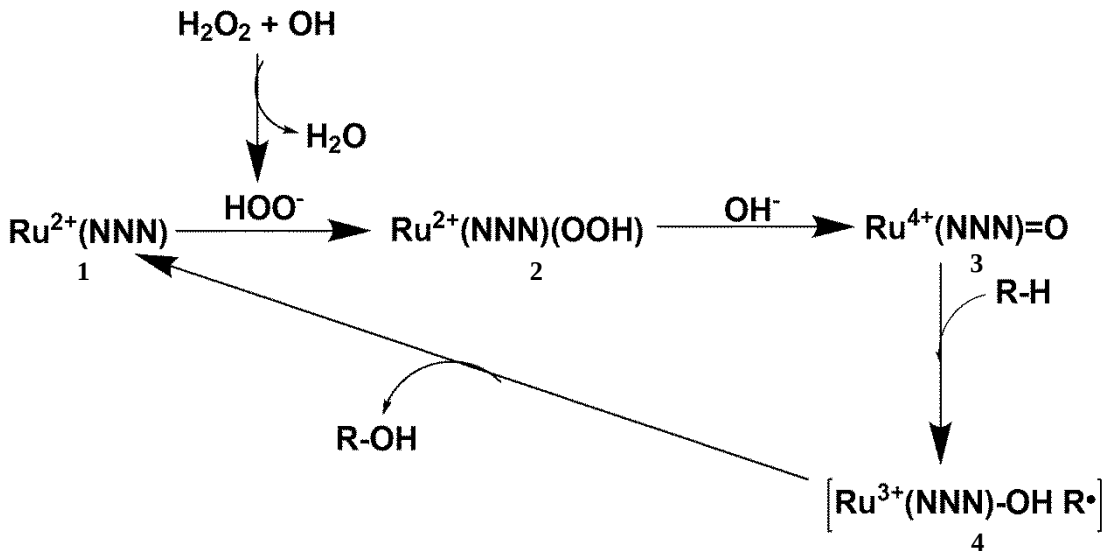

Scheme 4.5: A plausible mechanism in the oxidation of *n*-octane catalysed by **RI**-**RIV** with H_2O_2.

4.3.4 Recovery of catalysts RI and CV

Catalysts **RI** and **CV** were successfully recovered from the reaction solution. IR spectroscopy showed noticeable peak shifts between the fresh catalyst and those of the recovered catalyst **CV** (Fig. 4.37). However, catalyst **RI** shows no significant peak shifts in the IR spectrum (Fig. 4.38). Nonetheless, analysis of the NMR spectrum shows cleavage of the benzene moiety which was originally bound to the Ru metal (Fig. 4.39). This proves that a vacant site was created during the catalysis and subsequent binding of the substrate possibly occurred at this position, accounting for the enhanced reactivities of the Ru catalysts over the Co systems.

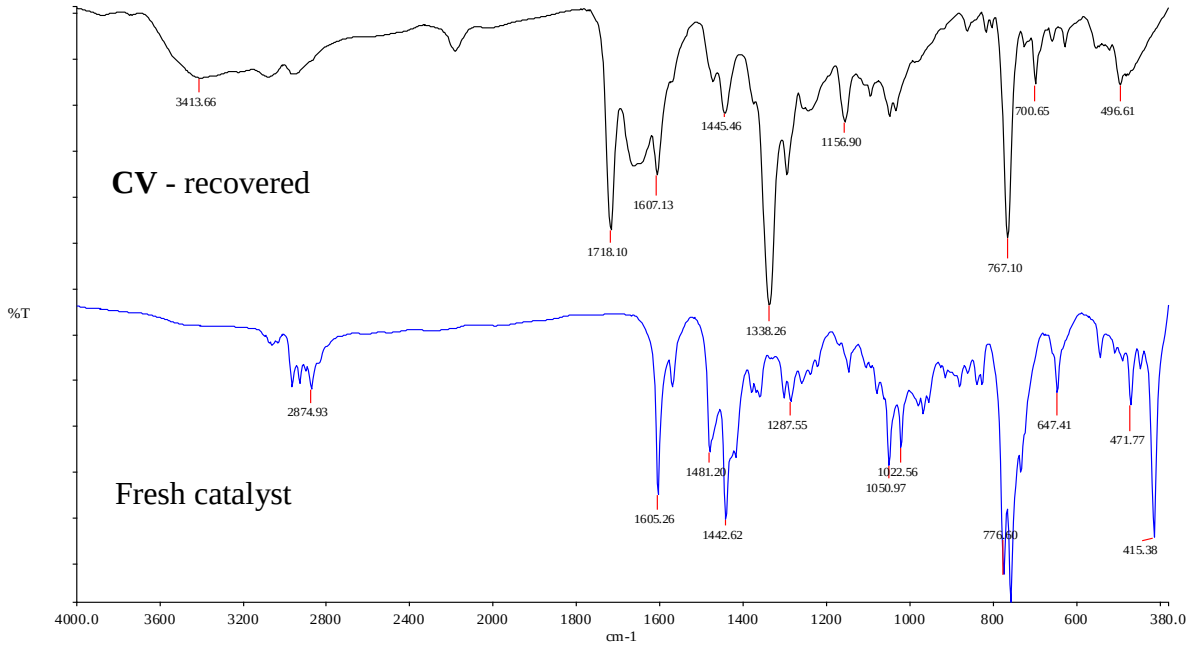

Figure 4.37: IR spectrum of the fresh and recovered catalyst, **CV**.

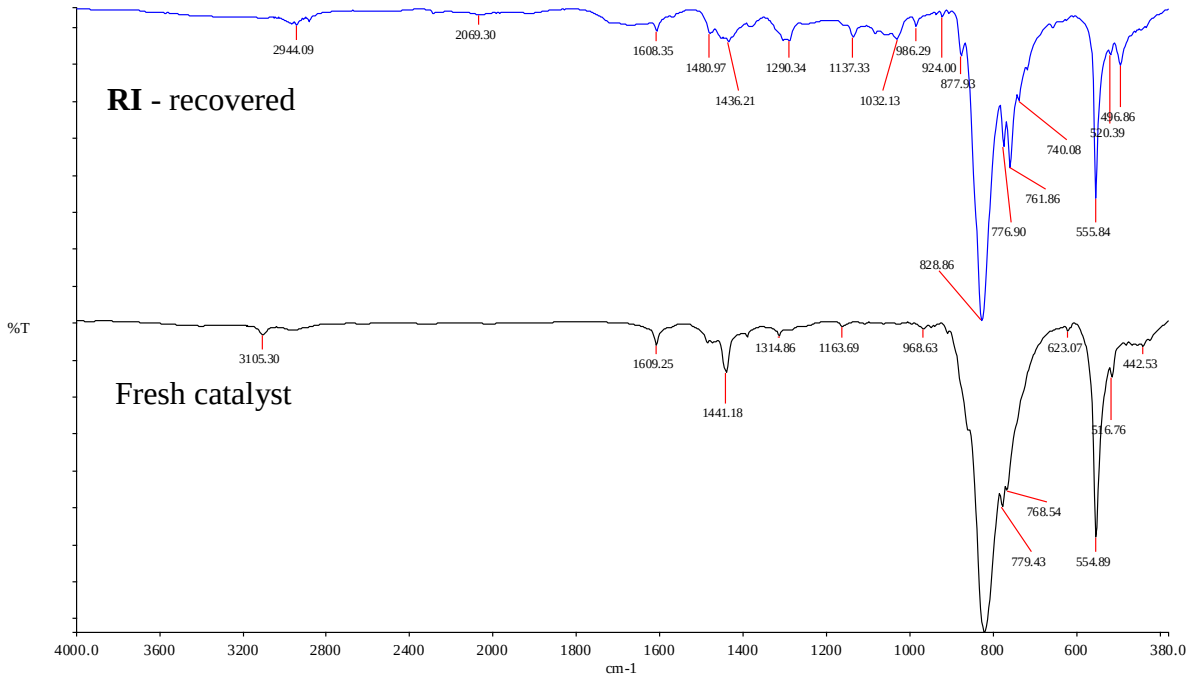

Figure 4.38: IR spectrum of the fresh and recovered catalyst, **RI**.

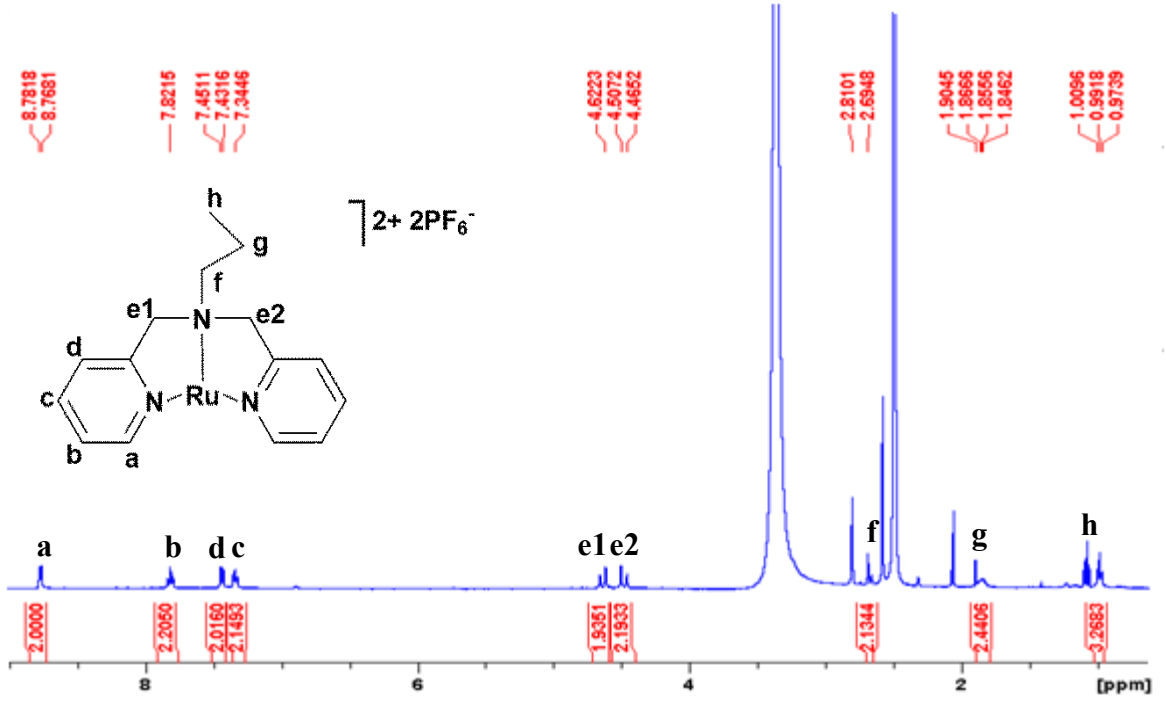

Figure 4.39: NMR spectrum of the recovered catalyst, **RI**.

4.4 Summary

Catalysts **RI**-**CVIII** were studied in the oxidation of *n*-octane using *t*-BuOOH and H_2O_2 as two sources of oxygen. Optimisation using *t*-BuOOH as the oxidant and **CV** as a model system for the Co series, showed that a substrate to oxidant mole ratio of 1:15 at a temperature of 80 °C within 24 hours gave best conversion. Optimisation studies were also carried out using **RI** as a representative system, where similar optimum conditions were found as established with Co, with an exception to the substrate to oxidant mole ratio (1:12).

In the case of *t*-BuOOH as the oxidant, all Co catalysts were dominantly selective to alcohol formation within 24 hours, with selectivities of ca. 65-80% for catalysts **CV**-**CVII**, whilst **CVIII** was most selective to ketones (70%). It was found that predominantly ketones were produced in 24 hours for all Ru catalysts, however, **RI** and **RIV** where more selective to ketones than the other catalysts, which may be attributed to the catalyst's ligand flexibility and bidentate nature of **RIV**, respectively. Catalysts **RI**-**RIII** and **CV** were the only systems that were reactive enough to catalyse the activation of the terminal carbon position. In all catalytic systems, the C(2) position of the hydrocarbon chain was the most reactive, where primarily 2-octanol was formed for the Co systems, while 2-octanone was produced for the Ru catalysts.

Both the Co and Ru catalysts with *tert*-butyl and phenyl backbones respectively (**CVI** and **RIV**) exhibited the highest activity with TONs of 10.2 (10% conversion) and 12.6 (12% conversion). The catalysts that were least efficient where those with a propyl and cyclohexyl substituent on the central N-donor atom of the Co and Ru systems, respectively, with TONs of 7.2 and 8.2. Both systems gave a conversion of 7%. The time-dependent studies of the Co and Ru catalysts show that Co is active over longer periods giving increasing conversions up to 15 hours, compared to Ru, that exhibits high reactivity during the initial hours of the reaction (6 hours). The recovery of catalysts **RI** and **CV** was successful and characterisation techniques (IR and NMR) show that both catalysts were modified during the catalytic testing. However, the state in which both the catalysts exist needs to be further analysed through their respective single crystal data.

It was also concluded that H_2O_2 showed to be a more efficient oxidant than *t*-BuOOH since activities were displayed in the mid-teens up to the 20's for all Co and Ru catalysts with aliphatic substituents on the central N-donor atom. Further investigation will be done using this oxidant in order to examine the effect of the behaviour of the catalysts in converting *n*-octane when varying the substrate to oxidant ratios.

4.5 References

1. M. Sharbatdaran, F. Farzaneh, M. M. Larijani, A. Salimi, M. Ghiasi and M. Ghandi, *Polyhedron*, 2016, **115**, 264-275.
2. L. Soobramoney, M. D. Bala and H. B. Friedrich, *Dalton Transactions*, 2014, **43**, 15968-15978.
3. W. P. Griffith and E. Kwong, *Synthetic Communications*, 2003, **33**, 2945-2951.
4. F. A. Chavez, C. V. Nguyen, M. M. Olmstead and P. K. Mascharak, *Inorganic Chemistry*, 1996, **35**, 6282-6291.
5. J. A. Labinger and J. E. Bercaw, *Nature*, 2002, **417**, 507-514.
6. L. S. Shul'pina, M. V. Kirillova, A. J. L. Pombeiro and G. B. Shul'pin, *Tetrahedron*, 2009, **65**, 2424-2429.
7. T. C. O. Mac Leod, M. V. Kirillova, A. J. L. Pombeiro, M. A. Schiavon and M. D. Assis, *Applied Catalysis A: General*, 2010, **372**, 191-198.
8. V. Mirkhani, M. Moghadam, S. Tangestaninejad, I. Mohammadpoor-Baltork and N. Rasouli, *Catalysis Communications*, 2008, **9**, 2411-2416.
9. F. Chen, Q. Meng, S.-Q. Han and B. Han, *Organic Letters*, 2016, **18**, 3330-3333.
10. L.-T. Li, J. Huang, H.-Y. Li, L.-J. Wen, P. Wang and B. Wang, *Chemical Communications*, 2012, **48**, 5187-5189.
11. A. R. Silva, T. Mourão and J. Rocha, *Catalysis Today*, 2013, **203**, 81-86.
12. M. V. Kirillova, A. M. Kirillov, D. Mandelli, W. A. Carvalho, A. J. L. Pombeiro and G. B. Shul'pin, *Journal of Catalysis*, 2010, **272**, 9-17.
13. S.-I. Murahashi, N. Komiya, Y. Oda, T. Kuwabara and T. Naota, *Journal of Organic Chemistry*, 2000, **65**, 9186-9193.
14. D. Naicker, H. B. Friedrich and B. Omondi, *RSC Advances*, 2015, **5**, 63123-63129.
15. C. A. Tolman, *Chemical Reviews*, 1977, **77**, 313-348.
16. R. R. Fernandes, J. Lasri, M. F. C. G. da Silva, J. A. L. da Silva, J. J. R. Fraústo da Silva and A. J. L. Pombeiro, *Applied Catalysis A: General*, 2011, **402**, 110-120.
17. G. B. Shul'pin, *Journal of Molecular Catalysis A: Chemical*, 2002, **189**, 39-66.
18. T. A. Fernandes, V. André, A. M. Kirillov and M. V. Kirillova, *Journal of Molecular Catalysis A: Chemical*, 2017, **426**, 357-367.
19. A. Sabbatini, L. M. D. R. S. Martins, K. T. Mahmudov, M. N. Kopylovich, M. G. B. Drew, C. Pettinari and A. J. L. Pombeiro, *Catalysis Communications*, 2014, **48**, 69-72.

20. R. A. Sheldon, *Chemical Communications*, 2008, 3352-3365.
21. K. T. Mahmudov, M. N. Kopylovich, M. F. C. G. d. Silva, P. J. Figiel, Y. Y. Karabach and A. J. L. Pombeiro, *Journal of Molecular Catalysis A: Chemical*, 2010, **318**, 44-50.
22. P. J. Figiel, A. Sibaouih, J. U. Ahmad, M. Nieger, M. T. Räisänen, M. Leskelä and T. Repo, *Advanced Synthesis & Catalysis*, 2009, **351**, 2625-2632.
23. L. M. T. Frija, E. C. B. A. Alegria, M. Sutradhar, M. L. S. Cristiano, A. Ismael, M. N. Kopylovich and A. J. L. Pombeiro, *Journal of Molecular Catalysis A: Chemical*, 2016, **425**, 283-290.
24. A. Samuni, S. Goldstein, A. Russo, J. B. Mitchell, M. C. Krishna and P. Neta, *Journal of the American Chemical Society*, 2002, **124**, 8719-8724.
25. F. A. Chavez, J. A. Briones, M. M. Olmstead and P. K. Mascharak, *Inorganic Chemistry*, 1999, **38**, 1603-1608.
26. G. L. Banks, A. J. Chalk, J. E. Dawson and J. F. Smith, *Nature*, 1954, **174**, 274-275.
27. J. F. Black, *Journal of the American Chemical Society*, 1978, **100**, 527-535.
28. F. Zhang, P. Du, J. Chen, H. Wang, Q. Luo and X. Wan, *Organic Letters*, 2014, **16**, 1932-1935.
29. T. K. M. Shing, Yeung and P. L. Su, *Organic Letters*, 2006, **8**, 3149-3151.
30. N. Turrà, U. Neuenschwander, A. Baiker, J. Peeters and I. Hermans, *Chemistry – A European Journal*, 2010, **16**, 13226-13235.
31. E. Spier, U. Neuenschwander and I. Hermans, *Angewandte Chemie International Edition*, 2013, **52**, 1581-1585.
32. A. E. Shilov and G. B. Shul'pin, *Chemical Reviews*, 1997, **97**, 2879-2932.
33. G. B. Shul'pin, A. E. Shilov and G. Süss-Fink, *Tetrahedron Letters*, 2001, **42**, 7253-7256.
34. T. A. Fernandes, C. I. M. Santos, V. André, J. Kłak, M. V. Kirillova and A. M. Kirillov, *Inorganic Chemistry*, 2016, **55**, 125-135.
35. T. A. Fernandes, C. I. M. Santos, V. Andre, S. S. P. Dias, M. V. Kirillova and A. M. Kirillov, *Catalysis Science & Technology*, 2016, **6**, 4584-4593.
36. M. V. Kirillova, M. L. Kuznetsov, V. B. Romakh, L. S. Shul'pina, J. J. R. Fraústo da Silva, A. J. L. Pombeiro and G. B. Shul'pin, *Journal of Catalysis*, 2009, **267**, 140-157.
37. M. L. Kuznetsov and A. J. L. Pombeiro, *Inorganic Chemistry*, 2009, **48**, 307-318.
38. J. F. Hartwig and M. A. Larsen, *ACS Central Science*, 2016, **2**, 281-292.

39. J. M. Gichumbi, H. B. Friedrich and B. Omondi, *Journal of Molecular Catalysis A: Chemical*, 2016, **416**, 29-38.

40. J. M. Gichumbi, H. B. Friedrich and B. Omondi, *Transition Metal Chemistry*, 2016, **41**, 867-877.

41. V. D. B. C. Dasireddy, H. B. Friedrich and S. Singh, *Applied Catalysis A: General*, 2013, **467**, 142-153.

Chapter Five

Conclusion

The preparation of a set of NNN-pyridine based pincer ligands with varying amine backbones comprising of aliphatic and aromatic substituents, was achieved. These ligands were characterised using NMR, IR and MS and were successfully complexed to Ru and Co metal precursors. The formation of these complexes were confirmed through characterisation techniques, including NMR (for Ru compounds), IR, MS, melting point and elemental analyses that proved the purity of all synthesised complexes. Single crystal XRD confirmed the formation of pincer complexes in the cases of **RI**-**RIII** and **CV**, in which the ligand coordinated in a terdentate fashion to the metal centre.

Catalytic testing was carried out with complexes **RI**-**CVIII** using two oxidants, *viz. tert*-butylhydroperoxide and hydrogen peroxide, and *n*-octane as the linear paraffinic substrate. The results show that both oxidants hold promise in the C-H activation of the substrate. Using *t*-BuOOH, the most active catalysts were **RIV** and **CVI** with conversions of 12% and 10% observed for both systems, respectively. The use of H_2O_2 was also investigated under the established optimised conditions (using *t*-BuOOH as the oxidant) and complexes **RI**-**CVIII** were tested in the oxidation of *n*-octane. The results show that all systems (except **RIV** and **CVIII**) were highly active in the oxidation of *n*-octane with H_2O_2 forming more alcohols within 24 hours (compared to *t*-BuOOH) due to the promoting effect of water. Catalysts **RII** and **CVII** showed the highest activity which was attributed to an electronic effect and ligand flexibility, respectively.

In the case of *t*-BuOOH as the oxidant and a substrate to oxidant ratio of 1:15, the selectivity profiles of the Co catalysts show that **CV**-**CVIII** are highly selective to alcohols, while **CVIII** is more selective to ketones. The effect was rationalised through the steric and electronic influences of the ligand (**CVI**), where the overall steric bulk of the catalysts made each complex more selective rather than more reactive. From the regioselective parameters and a substrate to oxidant ratio of 1:12, the Ru complexes were more selective to ketones with 2-octanone predominantly formed. However, 2-octanol was the dominant product observed for the Co systems. Also, selectivity to 1-octanol was only observed for the Ru catalysts. Time-dependent studies reveal that over oxidation is more prominent with Ru than

with Co. Also, the initial rates of the reactions catalysed by **RIV** and **CVIII** (producing the highest concentration of ketones) were higher than **RIII** and **CVII** which produced the highest content of alcohols within 24 hours.

Recovery of catalysts **RI** and **CV** was successful and was proven through IR and NMR characterisation techniques, which showed that both catalysts were altered during the catalytic testing and may still hold promise in conducting recyclability reactions using each system.

It can be generally concluded that the main objective of the study was achieved, where the proposed catalysts were successful synthesised and characterised. Furthermore, the oxidation of *n*-octane using *t*-BuOOH and H_2O_2 was successfully achieved using Ru and Co NNN systems, and showed promising results despite their rigid nature. Finally, Ru showed to be more reactive than Co, where over-oxidation was more prominent and reactions reached completion faster. Reactions catalysed by the Ru and Co complexes using *t*-BuOOH and H_2O_2, were also shown to proceed *via* radical mechanisms.

Supporting information

The supporting information accompanying this dissertation includes full spectroscopic data (^{1}H NMR, ^{13}C NMR, ^{13}C DEPT 135 NMR, ^{13}C APT NMR, HSQC, HMBC and IR), mass spectrometry, raw data for the elemental analysis and single crystal X-ray crystallography, and catalytic data for all complexes. The data presented in appendices A2, A3 and A4 are in the same order as referenced in the individual chapters within the thesis. Readers are encouraged to access the supplementary material for further information which is provided as pdf documents on the compact discs accompanying this dissertation.